

# Detection and Characterization of Defects in Reinforced Concrete Elements Using Frequency Response Functions

By

Sikandar H. Sajid

Department of Civil Engineering and Applied Mechanics



McGill University

Montreal, Quebec, Canada

December 2021

A thesis submitted to McGill University in partial fulfillment of the requirements for the degree  
of Doctor of Philosophy

© Sikandar Sajid, 2021



## ABSTRACT

A major portion of the existing reinforced concrete infrastructure suffers from age and durability related distress. The climate change appears to increase the rate of these deteriorations, which highlights the importance of efficient condition assessment tools for better maintenance and help in prudent decision making regarding the repair or replacement of affected structures and optimal allocation of funds. The impulse-response test is one of the most versatile of nondestructive test methods, which is widely used as a fast scanning method for the condition evaluation of reinforced concrete structural elements. However, due to the limited theoretical understanding of the test and the empirical nature of damage indices used to interpret the results, the accuracy and potential of diagnostics derived from the test have not been rigorously evaluated.

First, a thorough literature review is performed to document the published case studies for the use of the impulse-response test for the condition assessment of various types of civil engineering structures. The review also identifies knowledge gaps relative to the theoretical understanding of the test, and the limitations of current data interpretation tools to improve defect detection with the test.

Second, the theoretical basis of the impulse-response test is established using laboratory experiments and 3D finite element modeling. The formation of stationary waves after impact with a hammer and the relative variation of the local dynamic responses of the test element at different measurement points along its surface are shown to form the basis for defect detection. A modification in experimental setup is identified and proposed, which enables the localization of delamination in a slab using new damage sensitive features derived from an extended frequency range of the frequency response function.

Third, a new signal processing technique based on principal component analysis and outlier detection is introduced which uses the frequency response functions (FRFs) obtained using the impulse-response test as the vector-valued features. These features are shown to be directly related to the presence of defects and their severity. The factor scores associated with the vector-valued features are shown to spatially delineate both the delamination and honeycomb in a reinforced concrete plate specimen as compared to the existing indices, which only can only delineate the delamination.

Fourth, a new damage detection procedure based on the affinity propagation (AP) algorithm and homoscedasticity is proposed. The FRFs obtained with the impulse-response test according to the protocols of ASTM C1740 are combined to generate the feature space matrix. The AP algorithm is used to cluster the FRFs in the feature space. Clusters are shown to correspond to either intact locations or defects and cluster membership can be used to locate defects in the plate. The effectiveness of the algorithm for damage delineation is dependent on the optimal number of exemplars and some objective criteria to categorize each cluster according to the severity of defects. To achieve this objective, an upper bound for the number of exemplars is proposed for optimal defect detection. Further, the variance of the FRF is proposed and validated as a criterion for ranking the severity of defects and for merging exemplars that exhibit similar levels of variability to ensure the optimal number of clusters. The latter is achieved by checking the homoscedasticity of each pair of exemplars using Levene's test for the equality of variance. The proposed procedure is shown to accurately detect debonding and shallow delamination, as well as honeycomb and deep delamination, but to a lesser extent.

## Résumé

Une grande partie de l'infrastructure existante en béton armé souffre de détérioration due à leur âge et leur durabilité. Les changements climatiques semblent exacerber le taux de ces détériorations, ce qui souligne l'importance de développer des outils efficaces pour l'évaluation de l'état des infrastructures afin de planifier une maintenance efficace et des décisions appropriées pour la réparation ou le remplacement des structures affectées et l'allocation optimale des fonds. Le test par réponse impulsionnelle est l'une des méthodes d'essai non destructives les plus polyvalentes et répandue. Cette méthode, par sa facilité et rapidité d'exécution, permet son utilisation sur des grandes surfaces d'éléments structuraux. Cependant, en raison de la compréhension théorique limitée de l'essai et de la nature empirique des indices de dommages utilisés pour interpréter les résultats, l'exactitude et le potentiel des diagnostics dérivés de l'essai n'ont pas été rigoureusement évalués. Premièrement, une revue approfondie de la littérature est effectuée pour documenter les études de cas du test pour l'évaluation de l'état de divers types de structures de génie civil. Cet examen identifie également les lacunes dans les connaissances relatives à la compréhension théorique du test, et les limites des outils d'interprétation des données, afin d'améliorer la détection et l'interprétation des défauts. Deuxièmement, les bases théoriques du test sont établies à l'aide d'expériences en laboratoire et la modélisation 3D par éléments finis. Il est démontré que la formation d'ondes stationnaires suite à un impact à l'aide d'un marteau, et la variation relative des réponses dynamiques de l'élément à différents points de mesure le long de sa surface constituent le fondement pour la détection des défauts. Une modification mineure dans la configuration expérimentale de l'essai est identifiée et proposée afin d'étendre la gamme utile des fréquences du test et proposer de nouveaux indices d'endommagement. Troisièmement, une nouvelle technique de traitement de signal basée sur l'analyse en composantes principales et la détection des valeurs aberrantes est introduite, qui utilise le FRF dérivé du test de réponse impulsionnelle comme caractéristiques vectorielles. Les analyses démontrent que ces caractéristiques sont fortement corrélées à la présence des défauts et à leur sévérité. Les scores des composantes principales sont utilisés pour délimiter spatialement le délaminage et le nid d'abeille dans une plaque expérimentale en béton armé. Quatrièmement, un nouvel algorithme de détection de dommages est proposé qui utilise l'algorithme de propagation d'affinité (AP) et l'homoscédasticité. Les FRF obtenues avec le test de réponse impulsionnelle selon les protocoles de la norme ASTM C1740 sont combinées pour générer la matrice d'espace objet. L'algorithme

AP est utilisé pour regrouper les FRF dans l'espace des fonctionnalités. Les regroupements correspondent à des emplacements intacts ou à des défauts et l'appartenance à un regroupement peut être utilisée pour localiser des défauts dans la plaque. L'efficacité de l'algorithme de délimitation des dommages dépend du nombre optimal d'exemplaires et de certains critères objectifs pour catégoriser chaque regroupement en fonction de la gravité des défauts. Pour atteindre cet objectif, une borne supérieure du nombre d'exemplaires est proposée pour une détection optimale des défauts. En outre, la variance de la FRF est proposée et validée comme critère de classement de la gravité des défauts et de fusion des exemplaires présentant des niveaux de variabilité similaires afin d'assurer un nombre optimal de regroupements. Cette dernière est obtenue en vérifiant l'homoscédasticité de chaque paire d'exemplaires à l'aide du test de Levene pour l'égalité de la variance. Il est démontré que la procédure proposée détecte avec précision le décollement et le délaminage peu profond, ainsi que le nid d'abeilles et le délaminage profond, mais dans une moindre mesure.

## ACKNOWLEDGEMENTS

I would like to express sincere appreciation to my supervisor, Prof. Luc E. Chouinard for his confidence in me, invaluable patience, constant support, and providing a conducive environment to flourish research ideas and explore them in a self-dependent way. I also would like to express gratitude to him for his insightful ideas, knowledge, and guidance at crucial stages of my research. He is one of the best supervisors a doctoral student can ask for.

I would also like to acknowledge the useful feedback from my doctoral thesis committee. The feedback and valuable comments on different aspects of this research by Prof. Marco Amabili, Mechanical Engineering Department, McGill University, and Dr. Nicholas Carino, Honorary member of the American Concrete Institute, and Concrete Technology Consultant, United States, are highly appreciated. I highly appreciate the mentorship and guidance of Prof. Dr. Qaisar Ali, Pro-Vice Chancellor, University of Engineering and Technology (UET), Peshawar, Pakistan, and Prof. Dr. Akhtar Naeem Khan, Dean Faculty of Engineering, UET Peshawar, Pakistan.

I would like to acknowledge the named fellowships under the McGill Engineering Doctoral Award, the Natural Sciences and Engineering Research Council (NSERC), the Mobility Award by Graduate and Postdoctoral Studies, and the GREAT award by Civil Engineering.

I am especially thankful to my brothers at heart Hizb Ullah Sajid and Saif Ullah Sajid for their support, and unending kindness which were phenomenal in the successful completion of this research.

Finally, and most importantly, I would like to express my profound gratitude to my beloved parents for their encouragement, love, and support. I could not have made it this far without them.

## PUBLICATIONS, MANUSCRIPTS

- [1] **Sajid, S.**, & Chouinard, L. (2019). Impulse response test for condition assessment of concrete: A review. *Construction and Building Materials*, 211, 317-328.
- [2] **Sajid, S.**, Taras, A., & Chouinard, L. (2021). Defect Detection in concrete plates with Impulse-Response Test and Statistical Pattern Recognition. *Mechanical Systems and Signal Processing*, volume 161(2021).
- [3] **Sajid, S.**, Chouinard, L., Taras, A., (Accepted). Developing a new understanding of the impulse-response test for defect detection in concrete plates. *Journal of Engineering Mechanics* 148:04021125.
- [4] **Sajid, S.**, Chouinard, L., Carino, N., (in submission) Damage detection in concrete plate using mobility and clustering. *Structural Health Monitoring*.

# Table of Contents

1. Introduction .....	1
1.1 Background and Problem Statement .....	1
1.2 Research Objectives .....	2
1.3 Thesis Organization.....	3
2. Impulse Response Test for Condition Assessment of Concrete: A Review.....	5
Abstract .....	5
2.1 Introduction .....	5
2.2 Defects in Concrete .....	7
2.2.1 Delamination.....	7
2.2.2 Cracks .....	7
2.2.3 Debonding.....	7
2.2.4 Voids and Honeycombing.....	7
2.2.5 Loss of Ground Support.....	8
2.3 Impulse Response Test Method .....	8
2.3.1 Description of Method .....	8
2.3.2 Current State-of-the-Art of Case Studies .....	11
2.3.3 Current State-of-the-art of Data Analysis .....	14
2.3.4 Grid Size .....	15
2.4 Impulse Response Test with other NDT Methods .....	17
2.5 Impulse Response Test for Deep Foundations .....	20
2.6 Theory behind the Impulse-Response Test for Concrete Structures.....	26
2.7 Reliability of Impulse-Response Test .....	28
2.9 Conclusion.....	32

3. Developing a New Understanding of the Impulse Response Test for Defect Detection in Concrete Plates.....	42
Abstract .....	42
3.1 Introduction .....	43
3.2 Impulse-response Test.....	44
3.3 Motivation and Objectives of Research .....	45
3.4 Experimental Investigation .....	49
3.5 Data Analysis .....	52
3.6 Finite Element Modeling.....	56
3.6.1 Dynamic behavior of the Plate in Vicinity of Delaminations.....	56
3.6.2 Influence of Experimental Setups.....	59
3.6.3 Working Principle of the Test.....	60
3.7 Defect Localization Limiting Extent of Detectability.....	61
3.8 Discussion and Conclusions.....	68
4. Defect Detection with Impulse-Response Test and Statistical Pattern Recognition.....	75
Abstract .....	75
4.1 Introduction .....	76
4.2 Literature Review.....	78
4.3 Relation between Material Defects and the FRF .....	79
4.4 Pattern Recognition Algorithm .....	81
4.5 Experiments.....	85
4.5.1 Fully Supported Clamped Plate with Multiple Voids.....	85
4.5.2 Reinforced Concrete Plate on Elastic Foundation .....	91
4.6 Discussion and Future Research Prospects .....	100
4.7 Conclusion.....	101

5. Detection and Ranking of Damage in Concrete Plates Using Impulse-response Test with Affinity Propagation and Homoscedasticity .....	108
Abstract .....	108
5.1 Introduction .....	108
5.2 Condition Assessment Methods .....	109
5.3 Impulse-response Test.....	110
5.4 Literature Review.....	112
5.5 Frequency Response Function and Defects .....	113
5.6 Proposed Procedure.....	116
5.6.1 Vectorization of the FRFs.....	116
5.6.2 Affinity Propagation (AP).....	116
5.6.3 Homoscedasticity or Equality of Variance Test .....	118
5.7 Experimental Study .....	119
5.7.1 Fully Supported Slabs with Free Edges .....	119
5.7.2 Concrete slab on Elastic Foundation with Restrained Edges.....	127
5.7.3 Ultrasonic Shear Wave Tomography Test for Slab 3 .....	132
5.8 Concluding Remarks .....	132
6. Chapter 6. Original Research Contributions and Recommendations .....	139
6.1 Original Research Contributions.....	139
6.2 Recommendations for Future Research .....	140

## LIST OF FIGURES

Figure 2-1. Typical mobility plot.....	10
Figure 2-2. Mobility plot in time domain (Daniel Clem & Shumacher, 2012).....	15
Figure 2-3. Impulse-response test impact configuration used by Lo et al. (Lo et al., 2010) for piles shafts with caps. ....	23
Figure 2-4. Typical mobility plot obtained from the impulse-response test for a pile (S.-H. Ni et al., 2011). .....	24
Figure 3-1. Mobility spectrum and definition of mobility indices (ASTM C1740-16). ....	45
Figure 3-2. Concrete formwork and artificial delamination in the plate. (Photo courtesy: Institut de recherche d'Hydro-Québec, Canada). ....	50
Figure 3-3. Plan view of test plate and artificial delamination (dimensions are in the units of mm). ....	51
Figure 3-4. Performing impulse-response test with rubber tipped hammer (left) and steel tipped hammer (right). ....	51
Figure 3-5. Acceleration frequency response function for test at defect 'B' in comparison with intact location.....	53
Figure 3-6. Comparison of (a) average accelerance and (b) accelerance slope, for the intact and defect locations. ....	54
Figure 3-7. Accelerance as a function of frequency for intact location comparison with (a) Defect A, B, and F (b) Defect C, E, and G.....	55
Figure 3-8. (a) Finite element mesh of the test plate, and (b) FE simulated delaminations in ABAQUS®. .....	57
Figure 3-9. Eigen value analysis results showing different mode shapes of the concrete plate associated with a) Defect A b) Defect B and c) Defect C d) Defect E e) Defect F, and f) Defect G.....	59
Figure 3-10. FRF for defect G from experiments and numerical simulations for different sensor-impactor distances. (b) Accelerance as a function of sensor-impactor distance. ....	60
Figure 3-11. Wave propagation analysis after impact. (a) Wave components 90 microsecond after impact. (b) Standing waves at 650 microseconds after the impact. ....	61
Figure 3-12. Peak frequency as a function of the size and depth of defects for the experimental data (left), and numerical simulations (right). ....	63
Figure 3-13. Accelerance as a function of the size and depth of defects for the experimental data (left) and the numerical simulations (right). ....	64

Figure 3-14. Average Accelerance as a function of the size and depth of defects for the experimental data (left) and the numerical simulations (right) .....	64
Figure 3-15. Accelerance slope as a function of the size and depth of defects for experimental data (left) and the numerical simulations (right). .....	65
Figure 3-16. Error ellipsoids for prediction with 95% and 50% confidence levels obtained using correlation analysis for each delamination using (a) frequency, and (b) frequency and average Accelerance. The letters on each subplot represents the respective delamination and the vertical and horizontal axes represents the depth and planar size respectively in mm. ....	68
Figure 4-1. Schematic of defect detection with the impulse-response test using the proposed algorithm. ....	85
Figure 4-2. (a) Plan view of the first test plate with the impulse-response test measurements identified. All the dimensions are in the units of mm. (b) The specimen under construction. (c) The specimen during impulse-response test .....	86
Figure 4-3. Comparison of accelerance spectra with intact and defect locations, and the intact locations near each defect identified in Figure 4.2a with each other. ....	88
Figure 4-4. Pattern of the first 5 principal components for the FRF dataset of clamped concrete plate.....	88
Figure 4-5. Scree plot and the percent variance explained by each component for the FRF dataset of clamped concrete plate.....	89
Figure 4-6. Box and Whisker plots of factor scores for the first 5 eigenvectors for the clamped concrete plate dataset.....	90
Figure 4-7. Outlier detection with ESD test on Factor scores for $\beta = 1$ .....	91
Figure 4-8. The test plate on elastic foundation with measurement grid and locations of void and honeycomb defects.....	92
Figure 4-9. Patterns of the first 4 principal components of the dataset for the plate on elastic foundation.....	93
Figure 4-10. Scree plot and the percentage of variance explained by each component for the data set of the plate on elastic foundation. ....	94
Figure 4-11. Box and whisker plots on factor scores for $\beta = 1-4$ .....	95
Figure 4-12. Outlier detection with ESD test on the factor scores for the first component for the plate on elastic foundation. ....	96
Figure 4-13. Contour plot of the factor score for the first component for the plate on elastic foundation with measurement locations and the outliers respectively by red asterisks and red ellipsoids. ....	97
Figure 4-14. Contour plot of average mobility values for the plate on elastic foundation, with planned defects marked and measurement locations presented with red asterisks.....	98

Figure 4-15. ESD test for outlier detection in the average mobility values at each test point for the plate on elastic foundation. ....	99
Figure 4-16. Tomogram (C-scan) of the plate obtained using ultrasonic shear wave tomography with MiRA®. The measurements of the impulse-response test are shown as yellow circles and the outliers detected with the box and whisker plots and the ESD are shown as red rectangles. ....	100
Figure 5-1. A typical mobility spectrum for concrete plate element with a description of the defect indices according to ASTM C1740-16.....	111
Figure 5-2. Influence of the defect severity on the variance of the FRF in the frequency range of 0-2000 Hz. All dimensions are in units of mm. ....	116
Figure 5-3. Slab specimen during construction (a) slab with defects (Slab 1), (b) reference slab (Slab 2). ....	120
Figure 5-4. Flow chart for detection with AP algorithm and homoscedasticity. ....	122
Figure 5-5. Affinity propagation to obtain the exemplars and the associated identification of measurement locations of Slab 1.....	122
Figure 5-6. The distribution of the input similarities, which includes all the entries of the similarities matrix for (a) Slab 1, and (b) Slab 2. ....	123
Figure 5-7. Exemplars and the associated FRFs in the respective clusters for Slab 1 .....	124
Figure 5-8. Contour plot of ranks of each test point. ....	125
Figure 5-9. AP algorithm for to obtain exemplars and their associated FRFs for Slab 2. Clustering with the AP for fully supported reference slab with free edges .....	126
Figure 5-10. Exemplar and the corresponding FRFs for Slab 2. ....	127
Figure 5-11. Defect delineation with the proposed algorithm for the impulse-response test data for Slab 3. ....	129
Figure 5-12. Histogram of the input similarities for Slab 3. ....	129
Figure 5-13. Exemplars and cluster members resulting from the AP and Levene’s test for Slab 3.....	131
Figure 5-14. Contour plot of variances of FRFs associated with exemplar for Slab 3. ....	131
Figure 5-15. C-scan of the plate obtained with MiRA® after performing ultrasonic shear wave tomography (at a depth of around 130 mm from the top surface). ....	132

## LIST OF TABLES

Table 2-1. Advantages and limitations of the impulse-response test.....	10
Table 2-2. List of case studies involving structures other than drilled shaft piles. ....	11
Table 2-3. Grid size used in various case studies reported by different authors.....	16
Table 2-4. Summary of the published data on the IR test for inter-layer pull-off strength estimation using pattern recognition based inductive mathematical models. ....	19
Table 2-5. Impulse-response test success rate of pile integrity assessment reported by (Briaud et al., 2002). ....	28
Table 2-6. Impulse-response test results for drilled shaft piles with various planned defects based on (Barker et al., 1991). ....	29
Table 3-1. Summary of case studies using the impulse-response test (Sajid and Chouinard 2019).....	47
Table 3-2. Dimensions and depths of planar defects for the test plate.....	49
Table 3-3. Instrumentation used in testing.....	51
Table 3-4. Size and depth of the defects and corresponding amplitudes and frequencies of dominant modes in the experimental FRFs.....	55
Table 3-5. Resonant frequencies and mode shapes associated with defects. ....	58
Table 3-6. Geometrical characteristics of the delaminations for the parametric study and corresponding FRF indices. ....	62
Table 3-7. Results of statistical analysis of the experimental measurements for number of observations of n=6 for each case. ....	65
Table 3-8. Results of statistical analysis for numerical simulations based parametric study. The number of observations is 7 for each case.....	66
Table 4-1. Dimensions and depths of planar defects in the test plate. ....	86
Table 5-1. Specifications of the instruments used for the impulse-response test measurements.....	120
Table 5-2. P-values of Levene's test for each pair of exemplars for Slab 1.....	123
Table 5-3. Levene's test for exemplars obtained using AP for the reference slab with free-free edges...	127
Table 5-4. P-values of Levene's test for each pair of the exemplars for Slab 3 obtained in Figure 5-11..	130
Table 5-5. Ascending order of exemplars based on individual variances for Slab 3.....	130

# 1. Introduction

## 1.1 Background and Problem Statement

The attainment of end of service life and changing climate patterns have rendered a major portion of the existing reinforced concrete infrastructure in advanced stages of deterioration. This necessitates the need for accurate condition assessment for optimal maintenance strategies or informed decisions on replacement. Consequently, several non-destructive test (NDT) methods are used to obtain information on internal condition. Several of these methods for the condition assessment of concrete in structural elements are documented in the consensus committee report of ACI 228.2 (ACI Committee 228, 2013). Many advanced NDT methods for the condition assessment of concrete have been developed over the last few decades, such as, acoustic emission (AE), ground penetrating radar (GPR), ultrasonic shear wave tomography, infrared thermography, and impact-echo (Malhotra & Carino, 2003). The AE needs constant monitoring and hence may have limited practicality and lower potential for field deployment. The ground penetrating radar and impact-echo work respectively on the basis of the reflection of electromagnetic waves due to variations in material media (Maierhofer, 2003) and p-wave due to changes in material impedance (Carino, 2013). This limits the defect detectability of both these methods in densely reinforced concrete sections. The ultrasonic shear-wave tomography generates a 3D image of the internal condition of the test element (Martin, Broughton, Giannopolous, Hardy, & Forde, 2001), yet the longer times needed to complete the measurements limits its applications to evaluation of small portions of the test element. The infrared thermography is a non-contact fast detection method but there are challenges regarding the accuracy of the test results owing to lack of robustness to weather and surface conditions (Büyüköztürk, 1998).

The impulse-response test on the other hand is a widely used fast scanning low frequency method with several successful condition assessment applications (Sajid & Chouinard, 2019). This method overcomes the limitations of the afore mentioned tests; however, it has limited understanding of the technical basis, unknown extent of detectability with the test, robustness of the test results to variation in the experimental setups, and empirically based damage indices for defect detection.

Therefore, an improved understanding on all of the above aspects can lead to better accuracy in diagnostics and potential expansion in the capabilities of the impulse-response test.

## 1.2 Research Objectives

The aim of this research is to characterize the impulse-response test measurements and to furnish better defect delineation and potential localization owing to improved physical understanding through proposed statistical and unsupervised machine learning algorithms. The following objectives and the respective approaches are used:

- a) Perform a critical review of the current state-of-the-art to identify the knowledge gaps.

Compile all the published studies on the subject to ascertain the widespread applications of the method and potential limitations in different aspects of the test.

- b) Developing a technical basis of the impulse-response test for defect detection in concrete plates.

Using experimental specimen with artificial delamination and 3D finite element model, the basic working principle of the test is established. Further, statistical tools are used to determine the limiting depth of delamination for detectability with the impulse-response test. In-addition the reliability of depth estimates of delamination is quantified using Gaussian process with the theoretical damage indices obtained from the extended frequency range of the test.

- c) Improving defect detection with the impulse-response test using statistical features of frequency response functions.

The vectorized frequency response functions derived with the impulse-response test is used in the paradigm of statistical pattern recognition for improved defect delineation and identifying defects of significance.

- d) Improving defect detection using vectorized frequency response functions for defect detection and ranking.

The vectorized frequency response functions together with affinity propagation algorithm and homoscedasticity provided are used to delineate defects. A physics-based approach is used to rank defects on a non-binary basis.

### **1.3 Thesis Organization**

This thesis follows a manuscript-based structure. Each of the main chapters consists of an article published or submitted in a peer-reviewed journal. Therefore, repetitions could not completely be avoided, especially in the introduction sections. All papers are the candidate's original work including the development of software to perform the analyses.

Chapter 1 provides the background on the issues that are being addressed, the motivation for the research, the research objectives, the main lines of the proposed methodology and the structure of the thesis.

Chapter 2 (Article No. 1) presents a detailed literature review compiling the published case studies and other condition assessment applications, the current state-of-the-art of the theoretical understanding and data analysis procedures for the impulse-response test.

Chapter 3 (Article No. 2) establishes a theoretical understanding of the test using 3D finite element model and experimental results. It also presents the sensitivity of the measurements to the changes in the experimental setups, the limiting depth for the detectability of defects with the test, the benefit of using extended frequency range with practical modifications in the experimental setup and the new damage indices in the extended frequency range. Also, the new damage indices are shown to be potentially useful for the localization of defects.

Chapter 4 (Article No. 3) presents a new signal processing algorithm using the paradigm of statistical pattern recognition and outlier detection for the impulse-response test which can potentially delineate defects with the same accuracy as that of the highly refined yet time consuming ultrasonic shear-wave tomography.

Chapter 5 (Article No. 4) proposes a defect detection and ranking procedure based on the affinity propagation algorithm to cluster the frequency response functions obtained from the impulse-response test. Location with defects are clustered separately and hence they are delineated. An upper bound of the number of clusters, and homoscedasticity are used for increasing the accuracy of detection and variance is used for ranking defects on a non-binary basis.

Chapter 6 summarizes the main conclusions for the current work and the directions for future research.

## References

- ACI Committee 228. (2013). In-place methods to estimate concrete strength. *ACI 228.2R*, Farmington Hills, MI.
- Büyüköztürk, O. (1998). Imaging of concrete structures. *NDT & E International*, 31(4), 233-243.
- Carino, N. J. (2013). Training: Often the missing link in using NDT methods. *Construction and Building Materials*, 38, 1316-1329.
- Maierhofer, C. (2003). Nondestructive evaluation of concrete infrastructure with ground penetrating radar. *Journal of Materials in Civil Engineering*, 15(3), 287-297.
- Malhotra, V. M., & Carino, N. J. (2003). *Handbook on nondestructive testing of concrete*: CRC press.
- Martin, J., Broughton, K., Giannopolous, A., Hardy, M., & Forde, M. (2001). Ultrasonic tomography of grouted duct post-tensioned reinforced concrete bridge beams. *NDT & E International*, 34(2), 107-113.
- Sajid, S., & Chouinard, L. (2019). Impulse response test for condition assessment of concrete: A review. *Construction and Building Materials*, 211, 317-328.

## **2. Impulse Response Test for Condition Assessment of Concrete: A Review**

### **Abstract**

The impulse-response test is one of the most versatile non-destructive test (NDT) methods for condition assessment of concrete structures. It is an elastic stress-wave propagation based low-strain and low frequency NDT method, which is widely employed in the NDT industry. Nevertheless, it is used mainly as a relative basis test, in which contour plots of the response parameter are used to distinguish between intact and anomalous regions in the test element. This article is the first to compile current published literature on the subject. A summary of the published case studies using impulse-response test is presented, followed by the current state-of-the-art of the fundamental theoretical understanding of the method. Current knowledge gaps are identified and recommendations are proposed to address these issues. The recommendations are aimed to move the impulse-response test from a qualitative NDT method to a quantitative condition assessment tool for concrete structures.

### **Keywords**

Concrete, non-destructive test, impulse-response test, low-strain integrity test, condition assessment.

### **2.1 Introduction**

Non-destructive testing (NDT) is employed as a non-invasive indirect testing technique for the condition assessment of structures and its component. NDT methods are based on the interaction of controlled physical “disturbances” with the internal structure of the test object. Condition assessment of a structure is of prime importance before any repair or maintenance operations is carried out. This assessment is necessary for efficient repair strategies and appropriate allocation of funds for the project (Yehia, Abudayyeh, Nabulsi, & Abdelqader, 2007). There have been projects in which the required repair was much more extensive than expected and the repair costs exceeded the replacement cost of the whole structure because the internal damage was not discovered until the commencement of repair (Jesper Stærke Clausen & Knudsen, 2009). Reliable information of the existing condition of a structure, is possible only through an NDT survey using

well-established methods. Furthermore, many NDT methods are employed for quality control during or soon after the construction operations (Han, 2004; S Nazarian, Yuan, & Tandon, 1999).

There are several NDT methods available for the above cited purpose as documented in the American Concrete Institute report ACI 228.2R (ACI-228.2R-13). Elastic stress-wave propagation based NDT methods are employed widely for the condition assessment of concrete structures. The two most versatile of this genre of methods are the impact-echo (IE) and impulse-response methods. The IE method was developed by Sansalone and Carino in 1980s at the National Institute of Standards (M Sansalone & Carino, 1986) and a detailed description is provided by Sansalone (Mary Sansalone, 1997). Besides several inherent limitations of the IE test, the speed of testing is considerably slow (Delatte et al., 2003). The impulse-response test, on the other hand, is a fast screening method. However, this method differentiates anomalous regions of the test element from the integral portion primarily on relative basis. Furthermore, the type of anomaly in the identified region and the location along the thickness of the test element cannot be ascertained using this test. These two challenges have rendered the impulse-response test primarily a qualitative NDT method for which the identified anomalous regions are checked in detail by more refined methods like IE.

There is sparse published literature on the various aspects of the impulse-response test (Oh, 2012). This article provides a comprehensive review of available literature on the subject. Furthermore, a critical analysis is presented that identifies the current knowledge gaps and technical challenges. Subsequently, future research perspectives are delineated to fill in these gaps.

Section 1 of this article describes common defects that may occur in concrete structures. Section 2 describes the impulse-response test with a brief history of the development and a review of published case studies of applications for concrete structures. Section 3 reviews the impulse-response test applied in combination with other testing methods for the assessment of materials properties. Section 4 gives an overview of the current state-of-the-art for impulse-response test for integrity assessment of drilled shaft foundations. Section 5 reviews the reliability of the impulse-response test obtained from the published case studies. Section 6 presents theoretical studies of impulse-response test for concrete structures. Section 7 presents a critical review and discussion on the state-of-the-art by identifying the current challenges in using the impulse-response test and research perspectives for addressing these challenges.

## **2.2 Defects in Concrete**

Concrete is a composite material that can be produced from numerous mix proportions using its constituent ingredients with the varied end product properties. Concrete can undergo deterioration because of durability issues in the short term and long term. Failure of addressing these can seriously affect the intended use of the concrete element and, in many cases, the overall integrity of the structural system. The most common defects in concrete elements are discussed in this section.

### *2.2.1 Delamination*

Delamination defects are most common in bridge decks and other plate like reinforced concrete structures. Published reports reveal that corrosion affected reinforced concrete structures are generally prone to delamination and cracking (C.-Q. Li, Zheng, Lawanwisut, & Melchers, 2007). This type of defect is subsurface crack parallel to a surface and in most cases is not noticeable given its location. Unchecked progression of delamination may ultimately result in loss of structural serviceability and cause premature failure of reinforced concrete elements (C. Li, 2003).

### *2.2.2 Cracks*

Cracks in concrete elements may result due to loading, volume change and several durability issues like freeze-thaw induced cracking and chemical attack. The cracks provide a direct path for the invasive materials to get inside the concrete and further the deterioration. The extent and size of the crack is hence an important parameter in condition assessment practices.

### *2.2.3 Debonding*

The provision of bonded concrete overlay on pavements and bridge decks is a major rehabilitation technique for these structural elements. The bond between the overlay and the existing slab is to ensure monolithic behavior. The loss of bond strength, termed as debonding of overlay, due to various reasons is a major durability issue in the rehabilitated concrete element.

### *2.2.4 Voids and Honeycombing*

Both voids and honeycombing are primarily due to poor quality control during construction. Honeycombing is a disproportionately high localized void ratio mainly due to inadequate consolidation of concrete.

### *2.2.5 Loss of Ground Support*

This is not a concrete defect per se, rather it is more of geotechnical induced failure. Due to geotechnical issues, concrete pavements and tunnel linings may lose the adjacent ground support, which affects the integrity of the concrete structure. The primary structural distress in continuously reinforced concrete pavements is the edge punchout. It is caused primarily by loss of support beneath the pavement (Gharaibeh, Darter, & Heckel, 1999). The loss of soil support around tunnel linings can result in circumferential cracking due to differential settlement or longitudinal cracking due to ovalization (Leung & Meguid, 2011). Early detection and remedial measures may avoid cracking of the tunnel lining.

## **2.3 Impulse Response Test Method**

### *2.3.1 Description of Method*

The impulse-response method is a low-strain, elastic stress-wave propagation-based NDT technique. In 1968, the term “La Méthode d’Admittance Mécanique” first appeared in the literature, which translates as “Mechanical Admittance Method” (Paquet, 1968). Paquet (1968) used the electrical transmission line theory and applied it to the one-dimensional problem of compressional bar stress wave transmitted from the pile head down the shaft. Throughout the course of developments in 1970s and 1980s it had have several names like, Vibration Test, Sonic-Mobility Method, Transient Dynamic Response (TDR), Impulse Response Spectrum (IRS) and Impulse Response Method (IR) etc. Finally, it became known as the impulse response (IR) method in early 1990s (Hertlein & Davis, 2007).

The impulse-response test for concrete structures, other than pile shafts, was developed by Allan G. Davis and Bernard H. Hertlein in the twentieth century (AG Davis & Hertlein, 1987; Allen Davis, Hertlein, Lim, & Michols, 1996; Allan G. Davis & Hertlein, 1990; Allen G Davis & Hertlein, 1995). This test method was traditionally used for integrity assessment of pile foundations. However, in 1985, with the advent of relatively portable personal computers with analog to digital (A/D) data acquisition cards, high sampling rates, onboard pre-trigger facilities, and vastly increased data storage facilities, tremendous advances were made and it enabled the impulse-response method to be used for other applications besides pile testing (Allen G Davis, 2003). The test involves striking the test object with an instrumented hammer and measuring

velocity response at adjacent point. The force time history (from the instrumented hammer) and the velocity time history (from the transducer) is used in a transfer function to obtain the mobility spectrum. The condition assessment of a structure using IR test is performed by interpreting the mobility plot, which is the basic output of this test. The steps to develop this plot as given by Sadri and Mirkhani (Sadri & Mirkhani, 2009) and Higgs (Higgs, 1979) are:

- a. Calculate the Fourier transforms of the measured force-time function,  $f(t)$  and the measured response,  $v(t)$ . These will be denoted as  $F(\omega)$  and  $V(\omega)$ .
- b. Using the complex conjugate of the Fourier transform of the force-time function  $F^*(\omega)$ , compute the cross power spectrum,  $V(\omega) \cdot F^*(\omega)$ .
- c. Compute the power spectrum of the force-time function,  $F(\omega) \cdot F^*(\omega)$ .
- d. Divide the cross-power spectrum by the power spectrum to obtain the transfer function according to Eq. 2-1.

$$H(\omega) = \frac{V(\omega) \cdot F^*(\omega)}{F(\omega) \cdot F^*(\omega)} \quad (2-1)$$

A typical mobility plot for a plate like element is provided in Figure 2-1. The parameters that can be obtained from the mobility spectrum are as follows (Daniel Clem, 2013):

*Average Mobility ( $N_{av}$ )* is the mean value of mobility within the frequency range of 100 to 800 Hz. This value is related to the elastic modulus, thickness, density, and indicates internal defects according to ASTM C1740, which provide guidance on testing plate-like elements.

*Dynamic Stiffness ( $K_d$ )* is the inverse of the slope of the mobility spectrum from 0 to 40 Hz. The dynamic stiffness is affected by the elastic modulus, thickness, support conditions, and presence of internal defects.

*Mobility Slope ( $M_p/N$ )* is the slope of a best-fit line to fit the mobility within the frequency range of 100 to 800 Hz. This parameter is used mainly to detect areas of poorly consolidated concrete.

*Peak-Mean Mobility Ratio or Voids Index ( $v$ )* is the ratio of the peak value of mobility typically below 100 Hz, and the average mobility. High values of Peak-Mean Mobility Ratios indicate debonding, delamination or loss of support beneath a slab-on-ground.

The IR test is performed on a grid of various size and a contour plot is created for each of the above parameters, all obtained from the mobility spectrum. Typically, estimated parameters are compared relative to each other within one test area of comparable boundary conditions. The advantages and limitations of the impulse-response test are provided in Table 2-1.

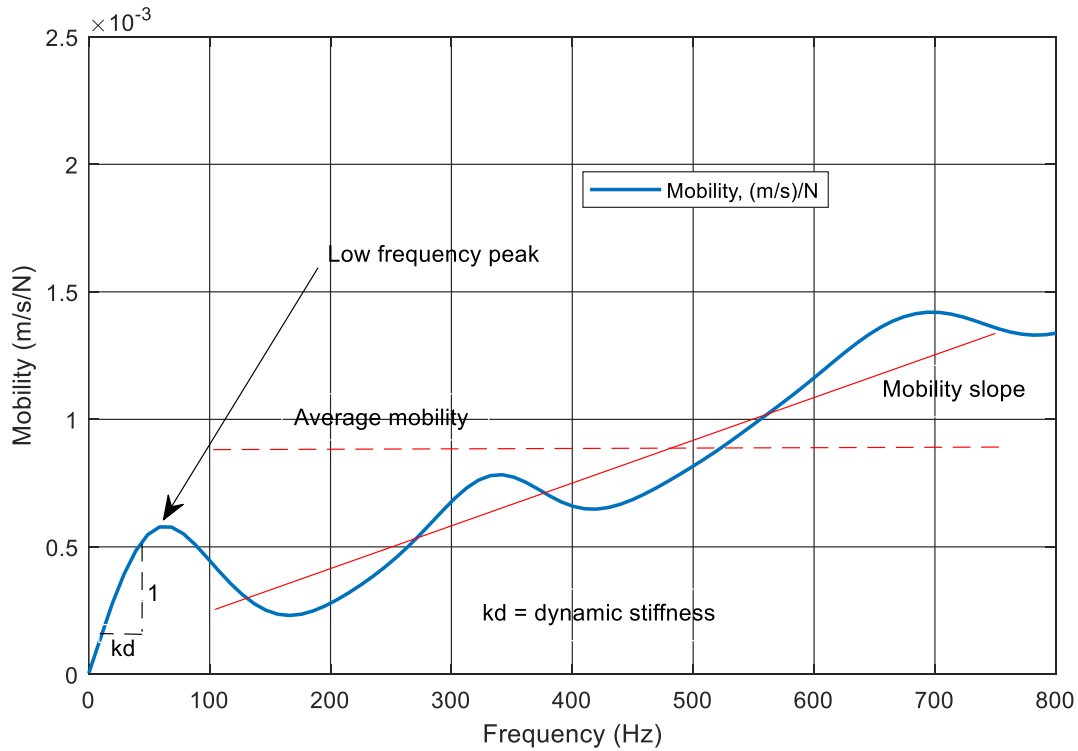


Figure 2-1. Typical mobility plot.

Table 2-1. Advantages and limitations of the impulse-response test.

Advantages	Limitations
Rapid screening method for plate elements	Empirical based method
High robustness compared with other contemporary NDT methods	Edge effects (Sadowski, 2018; Sadowski, Hoła, Czarnecki, & Wang, 2018) and lack of understanding of response of plate element with various boundary conditions in the test
Can be used for the assessment of generally all primary types of defects in concrete	Unknown relative sensitivity of the mobility indices to various defects

In Europe and Asia, IR is primarily used for pile integrity testing, while in North America, it is also used for the condition assessment of plate-like structures such as bridge decks and industrial floor slabs. The basic theory of IR remained the same since 1970, however the range of

applications has been increased (Allen G Davis, 2003). In the following, a historic review is presented.

### 2.3.2 Current State-of-the-Art of Case Studies

The NDT community following the work of Davis and Hertlein (AG Davis & Hertlein, 1987) commenced applying the IR method to structures other than piles. A list (Table 2-2) is provided outlining the case studies with the information of the type of structure being tested, the type of defect, the mobility spectrum parameters being calculated and if any invasive procedure is performed to confirm the IR test results.

Table 2-2. List of case studies involving structures other than drilled shaft piles.

Type of Structure	Type of Defect	Parameters of Mobility Plot	Confirmation using Invasive Probing	Reference
Portland cement concrete pavement	voids beneath pavement and delamination	dynamic stiffness, peak-to-valley difference*	coring confirms the map of the voids and delamination	(Pederson & Senkowski, 1986)
Concrete pavement slabs	quality and integrity of concrete and quality of subgrade support	not specifically mentioned	coring and visual inspection	(AG Davis & Hertlein, 1987)
Bridge deck	honeycombing, debonding and delamination	average mobility, high frequency peaks below 100 Hz	Not reported	(Allan G. Davis & Hertlein, 1990)
Concrete pavement	crack in the slab, voided foundation	dynamic stiffness, flexibility plot (for crack detection)	experiment performed in control environment with pre-knowledge of the anomaly type and extent	(McCavitt, Yates, & Forde, 1992)
Concrete chimney stacks	cracks, delamination and debonding	dynamic stiffness and mean mobility	Coring	(Allen G Davis & Hertlein, 1995)
Mechanical draught cooling towers	Honeycombed concrete, debonding of vinyl-based water proofing layer with concrete surface	mean mobility	confirmed the defects in the repair operation	(Allen G Davis & Hertlein, 1995)

Type of Structure	Type of Defect	Parameters of Mobility Plot	Confirmation using Invasive Probing	Reference
Bridge approach slabs	debonding of the overlay and delamination	dynamic stiffness, average mobility, peak-to-mean mobility ratio	coring at various location confirms the results of IE test and the IR test	(Allen Davis et al., 1996)
Airport runway pavement	honeycombing in different concrete layers	not reported	not reported	(Allen Davis et al., 1996)
Radioactive waste reinforced concrete storage tanks	cracks, delamination, spalling	dynamic stiffness, average mobility, flexibility index (peak-to-mean mobility ratio)	not reported, however the results were confirmed by other NDT methods	(Allen G Davis, Evans, & Hertlein, 1997)
Soil-filled spandrel wall, reinforced concrete arch bridge	poorly consolidated concrete	average mobility	Coring	(Michols, Davis, & Olson, 2001)
Six-span cast-in-place reinforced concrete spandrel arch bridge	freeze-thaw damage and delamination distress	average mobility and mobility slope	coring	(Michols et al., 2001)
Pre-stressed concrete box girders	honeycombing, delamination and loss of post-tensioning	dynamic stiffness and average mobility	surface chipping, visual inspection	(AG Davis & Petersen, 2003)
Integrity of concrete of bridge deck below the asphalt overlay	Delamination	peak-to-mean mobility ratio, dynamic stiffness	Coring	(Allen G Davis, 2003)
Post-tensioned box girders	variability in web thickness, localized internal voiding and debonding of the repair patch and honeycombing	average mobility, mobility slope, void ratio	not reported	(AG Davis, 2004)
Concrete tunnel lining	voids behind concrete tunnel lining	average mobility and dynamic stiffness	Ground penetration radar was used to	(Allen G Davis, Lim, & Petersen, 2005)

Type of Structure	Type of Defect	Parameters of Mobility Plot	Confirmation using Invasive Probing	Reference
Concrete floor overlay over a thick concrete base	debonding of the concrete overlay	dynamic stiffness, average mobility	confirm the voids. No coring is reported coring after confirmation with impact echo	(J Hola, Sadowski, & Schabowicz, 2009)
Bridge deck	delamination in soffit	average mobility	Coring	(Jesper Stærke Clausen & Knudsen, 2009)
Bridge deck	cracks in the underside of the deck	average mobility	Coring	(Jesper S Clausen, Zoidis, & Knudsen, 2012)
Grout beneath steel plates	voids in the grout beneath the steel plate	high peaks in the mobility spectrum	removal of the base plate for repair confirmed the presence of small voids	(Limaye, 2013)
Concrete floor	reduced thickness and voids between concrete floor and its concrete base	average mobility, void index	Coring	(Limaye, 2013; Zoidis et al., 2013)
Thick concrete wall in a hydroelectric dam	visually inaccessible cracks	average mobility and dynamic stiffness	ultrasonic tomography was conducted and no coring information is reported	(Gorzelańczyk, Hoła, Sadowski, & Schabowicz, 2016)
Thick concrete wall in a hydroelectric dam	visually inaccessible cracks	average mobility, dynamic stiffness, peak-mean mobility ratio, average mobility times peak-to-mean mobility ratio, void index	ultrasonic tomography was conducted and no coring information is reported	(Gorzelańczyk, Hoła, Sadowski, & Schabowicz, 2013)
Roof slab of reinforced concrete Antenna pedestal	voids, honeycombing	average mobility and statistical analysis (standard deviation from the mean of the average mobility value)	coring and ultrasonic shear-wave tomography	(Saldua, Dodge, Kolf, & Olson, 2018)

Type of Structure	Type of Defect	Parameters of Mobility Plot	Confirmation using Invasive Probing	Reference
Railway ballasts	contamination of ballast (ballast fouling)	dynamic stiffness	Experiment performed in control environment with pre-knowledge of the anomaly type and extent	(Tamrakar, Nazarian, Garibay, & Azari, 2017)
Bonded concrete overlay on concrete floor in vestibule of freezer	Debonding/delamination	Dynamic stiffness, mobility slop, average mobility and void index	coring	(Sadowski, 2018)

### 2.3.3 Current State-of-the-art of Data Analysis

The first attempt to improve the data analysis and result interpretation of the impulse-response test was a presentation by Clem and Schumacher (Daniel Clem & Shumacher, 2012). They used a parameter termed as “system response” or the mobility in time domain. This is obtained by transforming the mobility spectrum from frequency domain to time domain using inverse Fourier transformation (Eq. 2-2). A typical system response is provided in Figure 2-2. The parameters used for the inference of the condition of the object were maximum mobility amplitude and the exponential rate of decay. The former being related to flexibility whereby large values would possibly be due to delamination while the latter represent the damping whereby large values inferred as possible delamination.

Dodge and Chapa (Dodge and Chapa, 2015) and Saldua et al. (Saldua et al., 2018) suggested a statistical approach to the data analysis for the post processing of IR test for the condition assessment. The expected response of a structure is defined by the mean average mobility value calculated from tests in similar undamaged concrete areas. If average mobility values are greater than 4 standard deviations from the mean response, significant defects are likely to be present. If values are between 2 and 4 standard deviations from the mean response, material variations such as lower density, intermittently bonded cold joints or elevated entrapped air bubbles, are probable. If average mobility values are within 2 standard deviations of the mean response, the result indicates sound concrete. This approach was somewhat similar to the one used by Amick et al.

(Amick, Xiong, Tang, & Gendreau, 2009) in which they developed mobility plots for 22 test points on a slab with soil sub-base. These locations were supposedly without any voids beneath the slab. Almost all the mobility curves had peaks which represent resonance at frequencies above 70 Hz. The authors reported that a slab on a solid subgrade will have resonance at frequencies around 80 Hz and the stiffness is usually constant up to this frequency. These curves were plotted on a logarithmic scale and log mean and  $\pm 1$  sigma limits were defined. Locations which were suspected to have loss of support were tested and the results were shown on the same plot, which were located above the +1 sigma limit with resonance at frequencies around 30 Hz. The voided locations were repaired and the retesting showed that the mobility curves were within the  $\pm 1$  sigma range and higher resonant frequencies.

$$IFFT \left[ \frac{FFT(velocity(t))}{FFT(force(t))} \right] = system\ response(t) \quad (2-2)$$

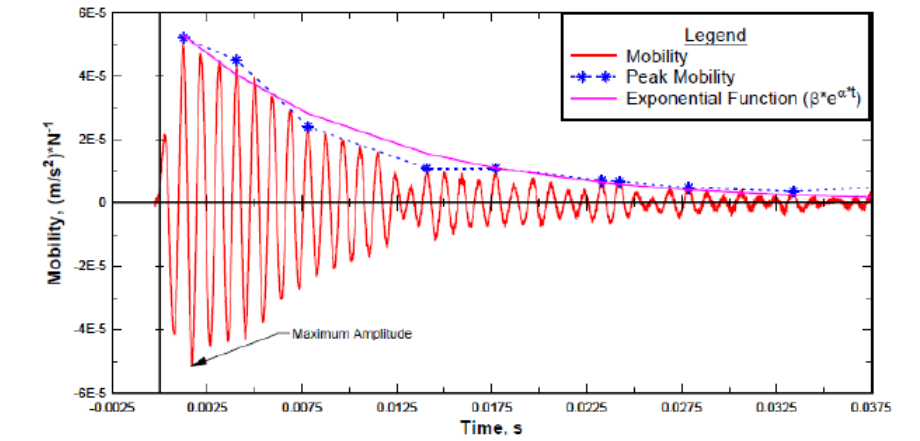


Figure 2-2. Mobility plot in time domain (Daniel Clem & Shumacher, 2012).

#### 2.3.4 Grid Size

A test grid is always established to obtain the impulse-response test data for post processing and subsequently developing contour plot of the response parameters from the mobility spectrum. The size of test grid is supposedly determined by the influence zone of the hammer impact around the test point. Typically, a 1 kg hammer is used in the impulse-response method, which is believed to have an influence zone 600 mm around the impact point (Allen G Davis, 2003; Pederson & Senkowski, 1986). A test grid is recommended to have at least 200 individual points in-order to be representative of an area (Ethan C Dodge & Chapa). Various authors have reported grid size in their studies as presented in Table 2-3. In some projects, after getting highly doubtful mobility

values and non-conclusive results, the mesh sizes were made finer to locate the defects and their extent (AG Davis & Petersen, 2003). Some studies with huge test areas, several representative areas were selected and test grids were laid out in these areas (Jesper Stærke Clausen & Knudsen, 2009). Dodge and Chapa (Dodge and Chapa, 2015) reported that a grid spacing of 300 mm provides an overlap of test point influence area to discount any single high mobility value if the adjoining points do not have high values. Test results from within 300 mm of the edge of a plate-like structure should be disregarded because of the edge effect of the plate on the test results (Breysse, 2012).

Table 2-3. Grid size used in various case studies reported by different authors.

Structure	Geometry/ element type	Grid Size, mm unless otherwise mentioned	Reference
Mechanical Drought Cooling Towers	Rectangular	900 x 900	(Allen G Davis & Hertlein, 1995)
Tunnel lining	circular perimeter	At 60, 120, 240 and 300 degree respectively with the center every 3 m.	(Allen G Davis et al., 2005)
Bridge deck	Plate	800 longitudinal x 300 transverse	(Zheng, Ng, & Ong, 2003)
Bridge deck	Plate	900 longitudinal x 450 transverse	(AG Davis & Petersen, 2003)
Arch Bridge	Arch	1000 x 1000	(Allen G Davis, 2003)
Bridge deck supported by transverse integrally connected concrete beams	Plate	1500 x 1200 and 1500 x 1550	(Allen G Davis, 2003)
Soffit of bridge deck	Plate	1000 x 1000	(Jesper Stærke Clausen & Knudsen, 2009)
Bridge deck	Plate	500 x 1000	(Jesper Stærke Clausen & Knudsen, 2009)

Structure	Geometry/ element type	Grid Size, mm unless otherwise mentioned	Reference
Roof of sewer tunnel	Plate	1000 x 1000	(Jesper Stærke Clausen & Knudsen, 2009)
Bridge deck	Plate	500 x 1000	(Jesper S Clausen et al., 2012)
Side walk	Plate	600 x 600	(Lim & Cao, 2013)
Concrete stair well	Wall	300 x 300	(Lim & Cao, 2013)
Bridge deck	Plate	600 x 600	(Daniel Clem & Shumacher, 2012)
Bridge deck	Plate	600 x 900	(Sadeghnejad et al., 2017)

#### 2.4 Impulse Response Test with other NDT Methods

The preceding section summarized various case studies in which impulse-response test results were verified with various other tests, particularly using the impact-echo test. Combining impulse-response testing with IE testing enhances the efficiency of the NDT evaluation. Schabowicz (Schabowicz, 2015) presented systematic use of the impulse-response test with various other methods for assessing different anomalies in concrete. He presented the methodology for assessing delamination in concrete structures accessible from one side only using impulse-response and IE tests. Similarly, to assess the macro-heterogeneities in concrete structures accessible from one side only, Schabowicz (Schabowicz, 2015) suggested the IR test along with ultrasonic tomography test and collecting cores for verification.

A series of research studies were reported by various authors on estimating the pull-off bond strength between concrete layers using NDT methods, including the impulse-response test. In all these reports, artificial neural network (ANN) based models were used to estimate the pull-off bond strength between concrete layers. The input neurons used for model training, testing and validation were obtained through various NDT methods including the impulse-response test. The optical laser triangulation test is used to obtain  $S_a$  (arithmetical mean height),  $S_q$  (root mean square height) and  $S_{bi}$  (surface bearing index). Impulse-response test is used to obtain  $N_{av}$  (average mobility),  $K_d$  (dynamic stiffness),  $M_p/N$  (mobility slope) and  $v$  (void index). The IE test is used

to obtain  $f_t$  (frequency of the wave reflection from the sample) and  $f_b$  (interlayer bond strength) obtained using pull-off test. The output value of the pull-off adhesion predicted by the artificial neural network (ANN) is  $f_{c,b}$ . The models were trained and tested using experimental data. The details of these studies are summarized in Table 2-4.

As can be seen in the Table 2-4, Sedowski and Hola (Sadowski & Hoła, 2014) used two sets of input neurons. The comparison of the results of both models are provided. Sadowski and Hola (Sadowski & Hoła, 2015) commented on the two sets of input neurons used in the earlier study by Sadowski and Hola (Sadowski & Hoła, 2014) and argued that while the inclusion of impact echo test parameter increases the reliability of the model results, it is affected by the layer thickness. However, the model without the resonant frequency (obtained using IE test) is independent of layer thickness and the reliability of the model is not considerably affected.

The relative error calculated between the interlayer pull-off bond strength obtained using ANN and the same obtained using the standard pull-off test with input neurons;  $S_a$ ,  $S_q$ ,  $N_{av}$ ,  $K_d$ ,  $f_t$  and  $f_b$  ranges from 0.05 to 0.17 (Sadowski, 2015). Furthermore, a practical methodology is given for the pull-off bond strength estimation using several methods including the impulse-response test. Sadowski et al. (Sadowski et al., 2018) used ANN based algorithms with various input parameters to predict the pull-off adhesion for concrete overlay of variable thickness. A total of 15 input parameters were obtained using the 3D laser scanning method, the impulse-response test, IE test, pull-off method and physical thickness measurement at each grid point. Statistical ranking techniques were used to obtain the important parameters as input variables. Czarnecki (Czarnecki, 2017) reported the NDT evaluation pull-off adhesion of the repaired variable thickness overlay on concrete substrate. A total of 7 input variables were used, namely  $S_{pk}$  (reduced peak height),  $S_k$  (core height),  $S_{10z}$  (10 point height),  $T$  (thickness),  $f_t$ ,  $K_d$  and  $v$ . The results of both these studies involving overlay of variable thickness are shown in Table 2-4.

While these studies showing promising results of the use of IR and impact echo test to estimate the interlayer bond strength, there is no mention of the theoretical basis of their application. Rather, these are statistical analyses which use inductive mathematical models and some measures of reliability.

Table 2-4. Summary of the published data on the IR test for inter-layer pull-off strength estimation using pattern recognition based inductive mathematical models.

Input Neurons	IR test input parameters	Linear correlation coefficient (R-squared) between $f_b$ and $f_{c,b}$			Model	Reference
		Training	Testing	Verification		
$S_a, S_q, S_{bi}, N_{av}, K_d, f_b$	$N_{av}, K_d$	0.8175	0.8225	0.8401	Radial Basis Function artificial neural network	(Sadowski, 2013)
$S_a, S_q, N_{av}, K_d, f_t, f_b$	$N_{av}, K_d$	0.9775	0.9725	0.9481	ANN	(Sadowski & Hoła, 2014)
$S_a, S_q, S_{bi}, N_{av}, K_d, f_b$	$N_{av}, K_d$	0.8847	0.8492	0.8989	ANN	(Sadowski & Hoła, 2014)
$N_{av}, K_d, M_p/N, v, f_t, f_b$	$N_{av}, K_d, M_p/N, v$	0.8873	0.8701	0.8441	ANN	(Sadowski, Hoła, & Czarnecki, 2016)
$N_{av}, K_d, M_p/N, v, f_t, f_b$	$N_{av}, K_d, M_p/N, v$	0.844	0.858	0.8968	ANN and Imperialist Competitive Algorithm	(Sadowski, Nikoo, & Nikoo, 2017)
$S_a, K_d, f_b, T$	$N_{av}, K_d, f_t$	0.9691	0.9575	0.9815	MLP-BFGS Network*	(Sadowski et al., 2018)
$N_{av}, K_d, f_t, f_b, T, v$	$N_{av}, K_d, v$	0.9019	0.9031	0.8494	MLP-BFGS Network*	(Sadowski et al., 2018)
$N_{av}, K_d, f_t, f_b, T, M_p/N$	$N_{av}, K_d, M_p/N$	0.8671	0.8816	0.8201	MLP-BFGS Network*	(Sadowski et al., 2018)
$S_{pk}, S_k, S_{10z}, T, f_t, K_d, v$	$K_d, v$	0.844	0.904	0.877	MLP-BFGS Network*	(Czarnecki, 2017)

\*Multi layer perceptron ANN with Broyden-Fletcher-Goldfarb-Shanno learning algorithm.

## 2.5 Impulse Response Test for Deep Foundations

The impulse-response test was developed for the integrity assessment of piles in 1960s in France. Davis and Hertlein (Davis & Hertlein, 1991) and Hertlein and Davis (Hertlein & Davis, 2007) presented the historical development of low-strain pile integrity testing method which latter assumed the name of the impulse-response test. Paquet (Paquet, 1968) presented the basic theory in his article “Vibration Study of Concrete Piles: Harmonic Response” and latter advanced by Davis and Dunn (Allen G Davis & Dunn, 1974). Davis and Dunn (Allen G Davis & Dunn, 1974) reported that there is a relationship between the low-frequency dynamic stiffness measured in the impulse-response test and the static stiffness deduced from the initial elastic portion of the load-settlement curve for a deep foundation load test when 100% recovery is obtained. Most of the case studies and developments in the impulse-response test for pile integrity testing occurred after 1990.

The impulse-response test is extensively used in quality control of cast in-situ concrete piles in Europe and Asia. ASTM D5882 (ASTM-D5882) (in which the impulse-response test is termed as the transient response method) describes the impulse-response test for pile integrity testing. ACI 228.2R (ACI-228.2R-13) presents a number of NDT methods for the condition assessment of piles, such sonic echo, impulse-response, and cross-hole sonic logging (CSL). Various authors have compared these methods for their limitations and advantages. For instance, White et al. (White, Nagy, & Allin, 2008) compared sonic echo and CSL. Rausche et al. (Rausche, Ren-Kungz, & LilcinsJ, 1991) compared the sonic echo method with the impulse-response test in terms of their advantages and limitations. Davis and Kennedy (AG Davis & Kennedy, 1998) used the impulse-response method for the assessment of alkali-aggregate reaction in the concrete drilled shaft foundation of electrical transmission towers. The authors reported successful assessment of concrete integrity in the shafts using impulse-response method as confirmed by computer simulations to match the simulated response with the field tests. In these simulations, the drilled shaft foundations were modeled with three concrete qualities, along with the surrounding soil and the anomalies identified in the field tests. Finno et al. (Finno, Gassman, & Osborn, 1997) and Finno and Gassman (Finno & Gassman, 1998) reported the results of an experimental study and numerical simulations on drilled shaft integrity testing using impulse-response test. The heads of the piles during testing were accessible. They concluded that the use of impulse-response test for integrity testing of piles with accessible heads is limited primarily by the length to diameter ratio

of the shaft, the ratio of the shear wave velocity of the soil to the propagation velocity of the concrete, and the soil stratification.

Pile integrity testing with pile caps is especially challenging given the non-access of the pile top. Hertlein and Walton (Hertlein & Walton, 2000) reported that the impulse-response test is most effective when applied to the pile top and application through pile caps or grade beams has only met limited success. Gassman (Sarah L. Gassman, 1997) reported based on the doctoral research findings, which included experimental work and numerical simulations, that drilled shafts satisfying the assumption of 1-D wave-propagation can be assessed for their integrity using the impulse test with the in-accessible head condition.

To investigate the ability of using a multiple geophone system to minimize the effects of surface waves and reflections from the edges of pile caps for inaccessible-head testing, tests with multiple geophones were performed on the inaccessible drilled shafts at the NGES at Northwestern University as reported by Gassman and Finno (Sarah L Gassman & Finno, 1999). They used multiple geophones on the pile cap to determine the most suitable location to place geophones for maximum resolution of toe and anomaly resonances for various pile cap geometries. It was reported that the geophone placed near the edge of the pile cap gives high toe and anomaly resonances. Also, to further reduce the effect of waves reflected from the boundaries of the pile cap, they suggested using multiple geophones at various locations on the cap surface and developing a composite mobility response as a more general approach.

Gassman and Finno (Sarah L Gassman & Finno, 2000) used the results of experimental studies and numerical simulations, to determine the frequency below which the impulse-response test could be used for in-accessible pile heads. They reported that the geometry of the pile and the pile cap influence the cut-off frequency. The two main geometric factors that limit its applicability are the ratio of the tributary area of the intervening structure above the shaft to the area of the drilled shaft and the ratio of the thickness of the pile cap to the shaft diameter. Furthermore, the geometry of the intervening structure must not undermine one-dimensional wave-propagation conditions in the underlying drilled shaft.

Baxter et al. (Baxter, Islam, & Gassman, 2004) used the numerical simulations to understand the effectiveness of the impulse-response test for condition assessment of pile shafts with and without pile caps. Before this study, numerical simulations had been performed for impact testing based NDT of pile shafts using a 1-D model of the shaft (Liao & Roesset, 1997a, 1997b). In the study of

Baxter et al. (Baxter et al., 2004) the shaft was modelled without the surrounding soil using 2-D and 3-D models and the soil at the base was included. The impulse load of the hammer was applied as a point load on the top of the shaft for the 2-D model; while for the 3D model, it was applied as distributed force over a small area. The piles with caps were modelled as 3-D elements. While both the 2-D and 3-D models accurately predicted the length of the shaft, there was significant difference in the average mobility values for both the models. The calculated average mobility from the 3-D model more accurately predicted the defect-free condition of the shaft. Piles with caps were modelled using a 3-D element. However, the interpretation was more complex due to the reflections from the boundaries of the pile cap and its asymmetry.

Briaud et al. (Briaud, Ballouz, & Nasr, 2002) reported the results of a study in which drilled shafts with deliberate and controlled anomalies were tested for class-A prediction by various NDT companies using the impulse-response test along with other NDT methods. It should be noted that class-A prediction are used to forecast an event before it happens (Lambe, 1973). The purpose of the study was to assess the comparative reliability of the NDT methods under study in predicting anomalies in drilled shafts. The percent success for various types of anomalies at different depths from the top of the shaft is provided in Table 2-5 and will be discussed in the following sections. Lo et al. (Lo, Ni, & Huang, 2010) reported the results of a case study in which bridge piles were scoured and their integrity was assessed. To handle the presence of pile caps, they used “guided impact” on the side of the piles as shown in Figure 2-3. They reported the estimated length of three piles using the impulse-response test. The results were obtained using the mobility plot in frequency domain and in time-frequency domain. The lengths estimated using frequency domain had differences of 3%, 4.9% and -2.4% from the presumed actual value. Similarly, the differences were -1.14%, 5.1% and 7% for the time-frequency domain. The authors suggested that though the error percentage was slightly higher in the time-frequency domain, it is easier to interpret.

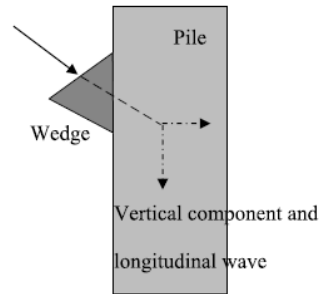


Figure 2-3. Impulse-response test impact configuration used by Lo et al. (Lo et al., 2010) for piles shafts with caps.

Ni et al. (S.-H. Ni, Huang, Lo, & Charng, 2011) estimated the flaw size in drilled shaft piles using the impulse-response test. They used numerical simulations to study the influence of flaw depth ratio ( $R_D$ ), flaw size ratio ( $A_R$ ) and the stiffness ratio ( $k_E$ ) on the resolution of the impulse-response test. These parameters are defined as the ratio of flaw depth to the pile diameter, the ratio of the flaw area to the intact cross sectional area of the pile, and the ratio of Young's modulus of elasticity of the shaft to that of the soil. The resolution is the ratio of the local maxima and local minima of the mobility plot. As this ratio approaches 1.0, it becomes difficult to see the resonance peaks and hence no identifiable shaft length can be deduced from the mobility plot (Finno & Gassman, 1998). The numerical mod was validated by comparing the depth of the flaw in the model with the same as estimated from the mobility plot of the model. They obtained a regression based model to correlate the  $R_D$  (flaw depth ratio =  $F_D/D$ )  $A_R$  (flaw size ratio),  $k_E$  (stiffness ratio =  $k_E = E_c/E_s$ ) and  $P/Q$  from Figure 2-4. This model could be used to assess the flaw size within  $\pm 10\%$  (S.-H. Ni et al., 2011).

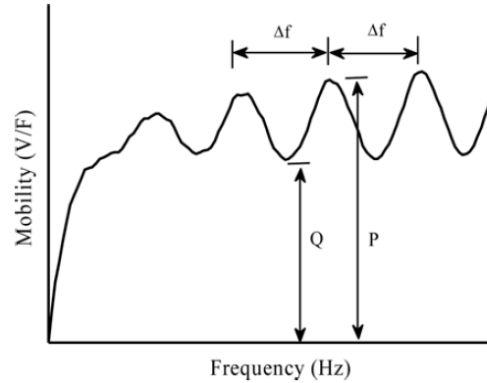


Figure 2-4. Typical mobility plot obtained from the impulse-response test for a pile (S.-H. Ni et al., 2011).

Huang and Ni (Huang & Ni, 2012) carried out an experimental study for integrity assessment of piles with and without pile caps using impulse-response test in comparison with parallel seismic survey and sonic echo tests. They reported that the high mass of the pile cap would absorb most of the energy of the applied impact and thus the magnitude of the reflected wave from the bottom of the shaft was unclear. Furthermore, the reflections from the side boundary of the pile cap likely produced interference and made it difficult to identify the pile toe in the reflected signals.

Abdelrahman (Abdelrahman, 2011) and Khosravi et al. (Khosravi, Abdelrahman, & McCartney, 2012) used the impulse-response test to understand the thermo-mechanical soil-structure interaction for pile shafts due to the inclusion of a ground source heat exchange pump in the deep foundation. Khosravi et al. (2012) treated the foundation as an embedded wave guide for a transient stress-wave applied to the foundation head using an impact hammer. The decrease in the magnitude of elastic wave velocity in the shaft that was observed with increasing temperature implied that due to radial expansion in the reinforced concrete shaft, which increases the soil confinement, and increased stiffness of the surrounding soil. This was consequent in higher energy dissipation of the elastic wave in the shaft. The results from the impulse-response test indicated that the measured wave velocity is sensitive to the change in stress state due to differential thermal expansion of the foundation and soil during temperature changes. The mobility spectrum from the impulse-response test was used to determine the difference between the frequency peaks, which in turn is used to calculate velocity according to Eq. 2-3. Where  $C$  is the wave velocity,  $\Delta f_{ave}$  is the average interval between resonance peaks and  $L$  is the length of the foundation.

$$C = 2\Delta f_{ave}L \quad (2-3)$$

Ni and Huang (S. H. Ni & Huang, 2013) used the impulse-response test for the integrity assessment of pour concrete-cased (PCC) piles. PCC piles are constructed by inserting a steel tube mold to the designed depth with vibrating drive and then pouring the concrete in the steel tube mold. They used numerical simulations validated by experiments in ABAQUS. The soil around the shaft was not modelled to get a higher resolution of the signal. The numerical simulations included intact models and models with a non-axisymmetric defect. The data collected from various sets of impact and sensing location have been presented in this article suggested that the error in length estimation increases as the difference between the sensing location and impact point increases. Furthermore, they also reported that the reliability in correctly determining a defect is low for the surface reflection data in the frequency domain than in the time domain.

Wu and et al. (Wu, Lai, Cheng, & Yang, 2015) reported the results of an experimental study on pile integrity assessment using various surface reflection techniques, including the impulse-response test. The piles had pile caps and they concluded that impulse-response test could not reliably estimate the length of the shaft, however major defects were reportedly identified. The major defects were the 20 mm polystyrene placed at 1.2 m depth of a 3m pile. The information on the cross-section of the defect due to polystyrene foam was not provided. The diameter of the pile was 0.3 m. The study, however, used dimensionally reduced model piles.

Rashidyan (Rashidyan, 2017) suggested the use of modified impact and sensor locations for the surface reflection methods, such as, the impulse-response test, for inaccessible pile heads. Numerical simulations and field investigations were performed to determine foundation properties for collecting data for the Bridge Management Inventory. It was suggested that for an inaccessible pile head, a vertical strike along with a vertically placed sensor is a proper way to conduct impulse-response and sonic-echo tests. It was concluded that the impulse-response test should not be used as a primary tool for shaft length estimation given the lesser reliable results the test furnished in the field studies. It is worth mentioning that for length estimation using impulse-response test, the compressional wave velocity was assumed, hence the error in the length estimation is partly attributed to the error in the assumed valued for the compressional wave velocity. Similar testing arrangement, that is, applying impact and sensors locations are on the side of shaft, was reported by Wang and Chang (Wang & Chang, 2008) using flexure wave testing for piles integrity assessment.

The other main limitation of the impulse-response test besides assessments when the pile head is not accessible, is the high slenderness ratio of the shaft. For long-slender piles ( $L/d > 30$ ) or piles embedded in stiff soil systems, only the initial dynamic stiffness data are obtained, and the subsequent toe reflection data are lost (Popovics, 2003).

## **2.6 Theory behind the Impulse-Response Test for Concrete Structures**

In the preceding sections, it has been shown how the impulse-response test has been used successfully in various case studies of condition assessment and evaluation; however, there is disproportionately less published work on understanding the theory behind the test itself. While the theoretical interpretation of the impulse-response test for the pile integrity testing is provided by Davis and Dunn (Allen G Davis & Dunn, 1974), there are few publications available on such studies for concrete structures other than piles. Unlike the impact-echo test, for which the theory is well established and hence can be used for quantitative assessment, impulse-response test is therefore more of a relative condition assessment technique.

Reddy (Reddy, 1992) used a curve-fitting algorithm with the flexibility response curve (obtained by the integration of mobility spectrum) from impulse-response testing of slabs to extract modal parameters such as static flexibility and maximum flexibility. Two curve-fitting approaches were used. First, a built-in function that extracts the poles and zeros and gain of the flexibility spectrum was used. Second, the curve fitting process given by Desai (Desai, 1991) was utilized. With these extracted parameters, the shear modulus and damping ratio of the subgrade could be computed. Reddy concluded that this flexibility based impulse-response testing produced repeatable results and that the method was successful in locating voids greater than twice the thickness of the slab. Nazarian et al. (Soheil Nazarian, Reddy, & Baker, 1994) presented the details of the flexibility based impulse-response method and case studies to demonstrate its application. Again, the procedure showed its robustness in detecting voids underneath rigid pavements (Soheil Nazarian, Baker, & Crain, 1995).

Nazarian and Reddy (Soheil Nazarian & Reddy, 1996) studied the sensitivity of the impulse-response test for defect detection in rigid pavements. They used numerical simulation and modal time-history analyses to study the effect of thickness and elastic modulus of the slab, the modulus of subgrade of the soil, the length and width of the slab, location of the impact, and size and location of the defects. They adopted a statistical approach to study the effect of each of these

parameters on the mobility plot of rigid pavements on soil sub-base. This study only deals with rigid pavements and no insights are provided on the application of the empirical sensitivity models to other structures or in different situations.

Ottosen et al. (Ottosen, Ristinmaa, & Davis, 2004) used the analogy of a beam on an elastic foundation for the slab on soil and obtained mobility plots using analytical solutions for various cases. The case studied involved a beam having an imperfection in the foundation and the beam having honeycombing with a perfect foundation. According to the analytical solutions, a void in the foundation will increase the mobility dramatically at low frequencies whereas it leaves the mobility curve unchanged for higher frequencies. On the other hand, honeycombing in the concrete will increase the mobility at high frequencies; whereas, the influence for low frequencies is less significant. These conclusions are in good agreement with field experience for concrete slabs resting on soil. However, this approach is tractable for a simple structure like beam, but very complex for application to the other structures. Hola et al. (Jerzy Hola, Sadowski, & Schabowicz, 2011) further explained the equations for the impact, the resulting response and mobility given by Ottosen et al. (Ottosen et al., 2004) using the experimental data.

Clem et al. (DJ Clem et al., 2013) studied the underlying principles of the impulse-response test for detecting delamination in a bridge deck. Finite-element simulations, calibrated with the results of field studies, were used to study the effects of the depth and size of the delamination on the measured parameters of the impulse-response test. They identified the shortcoming of the frequency limit of 800 Hz suggested by the ASTM C1740-16 and suggested that shallow delamination of significance may not be assessed with this frequency limit on the mobility plot. Their finding that useful frequency range in impulse-response test extends beyond 800 Hz is in contradiction with the useful frequency range of 0-1000 Hz given by Davis and Hertlein (Allen G Davis & Hertlein, 1995) and the 0 - 800 Hz suggested by ASTM C1740-16. This limit is based largely on the practical experiences of Dr. Allan G. Davis who initiated the development of the standard practice before his death. Furthermore, they reported that even if the location of a delamination is known, its size cannot be uniquely determined. While this study gives important insights, it only discussed the delamination and the authors suggested further investigations regarding other defect types and using various frequency ranges for the mobility plots.

## 2.7 Reliability of Impulse-Response Test

Being a wave reflection technique, the impulse-response test can identify defects in the material that are greater than the wavelength of the elastic stress-wave used in the test. While the reliability of the impulse-response test in the form of the probability of correctly detecting a defect and the probability of false detection is not well-established, several studies give a glimpse of such information. Regarding the reliability of this test, disproportionate little published work is available for concrete structures other than drilled shafts. A summary of such studies for drilled shafts is provided by Ni et al. (S.-H. Ni et al., 2011) who reported the percentage detection of defects by the impulse-response test and along with other wave reflection methods. Table 2-5 summarize the results of the study reported by Briaud et al. (Briaud et al., 2002).

Table 2-5. Impulse-response test success rate of pile integrity assessment reported by (Briaud et al., 2002).

Type of Defect	Location from the top of the pile	Percent Success of Impulse-response Test
Bulging/Underream	0-8	44
	8-14	25
	0-14	38
Necking	0-8	56
	8-14	38
	0-14	50
Soft Bottom	11.6 - 16.8	15
Mud Cake	0 - 11.6	0
Tremie Displacement	5.3	25
Length	0 – 15	92
	15 – 25	59
	0 – 25	73

Baker & et al. (Barker et al., 1991) reported the study in which one of the objectives were to evaluate several NDT methods including the impulse-response test (termed in the report as transient dynamic response test) for defect detection in drilled shaft piles. A total of 20 piles with

and without defects at sites in California and Texas were used in this study. This document presents an extensive work exploring many dimensions of quality control, acceptance criteria and testing of drilled shaft piles. The results of a portion of piles for only impulse-response test are provided in Table 2-6.

Table 2-6. Impulse-response test results for drilled shaft piles with various planned defects based on (Barker et al., 1991).

Anomaly Category	Anomaly type	Depth to Anomaly (ft.)	% shaft area effected	TDR Detection	Soil Condition
Shaft-area reduction	Inclusion	13	15	No	Dry/dense
	Neck-in	8	48	No	Dry/dense
	Neck-in	43	50	Yes	Wet/soft
Construction and Material related anomaly	Cold-joint	6.5	100	No	Dry/dense
	Weak-concrete	14.5-16.5	100	No	Dry/dense
	Tremie-defect	15	100	Yes	Wet/soft
	Perimeter	5.5-10	92	No	Dry/dense
Soft base	Soft base (mulch)	27	100	Yes	Dry/dense
	Soft base (mulch)	32	300	Yes	Dry/dense
	Soft base (sand/gravel)	33	100	No	Dry/dense

Rix and et al. (Rix, Jacobs, & Reichert, 1993) used several wave reflection techniques, including the impulse-response test for the drilled shafts. The impulse-response test estimated a length of 17.2 m for an actual length of 16.9 m for one pile using measured compressional wave velocity ( $v_c$ ) and Eq. 3-3. The estimated length of the second pile was 18.2 m for an actual length of 21.4 m. The authors reported the presence of partially weathered rock at a depth of 19.5 m. It is worth mentioning here that the impulse-response test was used to estimate length for a measured compressional wave velocity ( $v_c$ ) and the spacing between the peaks ( $\Delta f$ ) in the mobility spectrum. It should however be noted that if the compressional wave velocity of the pile material is assumed, then the error in length estimation is primarily attributed to the error in the assumed value of  $v_c$ . Olson et al. (Olson, Aouad, & Sack, 1998) reported the results of impulse-response testing of a pile with a length of 18.9 m. The impulse-response test showed an anomaly at 10.8 m compared to 11 m of actual depth of the flaw. They, however, reported that the length of the pile

could not be estimated due to the absence of resonant peaks from the bottom of the shaft, presumably due to the extent of the defect.

The authors could not find any published data on the probabilistic reliability of impulse-response test presenting the probability of detection and probability of false alarms. Furthermore, there is no mention of the smallest defect that can be identified using this method for concrete structures other than drilled shafts.

## **2.8 Discussion and Future Perspectives**

A close variant of the impulse-response test has been in use in the aerospace industry for testing and inspection of aircraft components prior to its use for civil engineering structures (Jones & Stiede, 1997). Since then, besides its use in integrity assessment of piles and other concrete structures, the impulse-response test has been used in the assessment of fatigue cracks in steel anchor rods (Keller, Cohen, Pakzad, & Pessiki, 2017). One of the first applications of this method in assessment of voids beneath concrete was to assess the quality of grouting behind the lining of the English Channel Tunnel (Allen G Davis et al., 2005). The method, while praised for being a fast scanning technique, has only been used on relative basis for the condition assessment of concrete elements. The qualitative use of the test is attributed to empirical basis and lack of understanding of the basic theory of the test. The published studies have no theoretical support of how the mobility spectrum indices, as described by ASTM C1740-16 (ASTM-C1740-16, 2016), are influenced by the different type of defects. A specific type of defect may not be necessarily influencing a single index of the mobility spectrum, hence making it difficult to determine the type of defect that might be present in the structure. While the use of multiple NDT tests is recommended for high confidence of results, it is un-economic in-terms of cost of the equipment and training of the testing personnel, which is an important aspect of performing NDT (Carino, 2013). Therefore, given the advantages and its successful employment in various applications as discussed in the preceding sections, further research is needed to develop the impulse-response test as a quantitative test method, like its contemporary IE method. Various authors have cited the benefit of the impulse-response test over its contemporary IE test due to the fact that the former is less sensitive to the presence of embedded steel in concrete and is therefore suitable for condition assessment of thick reinforced concrete members (Cao, 2010; Ethan C. Dodge & Chapa, 2015).

The studies on understanding the theory behind the impulse-response test such as presented by Nazarian and Reddy (Soheil Nazarian & Reddy, 1996), Ottosen et al. (Ottosen et al., 2004) and Clem et al. (DJ Clem et al., 2013) need to be investigated further so that the research questions may be addressed to provide a strong theoretical basis for defect detection by the impulse-response test. Specifically, the following topics should be investigated;

1. The zone of influence of the impact needs to be understood. With this information, the engineer will be in a better position to select the grid size to be used in the field for damage detection in plate-like structures. Numerical simulations of the impulse-response method will be an effective method for addressing this issue.
2. The impulse-response test is used often to check for voids beneath pavements or slabs. The relationship between measured response and void size and thickness of the pavement needs to be investigated in order to determine if a quantitative assessment of void size below pavements is feasible. A comparison needs to be performed with the models developed by Nazarian and Reddy.
3. Experimentally validated numerical simulations should be performed to better understand how the vibrational response of a plate is affected by the presence of honeycombed concrete. It will help in better understanding why the slope of the mobility has been empirically related to the presence of honeycombing.
4. There is a high potential for more advanced methods of data analysis of the signals given the immense development in digital signal processing. In pile integrity assessment, impulse-response test data analyzed using the wavelet transform and the complex continuous wavelet transform have resulted in easier interpretation of the results compared with traditional mobility plot (S.-H. Ni, Yang, & Lyu, 2014; S.-H. Ni, Yang, Tsai, & Chou, 2017).
5. A probabilistic reliability analysis needs to be performed in-order to quantify the probability of defect detection and probability of false alarms using the impulse-response test. Furthermore, the smallest defect that can be detected and the largest defect that can go undetected using this test method needs to be investigated.

## 2.9 Conclusion

While the impulse-response test is used extensively for the condition assessment of concrete structures, there has been relatively few studies on the basic theory of the test as compared to the number of published case studies. After a critical analysis of the published literature and case studies of various applications of the impulse-response test, the following research directions are suggested:

- a. Effect of hammer impact duration and evaluating influence zone of the hammer for optimized grid size for the impulse-response test.
- b. The theory behind the features of the mobility plot that have been correlated empirically to different types of defects.
- c. Quantifying the reliability of impulse-response test results for different types and size of defects.
- d. Improving the interpretation of impulse-response test results using the contemporary signal processing tools.

The above research directions will improve the understanding of different aspects of the impulse-response test, which are explained in the preceding section. Furthermore, these are aimed at establishing a theoretical basis of the test, thereby rendering it as a quantitative assessment method at par with other contemporary stress-wave NDT methods for the condition assessment of concrete elements.

## Acknowledgement

The authors appreciate the review and valuable suggestions of Dr. Nicholas J. Carino, Concrete Technology Consultant in Cleveland, Ohio, United States. The funding for this research by the Natural Science and Engineering Research Council of Canada (NSERC) and McGill University, Canada is also appreciated.

## References

Abdelrahman, S. (2011). *Evaluation of Thermal Soil-Structure interaction in Energy Foundations using an Impulse-Response Test*. (Master of Science Thesis). University of Colorado at Boulder,

- ACI-228.2R-13. *Report on Nondestructive Test Methods for Evaluation of Concrete in Structures*. Retrieved from
- Amick, H., Xiong, B., Tang, N., & Gendreau, M. (2009). Voids Beneath Slabs-on-Ground. *Concrete International*, 31(7), 29-33.
- ASTM-C1740-16. (2016). *Standard practice for evaluating the condition of concrete plates using the impulse-response method*. Retrieved from ASTM International, West Conshohocken, PA, 2016, www.astm.org:
- ASTM-D5882. Standard Test Method for Low Strain Impact Integrity Testing of Deep Foundations. In: ASTM International West Conshohocken, PA, 2016, www.astm.org.
- Barker, R. M., Duncan, J. M., Rojiani, K. B., Ooi, P. S., Tan, C., & Kim, S. (1991). *Manuals for the design of bridge foundations: Shallow foundations, driven piles, retaining walls and abutments, drilled shafts, estimating tolerable movements, and load factor design specifications and commentary*.
- Baxter, S., Islam, M., & Gassman, S. (2004). Impulse response evaluation of drilled shafts with pile caps: modeling and experiment. *Canadian Journal of Civil Engineering*, 31(2), 169-177.
- Breysse, D. (2012). *Non-Destructive Assessment of Concrete Structures: Reliability and Limits of Single and Combined Techniques: State-of-the-Art Report of the RILEM Technical Committee 207-INR* (Vol. 1): Springer Science & Business Media.
- Briaud, J.-L., Ballouz, M., & Nasr, G. (2002). Defect and length predictions by NDT methods for nine bored piles. In *Deep Foundations 2002: An International Perspective on Theory, Design, Construction, and Performance* (pp. 173-192).
- Cao, H. (2010). Techniques for Nondestructive Testing of Concrete Infrastructure at Electric Power Plants. *Materials Evaluation*, 68(7), 778-784.
- Carino, N. J. (2013). Training: Often the missing link in using NDT methods. *Construction and Building Materials*, 38, 1316-1329.
- Clausen, J. S., & Knudsen, A. (2009). *Nondestructive testing of bridge decks and tunnel linings using Impulse Response*. Paper presented at the Proceedings of 10th ACI International Conference on Recent Advances in Concrete Technology, Seville, SP-261-19.

- Clausen, J. S., Zoidis, N., & Knudsen, A. (2012). Onsite measurements of concrete structures using impact-echo and impulse response. *Emerging Technologies in Non-Destructive Testing V*, 117-122.
- Clem, D. (2013). *Evaluation of impulse response & ground-penetrating radar as a means of non-destructive testing of concrete bridge decks*. University of Delaware,
- Clem, D., Popovics, J., Schumacher, T., Oh, T., Ham, S., & Wu, D. (2013). *Understanding the impulse response method applied to concrete bridge decks*. Paper presented at the AIP Conference Proceedings.
- Clem, D., & Shumacher, T. (2012). *A Fresh Look at Impulse Response as a Form of NDT for Concrete Bridge Decks*. Paper presented at the ACI Spring Convention March 18-22, Texas, USA.
- Czarnecki, S. (2017). Non-destructive evaluation of the bond between a concrete added repair layer with variable thickness and a substrate layer using ANN. *Procedia Engineering*, 172, 194-201.
- Davis, A. (2004). Rapid non-destructive test method at the Taiwan High-Speed Rail project. *Concrete Technology*, 30-35.
- Davis, A., & Hertlein, B. (1987). *Nondestructive testing of concrete pavement slabs and floors with the transient dynamic response method*. Paper presented at the Proc Int Conf Struct Faults Repair (Lond).
- Davis, A., Hertlein, B., Lim, M., & Michols, K. (1996). *Impact-Echo and Impulse Response stress wave methods: Advantages and limitations for the evaluation of highway pavement concrete overlays*. Paper presented at the Nondestructive Evaluation of Bridges and Highways.
- Davis, A., & Kennedy, J. (1998). *Impulse Response Testing to Evaluate the Degree of Alkali-aggregate Reaction in Concrete Drilled-shaft Foundations for Electricity Transmission Towers*. Paper presented at the Proc. SPIE.
- Davis, A., & Petersen, C. (2003). *Nondestructive evaluation of prestressed concrete bridges using impulse response*. Paper presented at the Proceedings, Inter. Symp. on Non-Destructive Testing in Civil Engineering (NDT-CE 2003)(Berlin).
- Davis, A. G. (2003). The nondestructive impulse response test in North America: 1985–2001. *NDT & E International*, 36(4), 185-193.

- Davis, A. G., & Dunn, C. (1974). From theory to field experience with the non-destructive vibration testing of piles. *Proceedings of the Institution of Civil Engineers*, 57(4), 571-593.
- Davis, A. G., Evans, J. G., & Hertlein, B. H. (1997). Nondestructive evaluation of concrete radioactive waste tanks. *Journal of performance of constructed facilities*, 11(4), 161-167.
- Davis, A. G., & Hertlein, B. (1990). *Assessment of Bridge Deck Repairs by a Nondestructive Technique*. Paper presented at the NATO Advanced Research Workshop on Bridge Evaluation, Repair and Rehabilitation, Baltimore, Maryland, U.S.A.
- Davis, A. G., & Hertlein, B. H. (1991). Development of nondestructive small-strain methods for testing deep foundations: A review. *Transportation Research Record*(1331).
- Davis, A. G., & Hertlein, B. H. (1995). *Nondestructive testing of concrete chimneys and other structures*. Paper presented at the Nondestructive Evaluation of Aging Structures and Dams.
- Davis, A. G., Lim, M. K., & Petersen, C. G. (2005). Rapid and economical evaluation of concrete tunnel linings with impulse response and impulse radar non-destructive methods. *NDT & E International*, 38(3), 181-186.
- Delatte, N., Chen, S.-e., Maini, N., Parker, N., Agrawal, A., Mylonakis, G., . . . McNeil, S. (2003). Application of nondestructive evaluation to subway tunnel systems. *Transportation Research Record: Journal of the Transportation Research Board*(1845), 127-135.
- Desai, M. R. (1991). *An automated method for construction of surface wave dispersion curve*. (Master of Science). The University of Texas at El Paso, Texas, USA,
- Dodge, E. C., & Chapa, S. V. (2015). *Impulse Response Testing - Analysis of Relative Test Data* Paper presented at the International Symposium on Non-Destructive Testing in Civil Engineering (NDT-CE), Berlin, Germany.
- Finno, R. J., & Gassman, S. L. (1998). Impulse response evaluation of drilled shafts. *Journal of Geotechnical and Geoenvironmental Engineering*, 124(10), 965-975.
- Finno, R. J., Gassman, S. L., & Osborn, P. W. (1997). Non-destructive evaluation of a deep foundation test section at the Northwestern University national geotechnical experimentation site. *A Report Submitted to the Federal Highway Administration Office, Northwestern University, Evanston, Illinois*.
- Gassman, S. L. (1997). *Impulse response evaluation of inaccessible foundations*. (PhD Thesis). Northwestern University, Evanston, Ill,

- Gassman, S. L., & Finno, R. J. (1999). Impulse response evaluation of foundations using multiple geophones. *Journal of performance of constructed facilities*, 13(2), 82-89.
- Gassman, S. L., & Finno, R. J. (2000). Cutoff frequencies for impulse response tests of existing foundations. *Journal of performance of constructed facilities*, 14(1), 11-21.
- Gharaibeh, N., Darter, M., & Heckel, L. (1999). Field performance of continuously reinforced concrete pavement in Illinois. *Transportation Research Record: Journal of the Transportation Research Board*(1684), 44-50.
- Gorzelańczyk, T., Hoła, J., Sadowski, Ł., & Schabowicz, K. (2013). Methodology of nondestructive identification of defective concrete zones in unilaterally accessible massive members. *Journal of Civil Engineering and Management*, 19(6), 775-786.
- Gorzelańczyk, T., Hoła, J., Sadowski, Ł., & Schabowicz, K. (2016). Non-destructive identification of cracks in unilaterally accessible massive concrete walls in hydroelectric power plant. *Archives of Civil and Mechanical Engineering*, 16(3), 413-421.
- Han, N. (2004). Role of NDE in quality control during construction of concrete infrastructures on the basis of service life design. *Construction and Building Materials*, 18(3), 163-172.
- Hertlein, B., & Davis, A. (2007). *Nondestructive testing of deep foundations*: John Wiley & Sons.
- Hertlein, B., & Walton, W. (2000). Assessment and reuse of old foundations. *Transportation Research Record: Journal of the Transportation Research Board*(1736), 48-52.
- Higgs, J. (1979). Integrity testing of concrete piles by shock method. *Concrete*, 13(10).
- Hola, J., Sadowski, L., & Schabowicz, K. (2009). Non-Destructive Evaluation of the Concrete Floor Quality Using Impulse Response S'Mash And Impact-Echo Methods. e. *Journal of Nondestructive Testing*, 14(03).
- Hola, J., Sadowski, L., & Schabowicz, K. (2011). Nondestructive identification of delaminations in concrete floor toppings with acoustic methods. *Automation in Construction*, 20(7), 799-807.
- Huang, Y.-H., & Ni, S.-H. (2012). Experimental study for the evaluation of stress wave approaches on a group pile foundation. *NDT & E International*, 47, 134-143.
- Jones, M. G., & Stiede, P. E. (1997). Comparison of methods for determining specific acoustic impedance. *The Journal of the Acoustical Society of America*, 101(5), 2694-2704.
- Keller, W., Cohen, R., Pakzad, S., & Pessiki, S. (2017). *Rapid detection of fatigue cracking in steel anchor rods using the impulse response method*. Retrieved from

[http://onlinepubs.trb.org/onlinepubs/IDEA/FinalReports/Highway/NCHRP175\\_Final\\_Report.pdf](http://onlinepubs.trb.org/onlinepubs/IDEA/FinalReports/Highway/NCHRP175_Final_Report.pdf)

- Khosravi, A., Abdelrahman, S., & McCartney, J. (2012). Evaluation of Thermal Soil-Structure Interaction in Energy Foundations Using an Impulse-Response Test. In *GeoCongress 2012: State of the Art and Practice in Geotechnical Engineering* (pp. 4466-4475).
- Lambe, T. (1973). Predictions in soil engineering. *Géotechnique*, 23(2), 151-202.
- Leung, C., & Meguid, M. (2011). An experimental study of the effect of local contact loss on the earth pressure distribution on existing tunnel linings. *Tunnelling and Underground Space Technology*, 26(1), 139-145.
- Li, C.-Q., Zheng, J., Lawanwisut, W., & Melchers, R. E. (2007). Concrete delamination caused by steel reinforcement corrosion. *Journal of Materials in Civil Engineering*, 19(7), 591-600.
- Li, C. (2003). Life-cycle modeling of corrosion-affected concrete structures: propagation. *Journal of Structural Engineering*, 129(6), 753-761.
- Liao, S. T., & Roesset, J. M. (1997a). Dynamic response of intact piles to impulse loads. *International Journal for Numerical and Analytical Methods in Geomechanics*, 21(4), 255-275.
- Liao, S. T., & Roesset, J. M. (1997b). Identification of defects in piles through dynamic testing. *International Journal for Numerical and Analytical Methods in Geomechanics*, 21(4), 277-291.
- Lim, M. K., & Cao, H. (2013). Combining multiple NDT methods to improve testing effectiveness. *Construction and Building Materials*, 38, 1310-1315.
- Limaye, H. S. (2013). *Impulse Response Technique: A Valuable Non-Destructive Method to Detect Flaws*. Paper presented at the ASME 2013 Power Conference.
- Lo, K.-F., Ni, S.-H., & Huang, Y.-H. (2010). Non-destructive test for pile beneath bridge in the time, frequency, and time-frequency domains using transient loading. *Nonlinear Dynamics*, 62(1), 349-360.
- McCavitt, N., Yates, M., & Forde, M. (1992). Dynamic stiffness analysis of concrete pavement slabs. *Journal of transportation engineering*, 118(4), 540-556.
- Michols, K., Davis, A., & Olson, C. (2001). Evaluating historic concrete bridges. *Concrete Repair Bulletin*, 14(4), 5-8.

- Nazarian, S., Baker, M., & Crain, K. (1995). Use of seismic pavement analyzer in pavement evaluation. *Transportation Research Record*, 1-8.
- Nazarian, S., & Reddy, S. (1996). Study of parameters affecting impulse response method. *Journal of transportation engineering*, 122(4), 308-315.
- Nazarian, S., Reddy, S., & Baker, M. (1994). Determination of voids under rigid pavements using impulse response method. In *Nondestructive Testing of Pavements and Backcalculation of Moduli: Second Volume*: ASTM International.
- Nazarian, S., Yuan, D., & Tandon, V. (1999). Structural field testing of flexible pavement layers with seismic methods for quality control. *Transportation Research Record: Journal of the Transportation Research Board*(1654), 50-60.
- Ni, S.-H., Huang, Y.-H., Lo, K.-F., & Charng, J.-J. (2011). Estimating the flaw size in drilled shafts using an impulse response method. *KSCE Journal of Civil Engineering*, 15(7), 1197-1207.
- Ni, S.-H., Yang, Y.-Z., & Lyu, C.-R. (2014). *Application of wavelet analysis for the impulse response of pile*. Paper presented at the The 2014 World Congress on Advances in Civil, Environmental and Material Research (ACEM 14) Busan, South Korea.
- Ni, S.-H., Yang, Y.-Z., Tsai, P.-H., & Chou, W.-H. (2017). Evaluation of pile defects using complex continuous wavelet transform analysis. *NDT & E International*, 87, 50-59.
- Ni, S. H., & Huang, Y. H. (2013). Integrity Evaluation of PCC Piles Using the Surface Reflection Method. *Experimental Techniques*, 37(4), 63-73.
- Oh, T. K. (2012). *Defect characterization in concrete elements using vibration analysis and imaging*. (PhD Thesis). PhD Thesis, University of Illinois at Urbana-Champaign,
- Olson, L., Aouad, M., & Sack, D. (1998). Nondestructive diagnosis of drilled shaft foundations. *Transportation Research Record: Journal of the Transportation Research Board*(1633), 120-127.
- Ottosen, N. S., Ristinmaa, M., & Davis, A. G. (2004). Theoretical interpretation of impulse response tests of embedded concrete structures. *Journal of engineering mechanics*, 130(9), 1062-1071.
- Paquet, J. (1968). *Etude Vibratoire des Pieux en Beton: Reponse Harmonique et Impulsionelle, Application au Controle*. Paper presented at the Annales de L'Institut Technique du Batiment et Des Travaux Publics.

- Pederson, C., & Senkowski, L. (1986). Slab Stabilization of Portland Cement Concrete Pavements. *Transportation Research Record*(1083).
- Popovics, J. (2003). NDE techniques for concrete and masonry structures. *Progress in Structural Engineering and Materials*, 5(2), 49-59.
- Rashidyan, S. (2017). *CHARACTERIZATION OF UNKNOWN BRIDGE FOUNDATIONS*. (PhD). University of New Mexico, New Mexico, United States,
- Rausche, F., Ren-Kungz, S., & LilcinsJ, G. (1991). Comparison of Pulse Echo and Transient Response Pile Integrity Test Methods. *Transportation Research Record*(1331).
- Reddy, S. (1992). *Improved impulse response testing: Theoretical and practical validations*. (Master of Science). University of Texas at El Paso,
- Rix, G., Jacobs, L., & Reichert, C. (1993). Evaluation of nondestructive test methods for length, diameter, and stiffness measurements on drilled shafts. *Transportation Research Record*(1415).
- Sadeghnejad, A., Fancy, S. F., Valikhani, A., Chunn, B., Mohammadi, A., Taghinezhadbilondy, R., . . . Lau, K. (2017). *Non-Destructive Testing (NDT) of a Segmental Concrete Bridge Scheduled for Demolition, with a Focus on Condition Assessment and Corrosion Detection of Internal Tendons*. Retrieved from
- Sadowski, Ł. (2013). Non-destructive evaluation of the pull-off adhesion of concrete floor layers using RBF neural network. *Journal of Civil Engineering and Management*, 19(4), 550-560.
- Sadowski, Ł. (2015). Non-destructive identification of pull-off adhesion between concrete layers. *Automation in Construction*, 57, 146-155.
- Sadowski, Ł. (2018). Methodology of the assessment of the interlayer bond in concrete composites using NDT methods. *Journal of adhesion science and Technology*, 32(2), 139-157.
- Sadowski, Ł., & Hoła, J. (2014). New nondestructive way of identifying the values of pull-off adhesion between concrete layers in floors. *Journal of Civil Engineering and Management*, 20(4), 561-569.
- Sadowski, Ł., & Hoła, J. (2015). ANN modeling of pull-off adhesion of concrete layers. *Advances in Engineering Software*, 89, 17-27.
- Sadowski, Ł., Hoła, J., & Czarnecki, S. (2016). Non-destructive neural identification of the bond between concrete layers in existing elements. *Construction and Building Materials*, 127, 49-58.

- Sadowski, Ł., Hoła, J., Czarnecki, S., & Wang, D. (2018). Pull-off adhesion prediction of variable thick overlay to the substrate. *Automation in Construction*, 85, 10-23.
- Sadowski, Ł., Nikoo, M., & Nikoo, M. (2017). Hybrid Metaheuristic-Neural Assessment of the Adhesion in Existing Cement Composites. *Coatings*, 7(4), 49.
- Sadri, A., & Mirkhani, K. (2009). *Wave Propagation Concrete NDT Techniques for Evaluation of Structures and Materials*. Paper presented at the ASPNDE 6th International Workshop NDT Signal Processing.
- Saldua, B. P., Dodge, E. C., Kolf, P. R., & Olson, C. A. (2018). Reinforced concrete antenna pedestal. *Concrete International*, 40(4), 40-42.
- Sansalone, M. (1997). Impact-echo: The complete story. *Structural Journal*, 94(6), 777-786.
- Sansalone, M., & Carino, N. (1986). *Impact-Echo: A Method for Flaw Detection in Concrete Using Transient Stress Waves*, NBSIR 86-3452, National Bureau of Standards, Washington, DC. Retrieved from
- Schabowicz, K. (2015). Modern acoustic techniques for testing concrete structures accessible from one side only. *Archives of Civil and Mechanical Engineering*, 15(4), 1149-1159.
- Tamrakar, P., Nazarian, S., Garibay, J. L., & Azari, H. (2017). Feasibility of impulse response test for characterizing railway ballasts. *Journal of Materials in Civil Engineering*, 30(2), 04017287.
- Wang, H., & Chang, T. (2008). *Non-destructive evaluations of in-service concrete piles by flexural wave approach*. Paper presented at the Proceedings of the 8th International Conference on the Application of Stress-Wave Theory to Piles: Science, Technology, and Practice, Lisbon, Portugal.
- White, B., Nagy, M., & Allin, R. (2008). *Comparing cross-hole sonic logging and low-strain integrity testing results*. Paper presented at the Proceedings of the Eighth International Conference on the Application of Stress Wave Theory to Piles.
- Wu, S., Lai, J., Cheng, C., & Yang, B. (2015). Integrity Testing of Model Piles with Pile Cap. *Proceedings of NDT-CE 2015*, 920-927.
- Yehia, S., Abudayyeh, O., Nabulsi, S., & Abdelqader, I. (2007). Detection of common defects in concrete bridge decks using nondestructive evaluation techniques. *Journal of Bridge Engineering*, 12(2), 215-225.

- Zheng, Y., Ng, K., & Ong, J. (2003). *Evaluation of concrete structures by advanced nondestructive test methods-impact-echo test, impulse response test and radar survey*. Paper presented at the CD Proc. of Int. Symp. Non-Destructive Testing in Civil Engineering-NDT-CE.
- Zoidis, N., Tatsis, E., Vlachopoulos, C., Gotzamanis, A., Clausen, J. S., Aggelis, D. G., & Matikas, T. E. (2013). Inspection, evaluation and repair monitoring of cracked concrete floor using NDT methods. *Construction and Building Materials*, 48, 1302-1308.

### **3. Developing a New Understanding of the Impulse Response Test for Defect Detection in Concrete Plates**

#### **Abstract**

The objective of this research is to develop a technical basis of the impulse-response test for condition assessment and to improve its diagnostics for concrete plates. Impulse-response tests were performed on a fully supported concrete plate with artificial delaminations of various planar sizes at different depths. Defect detection was first performed using the empirical damage indices defined in ASTM C1740, which are based on the shape characteristics of the frequency response function (FRF) between 10 and 800 Hz. Next, the test procedure was modified for extending the frequency range of FRF, revealing that delaminations introduce vibration modes with distinctive high frequencies not present in intact portions of the plate and not detectable in the currently used frequency range of the test due to the hammer tip typically used. A validated 3D finite element model of the experimental plate is used to correlate the dynamic response of test points with experimental FRFs, indicating that the distinctive high frequencies in the extended FRF measured on delaminations correspond to the first bending mode characterized by a local reduction in flexural rigidity and in the damping of the plate. The effect of experimental setups, such as the relative distance between the sensor and the hammer, is shown to have a significant effect on the accuracy of defect delineation for large and shallow delaminations. A new damage index based on the resonant frequency from the extended FRF with a modified experimental setup is proposed for estimating the planar size and depth of delaminations. The performance of the proposed index is demonstrated through experimental data as well as parametric numerical simulations. Multiple regression is used to estimate the detectability, depth, and extent of delaminations as a function of the proposed and currently used damage indices. The resonant frequency is found to be more informative for the planar size of the delamination compared to the depth, while the average accelerance is more informative for the depth of delamination and less for its planar size. Furthermore, the results indicate that the test may have limited detectability and application for delaminations deeper than 300 mm. Finally, the prediction accuracy for the depth and size of delamination is demonstrated based on Gaussian processes and is presented in the form of confidence ellipses. The prediction model is shown to be reasonably accurate for shallow defects

(< 300 mm), which are the most critical for durability and structural performance. While the impulse-response test has been used since the early 1990s for condition assessment of concrete elements other than drilled shaft piles, this study is among the most comprehensive on its physical basis, the influence of experimental setups, the extension of the frequency range, the characterization of delaminations, and detection limitations of the test.

### **Keywords**

Impulse-response test, delamination, mobility spectrum, defect localization, stress-wave propagation, non-destructive testing.

### **3.1 Introduction**

The corrosion and expansion of steel rebars is the main source of delamination in reinforced concrete and is one the main cause for the reduced service life and high-maintenance costs of civil infrastructure (Idorn 1991). Delaminations are not visible unless they are severe enough to result in surface cracking. However, early detection of delamination is critical for timely maintenance and repairs and can only be achieved through the means of non-destructive testing (NDT). The NDT methods are generally used for local level assessment contrary to structural health monitoring which is aimed at global level assessments of a test element or a structure. The basic paradigm of many NDT methods is using controlled excitations on the test element and recording the responses at predetermined locations. Physical factors such as frequency range of the responses, the excitation mechanism, and the locations of sensors on the structure determine the type of NDT method. A number of NDT methods for the condition assessment of concrete elements on local level are documented in ACI 228.2R-13 (ACI). Among these, the most commonly used tests are the impact-echo (ASTM-C1383-15 2015), impulse-response (ASTM-C1740-16 2016), ultrasonic-echo, and ground penetrating radar (ASTM-D6432-11 2011). The impact-echo method is based on the analysis of the propagation and reflection of P-waves due to changes in acoustic impedance in the presence of defects. The test is reliable; however, the time required to perform the test at multiple locations limits its applicability to areas that had previously been targeted as potentially deficient. More recently, air-coupled sensing technology has been introduced to replace contact sensors (Ham and Popovics 2015; Zhu and Popovics 2007), which reduces considerably the time required to perform the test. Nevertheless, performing the test over large surfaces remains time consuming given repeatability issues and difficulties in selecting the impactor for the proper frequency range. The ultrasonic-echo or ultrasonic shear-wave tomography is used to generate 3D

tomograms using the synthetic aperture focusing technique (SAFT) (Aldo et al. 2013). One of the common uses of this method is for the integrity assessment of pre-stressed tendon grouts (Martin et al. 2001). The test provides high resolution assessments but the amount of time required to perform a test is a limiting factor. Ground penetrating radar uses the propagation and reflection of electromagnetic waves as a function of changes in dielectric properties in the presence of defects and reinforcing steel to perform assessments. However, the interpretation of field measurements remains complex and is the subject of ongoing research using innovative data analysis procedures (Sun et al. 2018; Tarussov et al. 2013), and machine learning algorithms (Asadi et al. 2019; Kang et al. 2019). Because it is based on electrical properties of materials, signals are dominated by interactions with the steel reinforcement and other embedded metallic objects, which impairs the assessment of defects located below the steel reinforcement.

### 3.2 Impulse-response Test

The impulse-response test, on the other hand, is a relatively low frequency stress-wave propagation condition assessment method, which is widely used in practice since it requires relatively very little time to perform and can thus be used across large surfaces (Davis 2003). The test was initially developed to verify the integrity of piles (Higgs and Robertson 1979) and subsequently extended for other applications such as bridge decks and floor slabs (Davis and Hertlein 1987), concrete chimneys (Davis and Hertlein 1995), highway pavements (Davis et al. 1996), radioactive waste tanks (Davis et al. 1997), and concrete tunnel linings (Davis et al. 2005). The standard test procedure is described in ASTM C1740-16 (ASTM-C1740-16 2016). To perform the test, an impact is applied at a test point and the velocity time history of the response close to the hammer is recorded. The recommended rubber tipped impactor has a useful frequency range up to 1 kHz. The FRF is defined in Eq. 3-1 (ASTM-C1740-16 2016) and is also referred to as the mobility spectrum or mobility plot.

$$H(\omega) = \frac{V(\omega) \cdot F^*(\omega)}{F(\omega) \cdot F^*(\omega)} \quad (3-1)$$

In Eq. 3-1,  $H(\omega)$  = the mobility spectrum of the velocity FRF;  $F(\omega)$  and  $V(\omega)$  are respectively the Fourier transform of the force-time function from the impactor and the velocity-time function of the sensor, and  $F^*(\omega)$  is the complex conjugate of the Fourier transform of force-time function of the impactor.

Several indices are derived from the mobility spectrum and are used as indicators of different types of defects (Figure 3-1). The dynamic stiffness is defined as the inverse of the slope of the mobility spectrum upto around 40 Hz and the voids index is defined as the ratio of the highest amplitude of the FRF in the range from 0 to 100 Hz range to the average mobility. The average mobility is the average value of the mobility between 100 to 800 Hz. Measurements are typically performed and indices evaluated across a series of grid points drawn at the surface of the test element. Contour plots of the indices are used to identify locations that exhibit anomalies relative to other locations across the test element. The associations between changes in the mobility spectrum indices and the presence of various types of anomalies are based primarily on empirical observations and expert judgment (Davis and Hertlein 1987; Davis et al. 1997; Davis and Hertlein 1995; Davis et al. 1996). Current practice is to limit the mobility spectrum to a maximum frequency of 800 Hz.

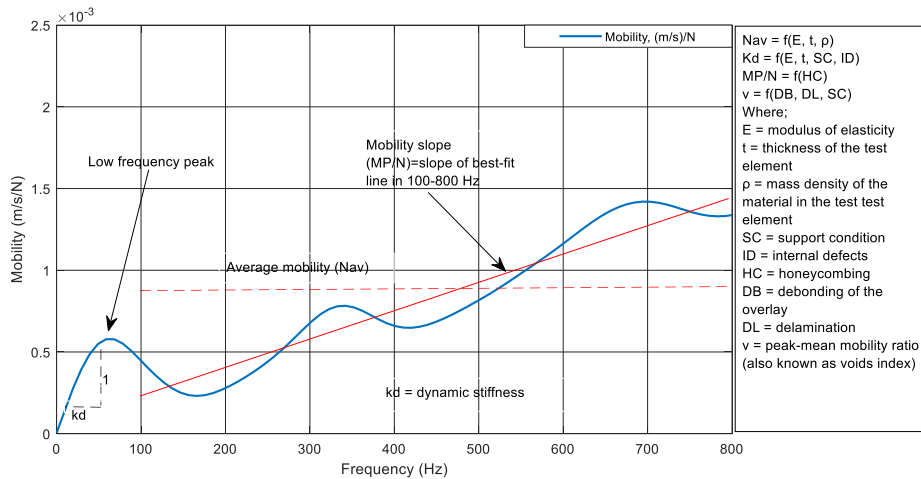


Figure 3-1. Mobility spectrum and definition of mobility indices (ASTM C1740-16).

### 3.3 Motivation and Objectives of Research

The test does not have a well established physical understanding that forms the basis of defect detection with it in concrete elements except for the drilled shaft piles (Davis et al. 1974; Finno and Gassman 1998; Higgs 1979). There are many case studies for the application of the impulse-response test on different types of concrete elements but very few publications on the theoretical basis for the association between the indices and damage (Sajid and Chouinard 2019). Ottossen et al. (2004) provide an analytical solution for the impulse-response test applied to a beam on an elastic foundation. According to their results, the presence of a void at the foundation interface increases the mobility in the low-frequency range, while honeycombing in the beam increases the

mobility in the high frequency range due to a reduction in the damping. A summary of applications of the impulse-response test for various types of condition assessment is provided in Table 3-1. However, in most instances the results and interpretations are empirical and case specific. Many issues remain unanswered such as the effect of the depth and planar size of defects on the response spectrum, on the selection of hammer size and tips to modulate the useful frequency range of the FRF and its influence on assessment, on boundary conditions of test elements, and on the location of the sensor relative to hammer impact sites and to damage location. The objective of this research is to address some of these issues through experimentation and 3D finite element (FE) modeling. In this application, a clamped concrete plate with artificial delaminations of various planar sizes at different depths is used for the experimental part. The plate is clamped to decrease boundary effects for defects near the edges of the plate and to replicate field conditions for concrete gate supports in dam spillways. The experiment and 3D FE model are used to develop an improved interpretation of test results and of the physical response of the plate to impacts in proximity to delaminations. Original contributions relate to fundamental findings demonstrating how standing waves and hence the relative variability of the local dynamic characteristics of the test points form the basis of detection with the impulse-response test, the interaction of a delamination with the test measurements, how detectability of defects can be improved by extending the useful frequency range of the FRF with stiffer hammer tips and stricter control of distances between the impactor and the sensor, and demonstrating for the first time how the impulse response test can be used to obtain probabilistic estimates of the depth and extent of delaminations.

The paper is organized by first describing the experimental specimen and the testing protocols using both currently recommended indices and the proposed modifications. Subsequently, a 3D FE model of the specimen is used to replicate experimental conditions and to characterize the dynamic response of test points during the measurements, model the impact and wave propagation during the test, and investigate the influence of different experimental setups on the results of the test. Next, a parametric study using numerical simulations is performed to investigate the effects of the orientation and extent (size and depth) of delaminations on detectability with the test. Statistical models using Gaussian processes are derived for both the experimental and parametric numerical simulations data, which demonstrate the possibility of using different damage indices to evaluate the planar size and depth of delamination. Finally, the article concludes with a discussion on the significance of the results for damage characterization and on knowledge gaps

to further develop the potential of the impulse-response test for the condition assessment of concrete elements.

Table 3-1. Summary of case studies using the impulse-response test (Sajid and Chouinard 2019)

Type of Structure	Type of Defect	Indices of Mobility Plot	Reference
Concrete pavement slabs	quality and integrity of concrete and quality of subgrade support	not specifically mentioned	(Davis and Hertlein 1987)
Bridge deck	honeycombing, debonding and delamination	average mobility, high amplitude peaks below 100 Hz	(Davis and Hertlein 1990)
Concrete pavement	crack in the slab, voided foundation	dynamic stiffness, flexibility plot (for crack detection)	(McCavitt et al. 1992)
Concrete chimney stacks	cracks, delamination and debonding	dynamic stiffness and mean mobility	(Davis and Hertlein 1995)
Mechanical draught cooling towers	Honeycombed concrete, debonding of vinyl-based water proofing layer with concrete surface	mean mobility	(Davis and Hertlein 1995)
Airport runway pavement	honeycombing in different concrete layers	not reported	(Davis et al. 1996)
Radioactive waste reinforced concrete storage tanks	cracks, delamination, spalling	dynamic stiffness, average mobility, peak-to-mean mobility ratio	(Davis et al. 1997)
Soil-filled spandrel wall, reinforced concrete arch bridge	poorly consolidated concrete	average mobility	(Michols et al. 2001)
Pre-stressed concrete box girders	honeycombing, delamination and loss of post-tensioning	dynamic stiffness and average mobility	(Davis and Petersen 2003)

Type of Structure	Type of Defect	Indices of Mobility Plot	Reference
Integrity of concrete of bridge deck below the asphalt overlay	Delamination	peak-to-mean mobility ratio, dynamic stiffness	(Davis 2003)
Post-tensioned box girders	variability in web thickness, localized internal voiding and debonding of the repair patch and honeycombing	average mobility, mobility slope, peak-to-mean mobility ratio	(Davis 2004)
Concrete tunnel lining	voids behind concrete tunnel lining	average mobility and dynamic stiffness	(Davis et al. 2005)
Concrete floor overlay over a thick concrete base	debonding of the concrete floor overlay	dynamic stiffness, average mobility	(Hola et al. 2009)
Bridge deck	delamination in soffit	average mobility	(Clausen and Knudsen 2009)
Bridge deck	cracks in the underside of the deck	average mobility	(Clausen et al. 2012)
Grout beneath steel plates	voids in the grout beneath the steel plate	high peaks in the mobility spectrum	(Limaye 2013)
Concrete floor	reduced thickness and voids between concrete floor and its concrete base	average mobility, peak-to-mean mobility ratio	(Limaye 2013; Zoidis et al. 2013)
Thick concrete wall in a hydroelectric dam	visually inaccessible cracks	average mobility, dynamic stiffness, peak-to-mean mobility ratio, average mobility times peak-to-mean mobility ratio, voids index	(Gorzelańczyk et al. 2013)
Roof slab of reinforced concrete antenna pedestal	voids, honeycombing	average mobility and statistical analysis (standard deviation from the mean of the average mobility value)	(Saldua et al. 2018)

### 3.4 Experimental Investigation

Tests were performed on a concrete plate with delamination of various planar sizes at different depths (Table 3-2). The experimental plate is 457 mm thick and has planar dimensions of 3,480 mm by 2,500 mm. It was cast on a concrete block with 1 m thickness with nominal planar dimensions of 3,480 mm by 3,480 mm. The base material of the slab was a general-purpose 30 MPa ready mix air-entrained concrete with a nominal mass density of 2,412 kg/m<sup>3</sup>, w=c of 0.57, aggregates combined in ratios of 1:3.3:3.5, and slump of 22 mm. The delaminations were introduced by placing polystyrene foam pieces with a compressive strength of 0.14 MPa (Figure 3-2 and Figure 3-3). The reinforcement steel is provided on the right half of the plate to understand its influence on the detectability of delamination below it. The experimental plate and boundary conditions were designed to replicate defects in concrete supports of the dam spillway gates and to investigate their detection with the impulse response test. Other configurations of concrete elements and boundary conditions are planned to extend the results of this study. The simulation of delamination by introducing polystyrene sheets in concrete elements has been used in several previous experimental studies (Kee et al. 2012; Zhu and Popovics 2007).

Table 3-2. Dimensions and depths of planar defects for the test plate.

Defect ID	Area (mm x mm)	Depth (mm)	Side/depth
A	457 x 457	305	1.5
B	305 x 305	152	2.0
C	305 x 305	38	8.0
D	760 x 760	76.2	10.0
E	305 x 305	114	2.7
F	610 x 610	203	3.0
G	406 x 406	76.2	5.3

The test equipment consisted of a piezo-electric accelerometer, instrumented hammers with plastic and metal tips and a mobile data acquisition system (Table 3-3). Epoxied plates were used to attach accelerometers to the concrete surface to minimise variability in surface contact conditions. More commonly, a dry contact geophone is used to perform the impulse-response test; however, an epoxied accelerometer provides better accuracy for high frequency signal recording, and better

measurement replicability in an experimental setting. For measurements, the accelerometer was located above the approximate center of each defect and the hammer impact applied close to the accelerometer according to ASTM C1740. Measurements were also performed at a location of the plate with no defect for comparison purposes (Figure 3-3). Two impact hammers were used to investigate the effect of impact contact time, which is a function of the stiffness of the hammer tip and the size of the impact area (Figure 3-4). The contact time ( $t_c$ ) of the hammer is used to determine the maximum usable frequency ( $f_{max}$ ) of the FRF according to Eq. 3-2 (Carino 2013; Sajid et al. 2019).

$$f_{max} = 1.5/t_c \quad (3-2)$$

A total of 16384 points at a sampling frequency of 20480 per second were obtained for both the load cell attached to the hammer and the accelerometer. The high sampling frequency and number of records were selected to obtain a resolution of 1.25 Hz in the FRF. A minimum of three repeat measurements were obtained for each test condition to ensure repeatability of the test and to select a representative FRF for analysis. Tests were repeated more times if the three initial FRF were not consistent. In general, good repeatability was observed in most measurements.



Figure 3-2. Concrete formwork and artificial delamination in the plate. (Photo courtesy: Institut de recherche d'Hydro-Québec, Canada).

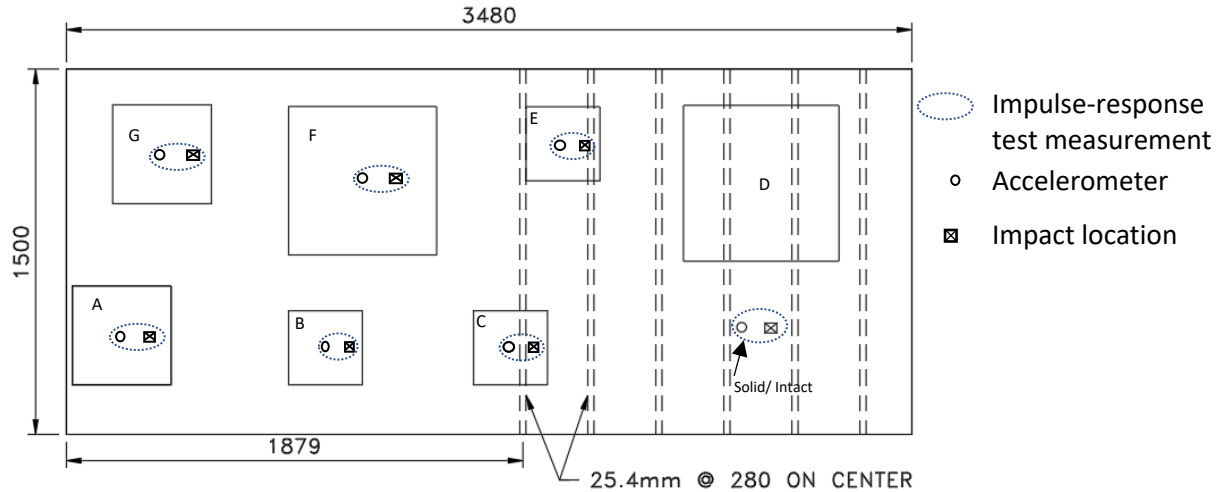


Figure 3-3. Plan view of test plate and artificial delamination (dimensions are in the units of mm).



Figure 3-4. Performing impulse-response test with rubber tipped hammer (left) and steel tipped hammer (right).

Table 3-3. Instrumentation used in testing

Instrument	Notes
Accelerometer	Sensitivity = 100.616 mV/g
Rubber tip hammer	Sensitivity = 0.23 mV/N Upper Frequency range = 800 Hz-1500 Hz
Steel tip hammer	Sensitivity = 0.1 mV/N Upper Frequency range = 2200 Hz-4500 Hz
Data Acquisition system	LMS SCADAS Mobile Upto 204.8 kHz sampling rate per channel

### 3.5 Data Analysis

Data analysis was first performed for measurements obtained with the rubber tip hammer according to the procedure of ASTM C1740. The ASTM procedure uses the velocity FRF or mobility spectrum up to 800 Hz to derive a series of mobility indices. In the following, the acceleration FRF is used instead of the velocity FRF since accelerometers were used for the measurements. Similar results for the resonant frequencies are obtained with either the velocity or acceleration FRFs. The FRF obtained from an acceleration time history is called the accelerance spectrum and is in units of acceleration per unit force. Here, acceleration is expressed in term of g ( $\approx 9.8 \text{ m/s}^2$ ).

The acceleration and the impact time histories from the experiment were used to obtain FRF according to Eq. (3-3), in which  $A(F)$  and  $f(F)$  are respectively the Fourier transforms of the acceleration and impact time-histories. Experimental results show that the shape of the FRF is affected by the presence of delaminations when compared to the FRF for intact regions. For example, Figure 3-5 compares the acceleration FRF above delamination ‘B’ to the FRF at an intact location. The slope of the FRF is steeper for the records above a delamination when compared to the FRF at the intact location. To further characterize the features of the FRF, the average accelerance, accelerance slope, and peak-to-mean accelerance ratio were calculated according to Eq. 3-4, 3-5, and 3-6, respectively. In these equations,  $n$  is the number of ordinates of the acceleration FRF in the range of 100 to 800 Hz, and  $\overline{f(F)}$  and  $\overline{A(F)}$  are mean values of the impact and acceleration respectively in frequency domain, and  $F$  represents the frequency values digitized based on the resolution of FRF.

$$\text{Accelerance} = \left[ \frac{|A(F)|}{|f(F)|} \right] \quad (3-3)$$

$$\text{Average accelerance} = \frac{1}{n} \left[ \frac{|A(F)|}{|f(F)|} \right] \text{ for } 100 \text{ Hz} \leq F \leq 800 \text{ Hz} \quad (3-4)$$

$$\text{Accelerance slope} = \frac{\sum_{i=100 \text{ Hz}}^{800 \text{ Hz}} \left[ (F_i - \overline{F}) \left( \frac{|A(F)|}{|f(F)|_i} - \left( \frac{|A(F)|}{|f(F)|_i} \right) \right) \right]}{\sum_{i=100 \text{ Hz}}^{800 \text{ Hz}} [(F_i - \overline{F})^2]} \quad (3-5)$$

$$\text{Voids index} = \frac{\max[|A(F)|/|f(F)|]}{\text{Average accelerance}} \text{ for } 20 \text{ Hz} \leq F \leq 100 \text{ Hz} \quad (3-6)$$

The average acceleration and acceleration slope are shown in Figure 3-6 for each delamination in comparison with an intact location. These indices from the existing practice are able to distinguish the delaminations relative to the intact location and also the delaminations based on their severity/size and depth. Delamination B, C and E have the same planar dimensions (305mm x 305mm); however, the average acceleration and acceleration slope both decrease with increasing the depth of delamination. The voids index is used in practice as an indicator of a large delamination or missing support for a slab-on-ground (ASTM-C1740-16 2016); however, since by definition it is related to the characteristics of FRF below 100 Hz, it is relevant only for large and shallow defects, which do not correspond to any of the delaminations in the test plate. In the following, delamination D was not considered because it represents an extremely large, shallow and obvious defect that does not follow trends in average acceleration and acceleration slope for hidden (deeper and smaller) defects, which are the primary defects targeted in this study.

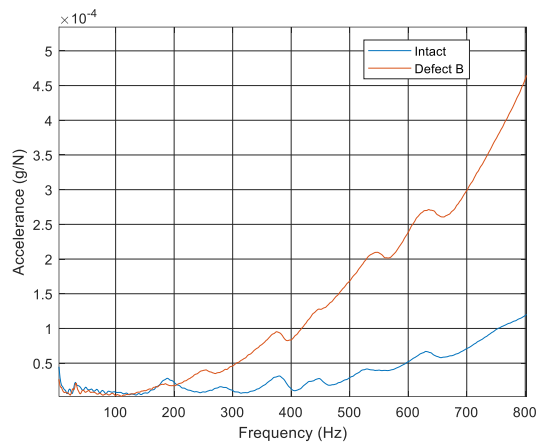


Figure 3-5. Acceleration frequency response function for test at defect 'B' in comparison with intact location.

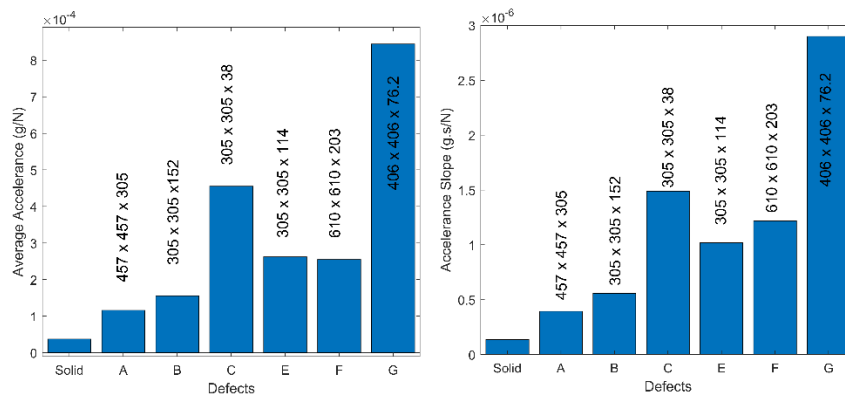


Figure 3-6. Comparison of (a) average accelerance and (b) accelerance slope, for the intact and defect locations.

As mentioned previously, the association between FRF indices and defects is mostly derived from empirical observations and very few studies have related their characteristics to the physical properties of test elements. Clem et al. (2013) proposed that the resonant bending mode frequencies of a defective test element can be larger than 800 Hz and recommended extending the frequency range of the FRF beyond 800 Hz for analysis purposes. However, in their experimental investigations, the authors used a hammer tip with an effective frequency range up to approximately 1.2 kHz and their investigation was limited to a numerical model of a small section of a bridge deck.

In our experimental investigation, a steel tip hammer was used to reduce the contact time and increase the usable frequency range. The contact time was measured from the records of the loadcell on the hammer tip, which can be approximated by a half sine wave where the time period for non-zero contact force defines the contact time. This for the steel hammer was observed to be in the range from 0.0004 to 0.0007 sec, and it implies a usable frequency range 0-2200 Hz according to Eq. 3-2.

High amplitude peaks can be observed in the FRF for tests above delaminations and frequencies above 800 Hz. These high amplitude peaks, which represent modal frequencies at the test locations, occur between 1200 Hz to 2150 Hz and greatly influence the shape of the FRF (Figure 3-7). The dominant frequencies with the corresponding geometrical characteristics of the delaminations are provided in Table 3-4. The peak accelerance for deeper delaminations (A, B, and F) are also shown to be an order of magnitude lower than for shallower ones (E, C, and G). The amplitude of the resonant peak or accelerance is a manifestation of damping for a given stiffness and mass values of the plate above a defect and the significant difference in the accelerance between shallow and deeper defects can be attributed to these properties. Nevertheless, inconsistent distances between the hammer and the sensor seem to also introduce some variability in the measurements. The current literature suggests this distance to be  $100 \pm 25$  mm, but according to the author's best knowledge, there is no published study quantifying this effect. This aspect of the experimental setup is investigated using experimentally validated 3D FE model in the following sections.

Table 3-4. Size and depth of the defects and corresponding amplitudes and frequencies of dominant modes in the experimental FRFs.

Defect ID	Area (mm x mm)	Depth (mm)	Frequency Peak (Hz)	Accelerance ( $10^{-3}$ g/N)	Average Accelerance ( $10^{-4}$ g/N)	Accelerance Slope ( $10^{-7}$ g.s/N)
A	457 x 457	305	1703	2.48	1.01	3.95
B	305 x 305	152	1858	4.85	1.56	5.57
C	305 x 305	38	1787	45.62	4.72	14.90
D	760 x 760	76.2	-----	-----	-----	-----
E	305 x 305	114	2122	62.73	2.81	10.20
F	610 x 610	203	1278	6.72	2.75	12.20
G	406 x 406	76.2	1428	83.59	6.96	29.00

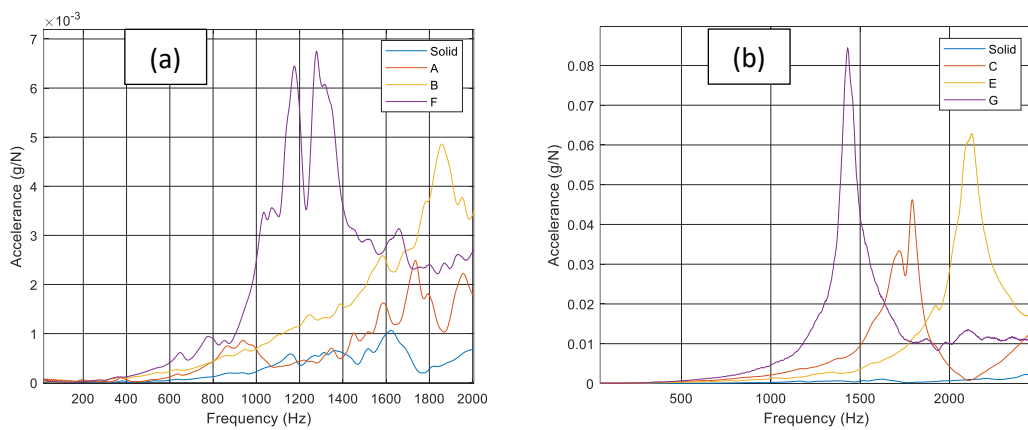


Figure 3-7. Accelerance as a function of frequency for intact location comparison with (a) Defect A, B, and F (b) Defect C, E, and G.

### 3.6 Finite Element Modeling

The purpose of the FE modeling was to investigate the dynamic behaviour of the experimental plate in the vicinity of delaminations, the influence of the different experimental setups on the test results, and demonstrate the wave-propagation during the test.

#### 3.6.1 Dynamic behavior of the Plate in Vicinity of Delaminations

A finite element model of the experimental plate is used to analyse the local dynamic behaviour of the plate above delaminations. The model was developed in ABAQUS® using several layers of plate elements merged together to properly account for the location, planar size, depth and thickness of the delaminations. The 3D FE model developed for experimental plate in Figure 3-2, is shown in Figure 3-8, which shows a good agreement. The delaminations were modeled as voids to account for the presence of the polystyrene foam in the experimental specimen since its elastic modulus and mass density is small in comparison to that of concrete. The concrete is defined with a compressive strength of 30 MPa, an elastic modulus of 24.7 GPa, a mass density of 2300 kg/m<sup>3</sup>, and a Poisson's ratio of 0.2. The reinforcing steel is defined to have an elastic modulus of 200 GPa, mass density of 7850 kg/m<sup>3</sup>, and Poisson's ratio of 0.3. These properties are in comparison with those defined in section 3.4. For amplitude attenuation, Rayleigh damping according to Eq. 3-8 is assumed in the governing equation of the motion in the FE model.

$$[M]\{\ddot{u}\} + [C]\{\dot{u}\} + [K]\{u\} = \{f\} \quad (3-7)$$

$$[C] = \alpha[K] + \beta[M] \quad (3-8)$$

where,  $M$ ,  $C$ , and  $K$  are respectively the nxn mass, damping, and stiffness matrices while  $f$  represents the force vector,  $\alpha$  and  $\beta$  are the stiffness and mass damping constants (Sarma et al. 1998). In this application, only stiffness damping was used for which a trial and adjustment approach was adopted to define  $\alpha=70$  for the concrete. As shown in Figure 3-3, the plate is reinforced with 25.4 mm diameter steel bars in one direction in the top right portion of the plate. This steel reinforcement is influential for the dynamic response of delaminations in the respective vicinity of the plate. The reinforcing steel is modeled with C3D10M elements of 8.0 mm embedded in the concrete plate model. The C3D10M element is a 10-node modified quadratic tetrahedron element in ABAQUS®. The same element is used to model concrete with a maximum element

size of 40 mm (Figure 3-8b). These element sizes of reinforcing steel and concrete are selected after a convergence study.

Fixed boundary conditions were specified at the base of the plate to replicate the boundary conditions of the experimental specimen. The Lanczos algorithm (ABAQUS 2017) was used to calculate the resonant frequencies (eigenvalues) and mode shapes (eigenvectors) of the plate in the frequency range from 0 to 2200 Hz which define the dynamic characteristic of the plate in the vicinity of delaminations in the respective frequency range.

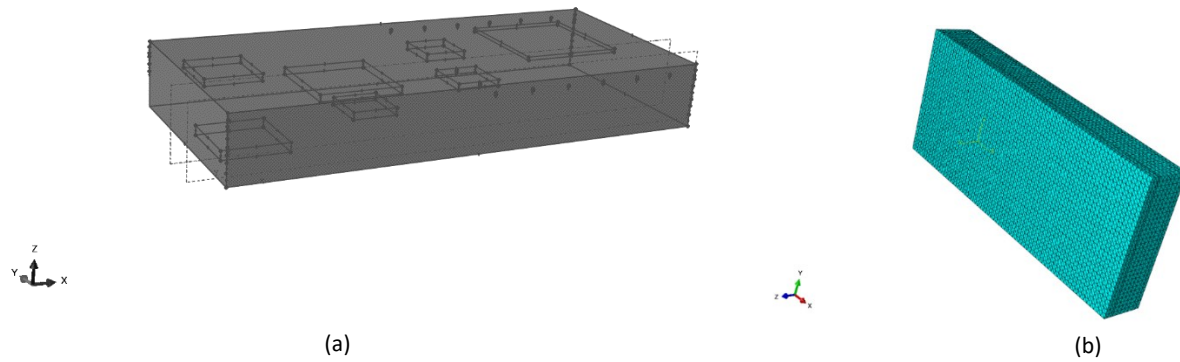


Figure 3-8. (a) Finite element mesh of the test plate, and (b) FE simulated delaminations in ABAQUS®.

The mode shapes in this frequency range correspond mostly to the geometrical features associated with the delaminations. The type of modal response and the associated resonant frequency obtained from the analysis are provided in Table 3-5.

Table 3-5. Resonant frequencies and mode shapes associated with defects.

Defect	Resonant Frequency (FE Model) (Hz)	Resonant Frequency (Experiment) (Hz)	Percent difference (%)	Mode
A	1624	1703	4.639	Bending
B	1859.9	1858	-0.102	Bending
C	1727	1787	3.358	Bending
E	2045	2122	3.629	Bending
F	1312	1278	-2.660	Bending
G	1501	1428	-5.112	Bending

Resonant peaks in the experimental FRF and from the 3D FE model show good agreement (Table 3-5). The analysis of the corresponding mode shapes indicates that peak frequencies in the experimental FRFs correspond to the first local bending mode of the plate above each delamination (Figure 3-9 and Table 3-5). The resonant frequency of these modes is a function of flexural rigidity of the plate, while the acceleration or amplitude of the resonant frequency is a function of damping. The presence of a delamination reduces locally the flexural rigidity of the plate compared to intact locations. The experimental acceleration FRF for the delamination ‘A’ exhibits several low amplitude peaks in the frequency range of 1200-2000 Hz (Figure 3-7a), which corresponds to torsional modes caused by its proximity to the edge of the plate.

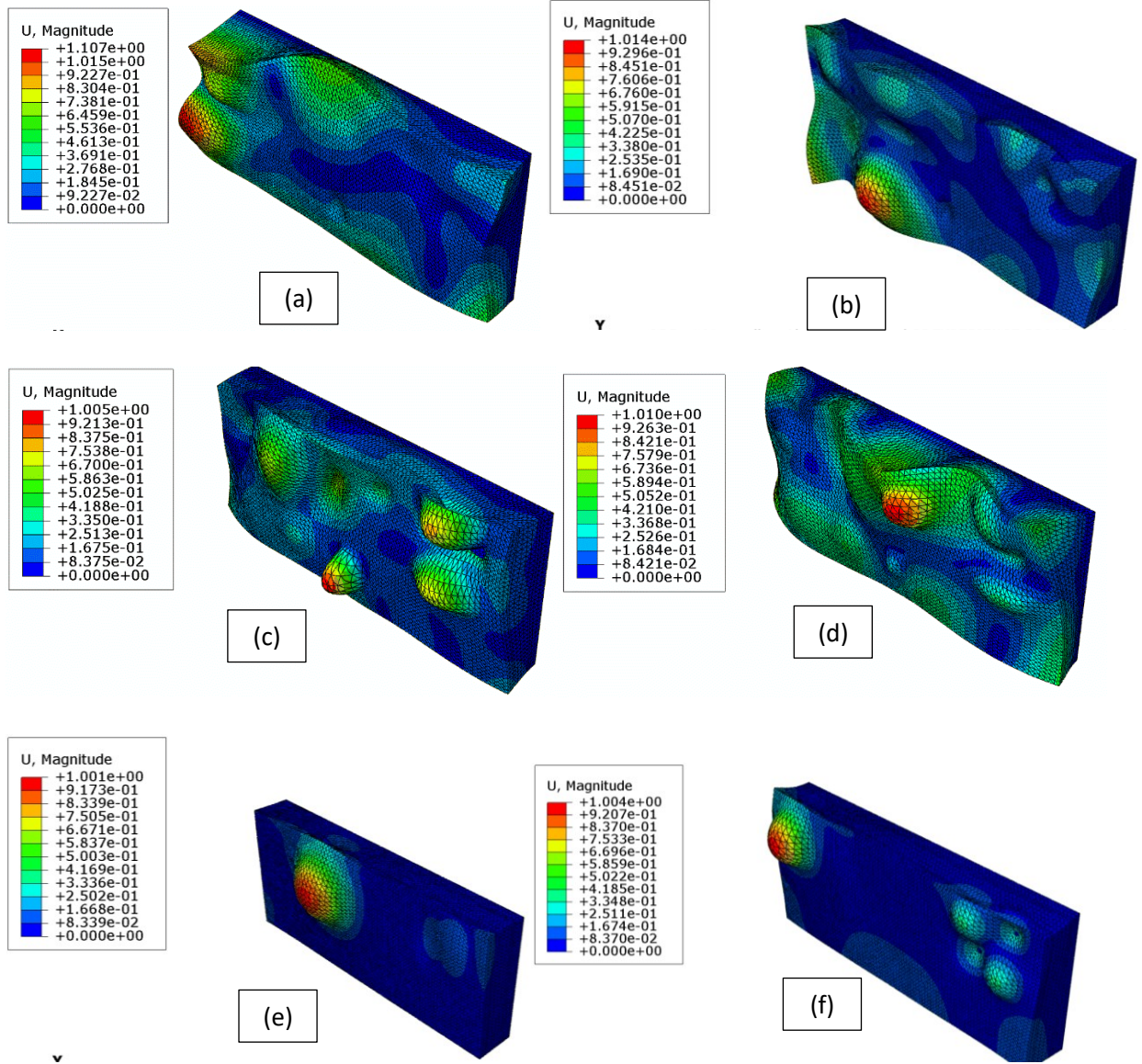


Figure 3-9. Eigen value analysis results showing different mode shapes of the concrete plate associated with a) Defect A b) Defect B and c) Defect C d) Defect E e) Defect F, and f) Defect G.

### 3.6.2 Influence of Experimental Setups

Impulse-response response was simulated on delamination G using the 3D FE model in section 3.6.1 to investigate the effect of the sensor-impactor distance on the acceleration by modelling defect G. The impact was modeled using Eq. 3-9 with a peak amplitude of 0.869 kN and a contact time of 0.0005 sec.

$$F(t) = F_{max} \sin^3\left(\frac{\pi t}{t_c}\right) \quad (3-9)$$

Explicit dynamic analysis was performed to obtain the response time history at the center of the delamination ‘G’ for the impact at 133 mm from the impact location as shown in Figure 3-10a. The FRF is in good agreement with the experimental observations as illustrated in Figure 3-10a for an impact at 125 mm from the sensor. A sensitivity analysis of the accelerance as a function of the sensor-impactor distance shows an inversely linear relationship and that a  $\pm 25$  mm difference in the location of the impact affects the accelerance by  $\pm 30\%$  of the accelerance at 100 mm, which highlights the importance of using consistent impactor-sensor distances and the need of stricter control compared to  $\pm 25$  mm tolerance currently allowed by the standard practice.

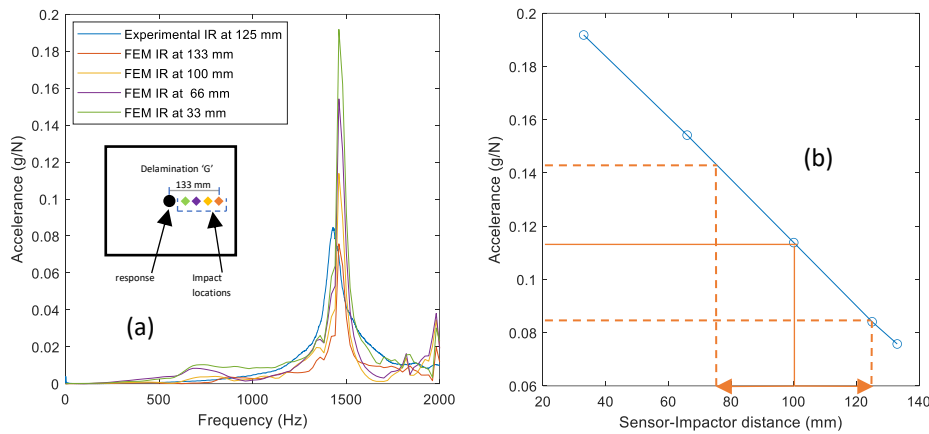


Figure 3-10. FRF for defect G from experiments and numerical simulations for different sensor-impactor distances. (b) Accelerance as a function of sensor-impactor distance.

### 3.6.3 Working Principle of the Test

As shown in the preceding section, the impulse-response test measures primarily the bending response of the concrete elements above a delamination. To further complement the analysis, an elastic stress-wave propagation analysis was performed using ABAQUS® to simulate the wave propagation after the impact during the impulse-response test. The impact is idealized as a cubic half sinewave according to Eq. 3-9. The analysis was performed for the contact time corresponding to an impact with the steel tip hammer (Table 3-1). The simulation shows that the hammer impact generates P, S, and R waves (Figure 3-11a). The P and S waves reflect at the external boundaries of the plate due to changes in the acoustic impedance (Sansalone et al. 1987). After undergoing

multiple reflections, the wave fronts disappear and only stationary waves are observable after 650  $\mu\text{s}$  (Figure 3-11b).

The modes of vibration excited by the impact depend on the frequency content of the impact, which is a function of the contact time. The rubber tip hammer used in the impulse response test has long contact times, which limits the useful frequency range to around 1 kHz. In addition, given the relatively long time during which measurements are recorded (0.8s), the low frequency flexural modes dominate and quickly evolve into stationary waves. By contrast, the impact-echo test is recorded over much shorter periods of time and measurements are primarily of wave propagation and reflection. Given the test uses stationary waves, relative variation in the local dynamic characteristic of test points forms the basis of detection with the impulse-response test unlike the impact-echo test in which the detection is performed based on the reflections of p-waves due to changes in material impedances.

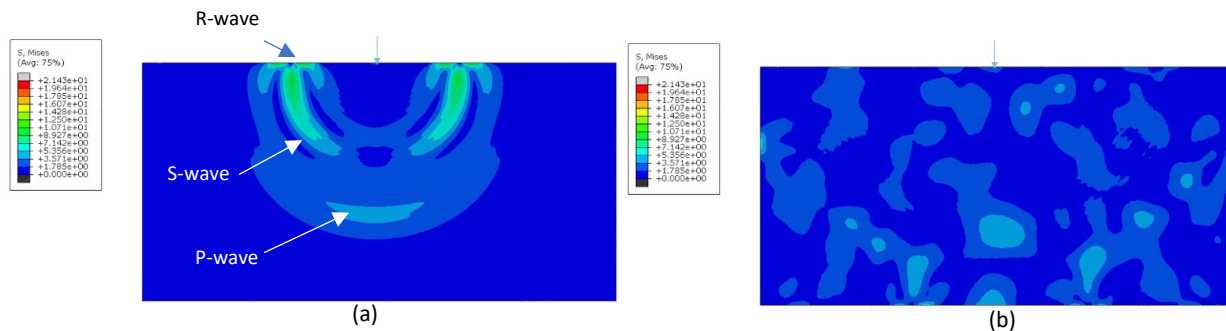


Figure 3-11. Wave propagation analysis after impact. (a) Wave components 90 microseconds after impact. (b) Standing waves at 650 microseconds after the impact.

### 3.7 Defect Localization Limiting Extent of Detectability

Traditionally, the impulse-response test has only been used for anomaly detection through an empirical analysis of the spatial variation of the average mobility, the mobility slope, the dynamic stiffness, and the voids index. Anomaly characterization in terms of size and depth typically relies on more refined yet time-consuming stress-wave methods, such as the impact-echo and ultrasonic shear-wave tomography. This section investigates the relation between FRF features and the geometrical characteristics (size and depth) of delaminations and their predictability using statistical procedures.

The potential for defect characterization with the impulse response test is investigated through a combination of numerical simulations based parametric study and experimental results. The

impulse-response test was modeled in ABAQUS for a 500 mm thick clamped concrete plate with dimensions of 2000 mm by 2000 mm, a mass density of 2400 kg/m<sup>3</sup>, elastic modulus of 33 GPa and Poisson's ratio of the 0.2. The damping for this analysis was defined as  $\alpha = 10$  (in Eq. 3-8) and the impact was modelled as a cubic half sine wave function (Eq. 3-9) of low intensity to constrain the amplitude for the FRF. Delamination of different sizes (Table 3-6) were investigated for a contact time of 0.0005 sec with an impactor-sensor distance of 100 mm, which provides a theoretical useful frequency range up to 3 kHz (Eq. 3-2). Explicit dynamic analyses were performed to generate the response time histories at a node above the center of each delamination for an impact at 100 mm horizontal spacing. The time histories of the response and the impact were then used to obtain the FRF according to Eq. 3-3 as well as the average accelerance, and accelerance slope according to Eq. 3-4 and 3-5 respectively. According to Table 3-6, similar trends between FRF parameters and the geometry of delaminations are observed in the results from numerical simulations and experiment measurements.

Table 3-6. Geometrical characteristics of the delaminations for the parametric study and corresponding FRF indices.

Size (mm)	Depth (mm)	Frequenc y (Hz)	Acceleranc e (g/N)	Average Accelerance (g/N) x10 <sup>-5</sup>	Accelerance Slope (g.s/N) x 10 <sup>-8</sup>
350	100	1867	0.00050	7.43	1.99
450	100	1505	0.00172	11.6	3.18
450	150	1573	0.00058	5.43	1.56
450	200	1593	0.00051	2.29	0.18
550	100	1143	0.00095	5.93	1.37
550	150	1300	0.00036	11.6	2.76
550	200	1329	0.00018	13.9	3.91

Multiple linear regression (MLR) analyses performed on both experimental (Table 3-5) and numerical data (Table 3-6), for which the natural log values of size and depth are used as explanatory variables and the natural log of each index (resonant frequency, peak accelerance, average accelerance, and accelerance slope) as predicted. The exponential of the MLR parameters is used to obtain the equations given in each of Figure 3-12 to Figure 3-15, which were used to calculate these curves. It is evident that the planar size and depth of delaminations are statistically

significant for the prediction of the peak frequency (Table 3-7 and Table 3-8, Figure 3-12). The results also indicate that the peak frequency tends towards a constant value for depths greater than 200 mm. The depth and planar size of delaminations are not as statistically significant for the prediction of the accelerance. The experimental results also indicate that the accelerance tends to a constant value for delaminations at depths greater than 150 mm (Figure 3-13). Results for the numerical model confirms the trends observed experimentally for the accelerance. The prediction models for the average accelerance (Figure 3-14) and accelerance slope (Figure 3-15) show similar trends as a function of the size and depth of delamination for both the experimental and the numerical data sets. The results for the experimental data set are statistically more significant than for the numerical data set, which can be explained by the influence of damping on the amplitude of accelerance and the difficulty in specifying damping in numerical models. In conclusion, the peak frequency appears to be influenced mainly by the size of defects while the average accelerance and accelerance slope are more sensitive to the depth of delamination than the peak frequency. The results indicate that both the peak frequency and average accelerance can be used to predict the size and depth of defects.

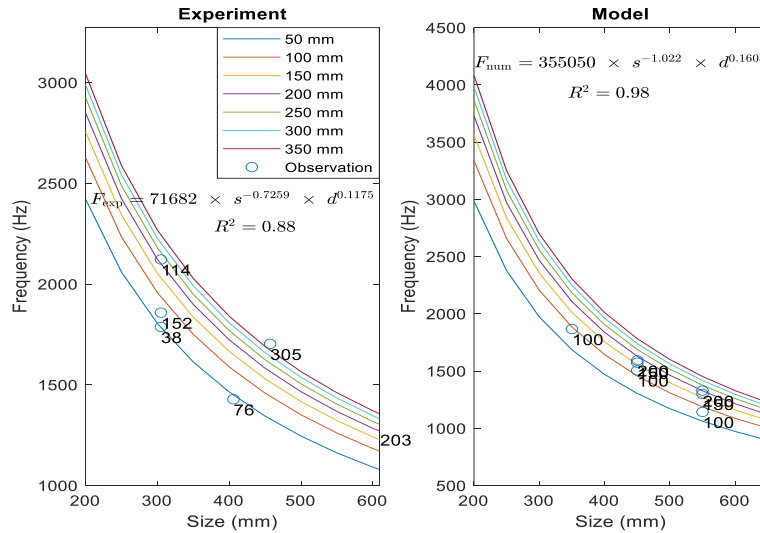


Figure 3-12. Peak frequency as a function of the size and depth of defects for the experimental data (left), and numerical simulations (right).

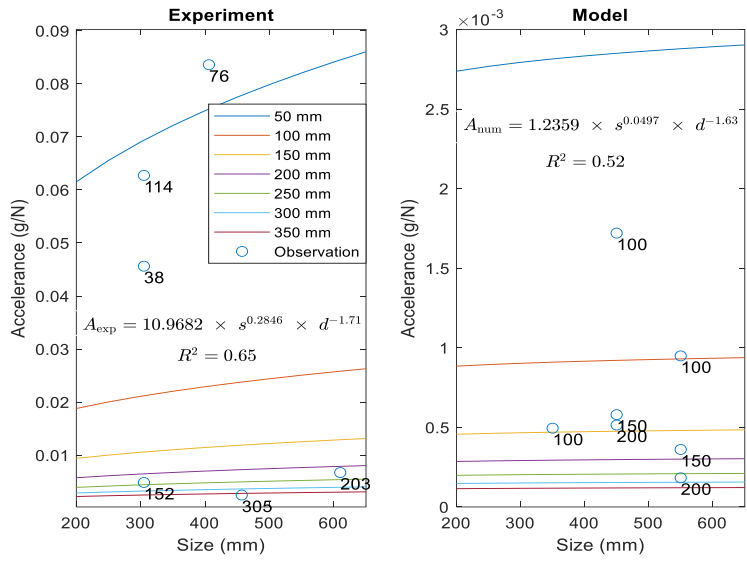


Figure 3-13. Accelerance as a function of the size and depth of defects for the experimental data (left) and the numerical simulations (right).

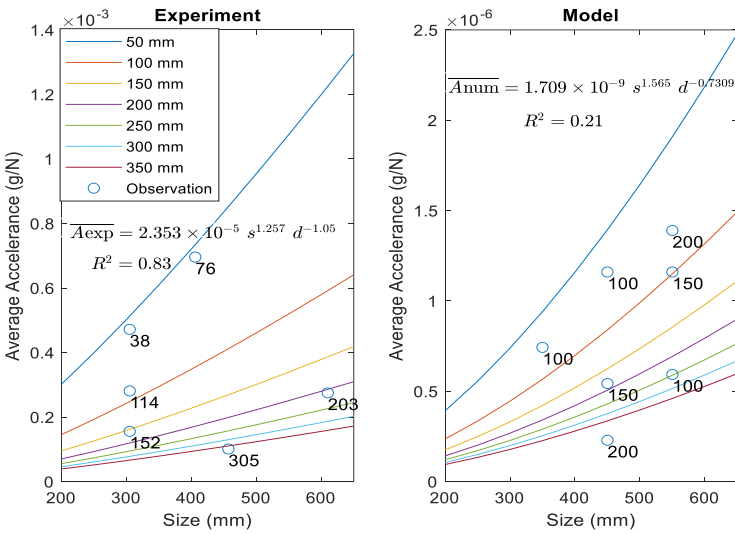


Figure 3-14. Average Accelerance as a function of the size and depth of defects for the experimental data (left) and the numerical simulations (right)

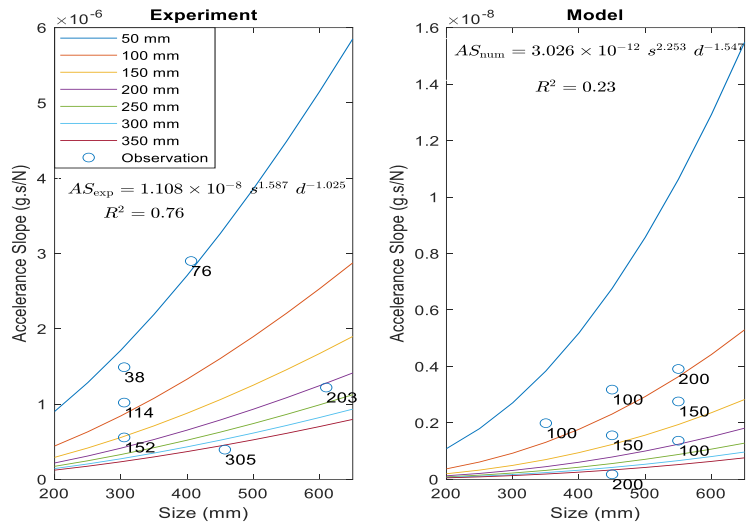


Figure 3-15. Accelerance slope as a function of the size and depth of defects for experimental data (left) and the numerical simulations (right).

Table 3-7. Results of statistical analysis of the experimental measurements for number of observations of n=6 for each case.

FRF	R <sup>2</sup>	Adj. R <sup>2</sup>	SE	Parameter	Estimate	t-statistic	P-value
Frequency	0.8793	0.7988	0.0205	Intercept	71682	13.801	0.001
				Size	-0.726	-4.596	0.019
				Depth	0.117	1.928	0.149
Accelerance	0.656	0.4266	3.9028	Intercept	355050	0.214	0.844
				Size	0.285	0.131	0.904
				Depth	-1.710	-2.034	0.135
Average Accelerance	0.8329	0.7215	0.4141	Intercept	-10.657	-2.927	0.061
				Size	1.257	1.770	0.175
				Depth	-1.050	-3.833	0.031
Accelerance Slope	0.7636	0.6061	0.5987	Intercept	-18.318	-4.185	0.025
				Size	1.587	1.859	0.160
				Depth	-1.025	-3.112	0.053

Table 3-8. Results of statistical analysis for numerical simulations based parametric study. The number of observations is 7 for each case.

FRF	R <sup>2</sup>	Adj.	SE	Parameter	Estimate	t-	P-value
Parameter		R <sup>2</sup>				statistic	
Frequency	0.9755	0.9632	0.031	Intercept	12.785	27.236	0.000
				Size	-1.022	-12.600	0.000
				Depth	0.161	3.766	0.020
Accelerance	0.5246	0.2868	1.4286	Intercept	0.212	0.023	0.982
				Size	0.050	0.032	0.976
				Depth	-1.630	-1.979	0.119
Average	0.2052	-	1.8423	Intercept	-20.187	-1.964	0.121
				Size	1.565	0.882	0.428
				Depth	-0.731	-0.782	0.478
Accelerance	0.2348	-	4.9262	Intercept	-26.524	-1.578	0.190
				Size	2.253	0.776	0.481
				Depth	-1.547	-1.012	0.369

A prediction model for the size and depth of delaminations as a function of the peak frequency and average accelerance is derived by using Gaussian processes. The procedure is first applied using the peak frequency as a predictor followed by a model using both the peak frequency and the average accelerance as predictors. Gaussian processes refer to the joint distribution of input and output functions and is defined by a mean value vector (Eq. 3-10) and covariance matrix (Eq. 3-11) where  $\underline{X}_1$  and  $\underline{X}_2$  represent respectively the vectors of predicted (output) and predictor (input) variables (Schulz et al. 2018).

$$\begin{bmatrix} \underline{\mu}_1 \\ \underline{\mu}_2 \end{bmatrix} \quad (3-10)$$

$$\begin{bmatrix} \Sigma_{11} & \Sigma_{12} \\ \Sigma_{21} & \Sigma_{22} \end{bmatrix} \quad (3-11)$$

Where  $\underline{X}_1 = \begin{bmatrix} \ln(size) \\ \ln(depth) \end{bmatrix}$  and  $X_2 = [\ln(Peak Frequency)]$  or  $\underline{X}_2 = \begin{bmatrix} \ln(Peak Frequency) \\ \ln(Average Accelerance) \end{bmatrix}$

The theory of Gaussian Processes can be used to obtain the conditional mean value vector of outputs as a function of the observed inputs, in this instance, the predicted mean size and mean depth of defects as well as their updated variance given the observed peak frequency (or peak frequency and average accelerance).

$$\underline{\mu}_{1|2} = \underline{\mu}_1 + \Sigma_{12}\Sigma_{22}^{-1}(\underline{x}_2 - \underline{\mu}_2) \quad (3-12)$$

$$\Sigma_{1|2} = \Sigma_{11} - \Sigma_{12}\Sigma_{22}^{-1}\Sigma_{21} \quad (3-13)$$

The diagonal terms of the covariance matrix in Eq. 3-13 provide the updated variance for the predicted size and depth of the defects, while the off-diagonal terms provide the covariance between the two values. The covariance between size and depth is not significant in this application given that it only represents the relationship for the experimental plate and is not representative of actual defects. The updated mean value vector and variances are used to illustrate the predictive ability of the model for each of the defects by comparing the observed size and depth to the 50% and 95% prediction ellipses using the Peak Frequency (Figure 3-16a) and Peak Frequency and Average Accelerance together (Figure 3-16b). The level of variability for the prediction of defects is reflected in the size of the ellipses and the fact that some defects fall within the 50% confidence intervals (CI) and others fall between the 50% and 95% CI is within what should be expected given the small sample of defects. The elongated shape of the ellipses reflects the larger uncertainties associated with the prediction of the depth of the delaminations in comparison to their size. The results indicate that the level of the uncertainty for the prediction of the depth of shallow defects, which are the most critical from a durability perspective, is greatly reduced by using both the Peak frequency and the Average Accelerance as predictors.

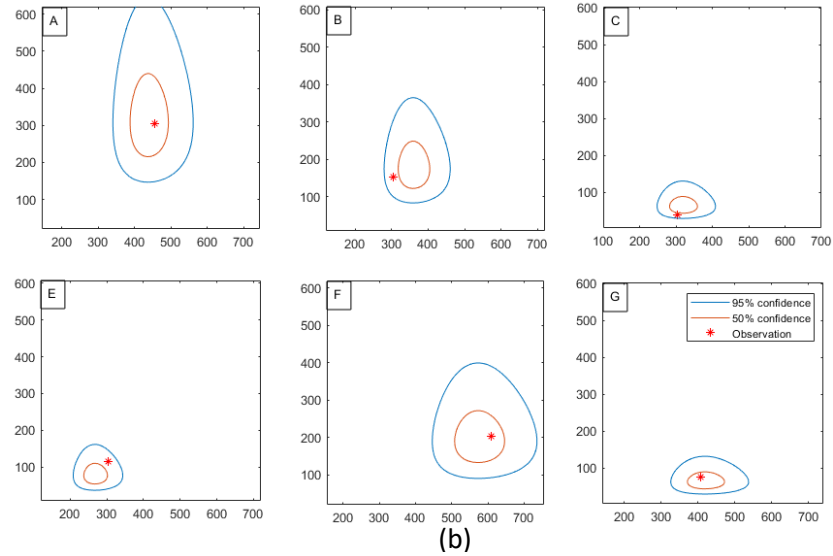
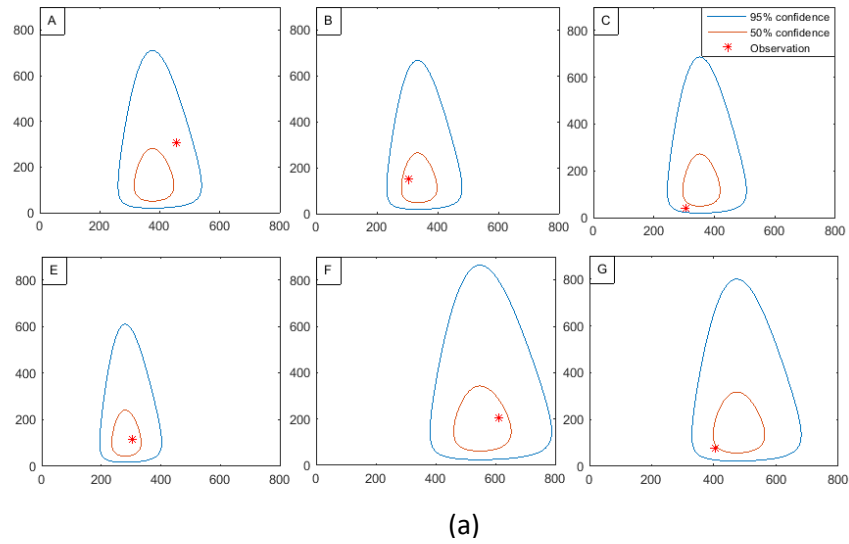


Figure 3-16. Error ellipsoids for prediction with 95% and 50% confidence levels obtained using correlation analysis for each delamination using (a) frequency, and (b) frequency and average Accelerance. The letters on each subplot represents the respective delamination and the vertical and horizontal axes represents the depth and planar size respectively in mm.

### 3.8 Discussion and Conclusions

Experiments and 3D FE models were used in this study to: 1) Demonstrate how the stationary waves form the basis of detection of defects with the impulse response test, 2) Investigate the interaction between delaminations and stress-waves generated during the test, 3) Investigate

benefits of extending the usable frequency range of the test, 4) Evaluate the impact of impactor-sensor distances on FRF indices, 4) And investigate the detectability and characterization of delaminations as a function of their planar sizes and depths.

First, experiments were performed to investigate the effect of the size and depth of delamination on the acceleration FRF and empirical indices defined in ASTM C1740-16, which are shown to be noticeably sensitive to the presence of delaminations. The experimental procedure was modified by using a steel hammer tip to extend the usable frequency range of the test, which reveals resonant frequencies up to 2200 Hz when delaminations are present.

A comparison between experimental FRFs and the frequency analysis of the 3D FE model of the plate reveals that the first flexural vibration mode of the plate above a delamination corresponds to the peak frequencies observed in the experimental FRFs. Furthermore, results indicate that the defect detection with impulse response test is based on the characteristics of standing waves, which are dominated by the first flexural mode of the plate above a delamination with peak frequencies between 800 Hz and 2000 Hz. This confirms that the basis of detection with the impulse-response test is the relative variation of the local dynamic properties of the test points unlike the reflection based NDT methods such as impact-echo which works on the basis of the reflection of p-waves due to changes in material impedance.

The influence of the sensor-hammer distance is quantified using the experimentally validated 3D FE model and the results indicate the need to use a consistent sensor-hammer distance throughout testing to limit the variability in FRF parameters. This effect can be especially significant for shallow delaminations. The authors recommend to have a stricter criteria of  $100 \pm 10$  mm replacing the currently provided  $100 \pm 25$  mm by ASTM C1740 for the test.

Statistical analyses were performed to investigate the diagnostic value of the impulse response test for defect characterization. Current recommended damage indices derived from the FRF were investigated in addition to the resonant frequency of the FRF as predictors for the size and depth of a delamination. The peak frequency was found to be very informative in relation to the planar size of delamination, while the average acceleration and acceleration slope both are informative in the relation to the depth of delamination, especially for depths up to 200 mm. In addition to the estimates of mean delamination size and depth, the Gaussian process equations provide estimates on the accuracy of these predictions. The results indicate that the prediction accuracy of the test is

greatly increased for both size and depth of a delamination by using resonant frequency in conjunction with the average accelerance.

The prediction model is shown to be mostly accurate for shallow delaminations (< 300 mm), which are the most critical for durability and structural performance. The statistical analyses also indicate that the impulse-response test may have limited detectability for delaminations greater than 300 mm. The next steps in this research is to investigate the effect of different support conditions for the plate, the geometrical shape of delaminations (e.g. circular, rectangular), and other types of defects (e.g. honeycombing).

### **Data Availability Statement**

The data for statistical analyses is provided in the respective tables of this manuscript. The raw data for the generation of FRFs may be provided on request and approval from Institut de recherche d'Hydro-Québec (IREQ).

### **Acknowledgment**

The authors would like to thank Mr. Steve Valois, Chief Expert, IREQ, Canada, for providing access and assistance for performing the testing program at IREQ facilities. The technical assistance by Mathieu Soares and Maxime were greatly appreciated. The detailed review and comments by Dr. Nicholas Carino, Concrete Technology Consultant in Cleveland, Ohio, United States, is gratefully acknowledged. Funding for this research was provided by the McGill Engineering Doctoral Award and NSERC Discovery Grants.

### **References**

- ABAQUS (2017). "ABAQUS Documentation." Dassault Systèmes, Providence, RI, USA.
- ACI (American Concrete Institute). 2013. *Report on Nondestructive Test Methods for Evaluation of Concrete in Structure*. ACI 228.2R. Farmington Hills MI: ACI."
- Aldo, O., Samokrutov, A. A., and Samokrutov, P. A. (2013). "Assessment of concrete structures using the Mira and Eyecon ultrasonic shear wave devices and the SAFT-C image reconstruction technique." *Construction and Building Materials*, 38, 1276-1291.
- Asadi, P., Gindy, M., and Alvarez, M. (2019). "A machine learning based approach for automatic rebar detection and quantification of deterioration in concrete bridge deck ground penetrating radar B-scan images." *KSCE Journal of Civil Engineering*, 23(6), 2618-2627.

- ASTM-C1383-15 (2015). "Standard Test Method for Measuring the P-Wave Speed and the Thickness of Concrete Plates Using the Impact-Echo Method." ASTM International, West Conshohocken, PA, 2015, [www.astm.org](http://www.astm.org).
- ASTM-C1740-16 (2016). "Standard practice for evaluating the condition of concrete plates using the impulse-response method." ASTM International, West Conshohocken, PA, 2016, [www.astm.org](http://www.astm.org).
- ASTM-D6432-11 (2011). "Standard Guide for Using the Surface Ground Penetrating Radar Method for Subsurface Investigation." ASTM International, West Conshohocken, PA, 2011, [www.astm.org](http://www.astm.org).
- Carino, N. J. (2013). "Training: Often the missing link in using NDT methods." *Construction and Building Materials*, 38, 1316-1329.
- Clausen, J. S., and Knudsen, A. "Nondestructive testing of bridge decks and tunnel linings using Impulse Response." *Proc., Proceedings of 10th ACI International Conference on Recent Advances in Concrete Technology, Seville, SP-261-19*, 263-275.
- Clausen, J. S., Zoidis, N., and Knudsen, A. (2012). "Onsite measurements of concrete structures using impact-echo and impulse response." *Emerging Technologies in Non-Destructive Testing V*, 117-122.
- Clem, D., Popovics, J., Schumacher, T., Oh, T., Ham, S., and Wu, D. "Understanding the impulse response method applied to concrete bridge decks." *Proc., AIP Conference Proceedings*, AIP, 1333-1340.
- Davis, A. (2004). "Rapid non-destructive test method at the Taiwan High-Speed Rail project." *Concrete Technology*, 30-35.
- Davis, A., and Hertlein, B. "Nondestructive testing of concrete pavement slabs and floors with the transient dynamic response method." *Proc., Proc Int Conf Struct Faults Repair (Lond)*, 429-433.
- Davis, A., Hertlein, B., Lim, M., and Michols, K. "Impact-Echo and Impulse Response stress wave methods: Advantages and limitations for the evaluation of highway pavement concrete overlays."
- Davis, A., and Petersen, C. "Nondestructive evaluation of prestressed concrete bridges using impulse response." *Proc., Proceedings, Inter. Symp. on Non-Destructive Testing in Civil Engineering (NDT-CE 2003)(Berlin)*.

- Davis, A. G. (2003). "The nondestructive impulse response test in North America: 1985–2001." *NDT & E International*, 36(4), 185-193.
- Davis, A. G., Dunn, C., and CEBTP (1974). "FROM THEORY TO FIELD EXPERIENCE WITH THE NON-DESTRUCTIVE VIBRATION TESTING OF PILES." *Proceedings of the Institution of Civil Engineers*, 57(4), 571-593.
- Davis, A. G., Evans, J. G., and Hertlein, B. H. (1997). "Nondestructive evaluation of concrete radioactive waste tanks." *Journal of performance of constructed facilities*, 11(4), 161-167.
- Davis, A. G., and Hertlein, B. "Assessment of Bridge Deck Repairs by a Nondestructive Technique." *Proc., NATO Advanced Research Workshop on Bridge Evaluation, Repair and Rehabilitation*, Kluwer Academic Publishers, 229-234.
- Davis, A. G., and Hertlein, B. H. "Nondestructive testing of concrete chimneys and other structures." *Proc., Nondestructive Evaluation of Aging Structures and Dams*, International Society for Optics and Photonics, 129-137.
- Davis, A. G., Hertlein, B. H., Lim, M. K., and Michols, K. (1996). *Impact-echo and impulse response stress-wave methods: advantages and limitations for the evaluation of highway pavement concrete overlays*, SPIE.
- Davis, A. G., Lim, M. K., and Petersen, C. G. (2005). "Rapid and economical evaluation of concrete tunnel linings with impulse response and impulse radar non-destructive methods." *NDT & E International*, 38(3), 181-186.
- Finno, R. J., and Gassman, S. L. (1998). "Impulse response evaluation of drilled shafts." *Journal of Geotechnical and Geoenvironmental Engineering*, 124(10), 965-975.
- Gorzelańczyk, T., Hoła, J., Sadowski, Ł., and Schabowicz, K. (2013). "Methodology of nondestructive identification of defective concrete zones in unilaterally accessible massive members." *Journal of Civil Engineering and Management*, 19(6), 775-786.
- Ham, S., and Popovics, J. (2015). "Application of micro-electro-mechanical sensors contactless NDT of concrete structures." *Sensors*, 15(4), 9078-9096.
- Higgs, J. (1979). "Integrity testing of concrete piles by shock method." *Concrete*, 13(10).
- Hola, J., Sadowski, L., and Schabowicz, K. (2009). "Non-Destructive Evaluation of the Concrete Floor Quality Using Impulse Response S'Mash And Impact-Echo Methods. e." *Journal of Nondestructive Testing*, 14(03).
- Idorn, G. (1991). "Concrete durability and resource economy." *Concrete International*, 13(7).

- Kang, M.-S., Kim, N., Lee, J. J., and An, Y.-K. (2019). "Deep learning-based automated underground cavity detection using three-dimensional ground penetrating radar." *Structural Health Monitoring*, 1475921719838081.
- Kee, S.-H., Oh, T., Popovics, J. S., Arndt, R. W., and Zhu, J. (2012). "Nondestructive bridge deck testing with air-coupled impact-echo and infrared thermography." *Journal of Bridge Engineering*, 17(6), 928-939.
- Limaye, H. S. "Impulse Response Technique: A Valuable Non-Destructive Method to Detect Flaws." *Proc., ASME 2013 Power Conference*, American Society of Mechanical Engineers, V002T013A001-V002T013A001.
- Martin, J., Broughton, K., Giannopolous, A., Hardy, M., and Forde, M. (2001). "Ultrasonic tomography of grouted duct post-tensioned reinforced concrete bridge beams." *Ndt & E International*, 34(2), 107-113.
- McCavitt, N., Yates, M., and Forde, M. (1992). "Dynamic stiffness analysis of concrete pavement slabs." *Journal of transportation engineering*, 118(4), 540-556.
- Michols, K., Davis, A., and Olson, C. (2001). "Evaluating historic concrete bridges." *Concrete Repair Bulletin*, 14(4), 5-8.
- Sajid, S., and Chouinard, L. (2019). "Impulse response test for condition assessment of concrete: A review." *Construction and Building Materials*, 211, 317-328.
- Sajid, S., Chouinard, L., and Carino, N. (2019). "Robustness of Resonant Frequency Test for Strength Estimation of Concrete." *Advances in Civil Engineering Materials*, 8(1), 451-462.
- Saldua, B. P., Dodge, E. C., Kolf, P. R., and Olson, C. A. (2018). "Reinforced concrete antenna pedestal." *Concrete International*, 40(4), 40-42.
- Sansalone, M., Carino, N. J., and Hsu, N. N. (1987). "A finite element study of transient wave propagation in plates." *Journal of research of the National Bureau of Standards*, 92(4), 267-278.
- Sarma, G., Mallick, K., and Gadhinglajkar, V. (1998). "Nonreflecting boundary condition in finite-element formulation for an elastic wave equation." *Geophysics*, 63(3), 1006-1016.
- Schulz, E., Speekenbrink, M., and Krause, A. (2018). "A tutorial on Gaussian process regression: Modelling, exploring, and exploiting functions." *Journal of Mathematical Psychology*, 85, 1-16.

- Sun, H., Pashoutani, S., and Zhu, J. (2018). "Nondestructive evaluation of concrete bridge decks with automated acoustic scanning system and ground penetrating radar." *Sensors*, 18(6), 1955.
- Tarussov, A., Vandry, M., and De La Haza, A. (2013). "Condition assessment of concrete structures using a new analysis method: Ground-penetrating radar computer-assisted visual interpretation." *Construction and Building Materials*, 38, 1246-1254.
- Zhu, J., and Popovics, J. S. (2007). "Imaging concrete structures using air-coupled impact-echo." *Journal of engineering mechanics*, 133(6), 628-640.
- Zoidis, N., Tatsis, E., Vlachopoulos, C., Gotzamanis, A., Clausen, J. S., Aggelis, D. G., and Matikas, T. E. (2013). "Inspection, evaluation and repair monitoring of cracked concrete floor using NDT methods." *Construction and Building Materials*, 48, 1302-1308.

## 4. Defect Detection with Impulse-Response Test and Statistical Pattern Recognition

### Abstract

Statistical and machine learning analysis of structural health monitoring data is a popular approach for efficient structural level defect detection. However, the application of these techniques to stress-wave methods such as impact-echo and impulse-response data for local level detection has been limited. In this research, statistical pattern recognition in conjunction with the impulse-response test is shown to provide an efficient means for the detection of defects in concrete plates. For this purpose, the frequency response function (FRF) derived from the impulse-response test following ASTM C1740 protocols at specific points on the test plate was used to define the feature space matrix. Analytical results demonstrate that the variability of the FRF increases in the presence of defects, which forms the physical basis for the proposed pattern recognition algorithm. First, Principal Component Analysis (PCA) is performed on the covariance of the feature space matrix to identify the dominant features of the FRFs and to determine the number of statistically significant factors or principal components. Factor scores are next used to identify locations on the plate that are associated most closely to each pattern. The generalized Extreme Value Studentized (ESD) test and box and whisker plots are applied to the factor score vector of all the test points to objectively identify test points with defects and rank these based on their severity. Two experimental specimens are used to demonstrate the applicability of the proposed detection algorithm. The first specimen, a partially reinforced clamped concrete plate, is used to demonstrate the relationship between the shapes and variability of the FRFs and the severity of defects (delaminations), the efficacy of the factor score as damage sensitive feature, and identification and the ranking of the severity of defects by using outlier statistical tests. The second specimen is used to demonstrate the efficiency of the procedure for detecting both void and honeycomb defects in a larger reinforced concrete plate on elastic supports. The proposed procedure is shown to provide similar levels of detectability as the highly refined yet time consuming ultrasonic shear-wave tomography test. While the impulse-response test has been in use for the condition assessment of concrete elements other than drilled shaft piles since 1980's, defect detection has been based primarily on empirical observations and correlations with limited features of the frequency

response function. The use of pattern recognition techniques to the full range of the frequency response function is proposed and shown to greatly improve the detection and characterization of defects.

## **Keywords**

Principal component analysis, impulse-response test, outlier detection, plate on elastic foundation, frequency response function, honeycomb.

## **4.1 Introduction**

The deterioration of the infrastructure has been and remains a focus of research since a large proportion of existing structures are reaching the end of their service life and resources needed to remediate the situation are limited. This trend may be worsening given that climate change appears to accelerate the rate of deterioration of structures. Accurate conditions assessments are required to properly prioritize and target repairs and replacements. The development of non-destructive test methods (NDT) have been very instrumental for this purpose and are increasingly relied upon in practice (ACI). Among stress-wave based test methods, the most common are the impact-echo (ASTM-C1383-15, 2015), the impulse-response (ASTM-C1740-16, 2016), the ultrasonic echo, and the ground penetrating radar (ASTM-D6432-11, 2011). The impact-echo test is based on the analysis of the propagation of P-waves and reflections due to changes in acoustic impedance, usually associated with the presence of defects. The impact-echo test is reliable; however, the test is time consuming, which limits its application to small segments of structural elements that have previously been identified as potentially deficient. More recently, air-coupled sensing technology has been introduced to replace contact sensors (Ham & Popovics, 2015; Zhu & Popovics, 2007), which reduces the time required to perform the test. However, the need to perform multiple impacts to select the proper frequency range for a given type of defect remains a time limiting factor. The ultrasonic-echo or ultrasonic shear-wave tomography is a technique that generates 3D tomograms using synthetic aperture focusing techniques (SAFT) (Aldo, Samokrutov, & Samokrutov, 2013). One of the most common use of this test is for the integrity assessment of pre-stressed tendon grouts (Martin, Broughton, Giannopolous, Hardy, & Forde, 2001). The main limitation of this test is the relatively long time required for the completion of the test. Ground penetrating radar uses the propagation and reflection of electromagnetic waves due to changes in dielectric properties to detect defects and reinforcing steel. However, the interpretation of measurement is complex and

is the subject of considerable research efforts using innovative data analysis procedures (H. Sun, Pashoutani, & Zhu, 2018; Tarussov, Vandry, & De La Haza, 2013), and machine learning algorithms (Asadi, Gindy, & Alvarez, 2019; Kang, Kim, Lee, & An, 2019). Because it is based on electrical properties, interference from steel reinforcement or other embedded metallic objects impairs the assessment of deficiencies below the reinforcement layer. The impulse-response test, on the other hand, is a low frequency, stress-wave propagation method, which is widely used in practice as a fast scanning method (A. G. Davis, 2003). This method was first used for pile integrity testing; however, many researchers have extended its application to the condition assessment of bridge decks and floor slabs (Clausen & Knudsen, 2009; AG Davis & Hertlein, 1987), concrete chimneys (A. G. Davis & Hertlein, 1995), highway pavements (Allen Davis, Hertlein, Lim, & Michols, 1996), concrete tunnel linings (A. G. Davis, Lim, & Petersen, 2005), radioactive waste tanks (A. G. Davis, Evans, & Hertlein, 1997), thick concrete walls (Gorzelańczyk, Hoła, Sadowski, & Schabowicz, 2013), and debonding in concrete overlays (Sadowski, 2018) . An exhaustive literature review of case studies using the impulse-response test is given in (Sajid & Chouinard, 2019). The test procedure is briefly described below. More detailed descriptions can be found in ASTM C1740-16 (ASTM-C1740-16, 2016) and (A. G. Davis, 2003; Sajid & Chouinard, 2019).

The impulse-response test is performed by applying an impact to the surface of a concrete component with an instrumented rubber-tipped hammer that provides a usable frequency range of 0-1 kHz, and the response is recorded close to the impact location using a dry contact geophone. Typically, the test is performed by repeating the measurements over a grid of test locations across the surface of the concrete element. The velocity FRF or mobility is derived from the Fourier transforms of the geophone  $V(t)$  and hammer  $f(t)$  records.

$$mobility = \frac{V(F)}{f(F)} = \left| \frac{FFT(V(t))}{FFT(f(t))} \right| \quad (4-1)$$

Empirical indices (average mobility, dynamic stiffness, voids index, and mobility slope) derived from the FRF in the range of 10-800 Hz are calculated at each test location and changes in the indices on a relative basis are used as indicators for the presence of damage or defects (ASTM-C1383-15, 2015). These empirical indices describe various features of the FRF in the frequency range (10-800 Hz) and field experience is used to interpret their significance for the detection of various types of defects (Sajid & Chouinard, 2019).

The objective of this research is to provide a physical basis for anomaly detection with the FRF and to use unsupervised statistical pattern recognition as an objective criterion for defect detection. The proposed procedure is shown to be effective in both detecting the presence of defects as well as their degree of severity and does not require prior baseline surveys. The efficiency of the proposed algorithm for defect detection is shown to outperform damage detection criteria based on current empirical mobility spectrum indices and to provide results comparable to that using ultrasonic shear-wave tomography. The current state-of-the-art on statistical methods for defect detection and localization are first reviewed, followed by a derivation of analytical solutions to evaluate effect of defects on the FRF of a test point on the plate. Next, a statistical pattern recognition procedure using principal component analysis using the covariance of FRF feature space is proposed. The location of defects associated with each statistically significant pattern is determined by identifying outliers using box and whisker plots and statistical tests on scores of the FRFs for a grid of locations across the surface of the concrete plate. Finally, the proposed procedure is demonstrated through experiments performed on two plates and then validated using the ultrasonic shear-wave tomography.

## **4.2 Literature Review**

Statistical and machine learning methods have been used extensively over the last two decades to analyze vibration data for structural health monitoring purposes and component level damage detection of civil structures (Farrar & Worden, 2010; Haritos & Owen, 2004; Sohn, Farrar, Hemez, & Czarnecki, 2002). A general statistical pattern recognition paradigm defined in (Farrar, Duffey, Doebling, & Nix, 1999) for such applications include operational evaluation, data acquisition, feature selection, and statistical model development. Typically, damage is inferred through a comparison of statistical models fitted to monitored vibrations with models fitted to baseline surveys on the undamaged structure or component. Statistical models that have been proposed include among others, autoregressive models (Yao & Pakzad, 2012) and auto-regressive exogenous models (Mustapha et al., 2015; Sohn & Farrar, 2001). Damage detection is determined through changes in the model parameters or through outlier detection tests performed on the residuals of the baseline models such as the Mahalanobis distance-based outlier test (Jayawardhana, Zhu, Liyanapathirana, & Gunawardana, 2015; Morgantini, Betti, & Balsamo, 2021; Noman, Deeba, & Bagchi, 2013; Sohn, Farrar, Hunter, & Worden, 2001; Z. Sun & Chang,

2004). Multiple other damage sensitive features have been proposed for statistical pattern recognition such as wavelet packet signature (Z. Sun & Chang, 2004) and the time-frequency features using continuous wavelet transform (Qiao, Esmaily, & Melhem, 2012). Damage sensitive features together with Principal Component Analysis (PCA) is also widely used in structural health monitoring applications. Shahsavari et al. used PCA on discrete wavelet transform coefficients obtained for sensors along a beam to detect defects (Shahsavari, Chouinard, & Bastien, 2017). PCA has also been used for damage detection in steel plates using the Hotelling's  $T^2$ -statistic (Mujica, Rodellar, Fernandez, & Güemes, 2011). Artificial neural networks have also been used for the classification of damaged and undamaged states in structures but require large training data sets (Zang, Friswell, & Imregun, 2004).

The use of statistical pattern recognition for material deterioration using stress-wave tests, such as impact-echo, GPR and impulse-response, has also gaining attention in recent years. Dinh et al. (Dinh, Zayed, Romero, & Tarussov, 2015) use time series data from GPR scans to compare the similarity between a baseline scan and subsequent scans using the correlation coefficient. Ye (Ye et al., 2014) performs defect detection using the Grassmann-Manifold technique for pattern analysis on the temporal-spectral features of the data. Statistical analyses performed on the impulse-response test data are reviewed in (Sajid & Chouinard, 2019). Among others, Dodge and Chapa (Dodge & Chapa) and Saldua et al. (Saldua, Dodge, Kolf, & Olson, 2018) use the probability distribution of the average mobility, which is defined as the average mobility between the range from 100 to 800 Hz of the velocity FRF (ASTM-C1740-16, 2016). They propose that a defect is present at a location when the average mobility deviates beyond two standard deviations from the mean of the entire plate. However, the reliability of this approach has not been quantified and the average mobility is an empirical measure devoid of explicit underlying physical basis. In the present research, statistical pattern recognition procedures with physically based features vector are used to enhance the detectability of deterioration or other defects in concrete plates.

### **4.3 Relation between Material Defects and the FRF**

While most defect detection procedures using statistical methods are empirical based, detection on the basis of features that have a physical interpretation are preferable (Yao & Pakzad, 2012). In this section, the relationship between the high variability in the FRF and the presence of defects is

demonstrated using analytical formulation. Considering the model of a plate with n-degrees of freedom and linear behavior, the equations of motion are:

$$M\ddot{y}(t) + C\dot{y}(t) + Ky(t) = F(t) \quad (4-2)$$

where M, C and K are the mass, damping and stiffness matrices, respectively,  $\ddot{y}(t)$ ,  $\dot{y}(t)$  and  $y(t)$  are vectors for the vertical acceleration, velocity, and displacement of the nodes and  $F(t)$  represents the impulse applied at the surface of the plate which is given in Eq. 4-3, but for the sake of simplicity a harmonic excitation is used in the solution of the governing equation of motion;

$$F(t) = F_{max} \sin\left(\frac{\pi t}{t_c}\right)$$

$$F = 0, \text{ for } t > t_c \quad (4-3)$$

The generalized undamped solution of Eq. 4-2 results in the mode shape matrix  $\psi$ .

$$(K - \omega_i M)\psi_i = 0 \quad (4-4)$$

where  $\omega_i$  is the  $i^{th}$  eigenvalue and  $\psi_i$  is the corresponding eigen vector. For a classically damped system, the ratio of the Fourier transform of the response and force time histories is defined as the receptance matrix:

$$\frac{Y(\omega)}{F(\omega)} = \psi[\omega^2 + \Gamma\omega + \Omega]^{-1}\psi^T \quad (4-5)$$

where  $\Gamma = \text{diag}(2\xi_i\omega_i)$ , and  $\xi_i$  and  $\omega_i$  are the damping ratio and natural frequency associated with the  $i^{th}$  mode, and  $\Omega = \text{diag}[\omega_i^2]$ . The receptance for any given point j on the plate is,

$$\frac{Y(\omega)}{F(\omega)} = \sum_{j=1}^N \frac{\psi_j^T \psi_j}{m_1(\omega_j^2 - \omega^2 + 2i\xi_j\omega\omega_j)} \quad (4-6)$$

The mobility and accelerance matrices are associated respectively with the velocity and acceleration responses and obtained using  $\frac{V(\omega)}{F(\omega)} = i\omega Y(\omega)$ , and  $\frac{A(\omega)}{F(\omega)} = i\omega^2 Y(\omega)$ .

$$\left| \frac{V(\omega)}{F(\omega)} \right| = \sum_{j=1}^N \left| \frac{\psi_j^T \psi_j i\omega}{m_1(\omega_j^2 - \omega^2 + 2i\xi_j\omega\omega_j)} \right| \quad (4-7)$$

$$\left| \frac{A(\omega)}{F(\omega)} \right| = \sum_{j=1}^N \left| \frac{\psi_j^T \psi_j (-\omega^2)}{m_1(\omega_j^2 - \omega^2 + 2i\xi_j\omega\omega_j)} \right| \quad (4-8)$$

From the preceding formulation, it can be observed that the FRF at a given location is a function of both the local stiffness and damping of the plate. At the location of a void or honeycombing, the local stiffness and damping of the plate is decreased, resulting in higher amplitudes and a shift of the FRF to lower frequencies which translates into higher variability in the respective FRF. Conversely, the FRF on a solid test point will generally remain flat in the frequency range generally used for the impulse-response test. Such observations are also reported by the current state-of-art. Ottosen et al. (Ottosen, Ristinmaa, & Davis, 2004) reported the shift of frequency and the reduction in damping due to the presence of defects based on the analytical formulation for the impulse-response test on Euler-Bernoulli concrete beam on elastic foundation. Clem et al. (Clem et al., 2013) use finite element method to model the impulse-response test on a plate with various levels of void defects and observe a characteristic shift of the peak of the frequency peaks in FRF. These effects form the physical basis of the proposed algorithm as well as the current detection procedure. The mobility spectrum indices recommended in current practice are limited to single features of the FRF and do not characterize the patterns and variability of the mobility spectra for different test points. On the other hand, modern pattern recognition methods have the capability to optimally capture the patterns in the FRFs to differentiate responses between intact and defective locations in a plate by using the full frequency range of FRFs.

#### **4.4 Pattern Recognition Algorithm**

The principal component analysis (PCA) is a data reduction technique used in a wide range of fields. PCA performs an eigenvalue/eigenvector analysis of either the covariance or correlation matrix and ranks uncorrelated linear combinations of the original variables in order of decreasing order of percentage variance explained (Jolliffe & Cadima, 2016). The first few components are interpreted as dominant patterns that are generated through a physical process while lower ranked components are usually associated with noise in the data set. The selection of the optimal number of components to retain can be selected as the inflection point in the scree plot (% of variance explained as a function of the number of components retained), or through physical interpretations of the components (Abdi & Williams, 2010; Shlens, 2014).

In this application, SVD is used to perform PCA on the covariance matrix. The basis of SVD is that any set of vectors in a multidirectional array can be expressed in terms of their projections on a set of axes, which meet the criteria of orthogonality and maximise the percent variance explained.

Consider a set of FRFs from impulse-response test measurements of  $m$  test points and  $n$  frequencies arranged in a matrix  $A$  of  $m$  rows and  $n$  columns,

$$[A] = \begin{bmatrix} A_{1,1} & \cdots & A_{1,n} \\ \vdots & \ddots & \vdots \\ A_{m,1} & \cdots & A_{m,n} \end{bmatrix} \quad (4-9)$$

The element  $A_{ij}$  represents the mean centered FRF value of the  $j^{th}$  frequency for  $i^{th}$  test point on a plate. The orthogonal set of vectors are obtained by diagonalizing the covariance matrix of  $A$ .

$$Cov(A) = AA^T \quad (4-10)$$

$$[A] = [U][\Sigma][V]^T \quad (4-11)$$

$$[A][A]^T = ([U][\Sigma][V]^T)([V][\Sigma][U]^T) \quad (4-12)$$

$$[A][A]^T = ([U][\Sigma]^2[V]^T) \quad (4-13)$$

where  $[U]$  is an orthogonal  $m \times m$  matrix,  $[\Sigma]$  is an  $m \times n$  rectangular diagonal matrix, and  $[V]^T$  is an orthogonal  $n \times n$  matrix. The diagonal entries of  $[\Sigma]^2$  denote the set of  $q$  positive eigenvalues of  $AA^T$  as  $(\lambda_1, \lambda_2, \dots, \lambda_q)$  and  $[U] = (u_1, u_2, \dots, u_q)$  denotes a set of corresponding eigenvectors.

The scree plot of the ranked percentage of variance explained by each component is used as an objective criterion for selecting the number of statistically significant components (Cattell, 1966).

The factor score of the  $i^{th}$  test point for the  $\beta^{th}$  factor is obtained as,

$$FS_{i\beta} = \sum_{k=1}^m \frac{u_{\beta n}}{\sqrt{\lambda_\beta}} A_{ij}^T \quad (4-14)$$

The number  $f n_\beta$  corresponds to the number of significant components obtained with the scree test beyond which there is no significant variation in the percent variance explained by the components. In the absence of clear inflection point on the scree plot, the test plate may be largely deemed as free of anomalies.

Principal components are expected to correspond to the dominant patterns of FRFs associated with defects in the plate. For locations of the plate without defects, the factor scores are expected to remain small in absolute terms and be similarly distributed, while at locations close to defects characterized by a principal component, they will be large and appear as outliers relative to other locations. A threshold on scores can be used to locate defects across the plate; however, if the

threshold is not selected properly, this can result in either failing to detect a defect or reporting a large number of false-positives. Thresholds can be specified on the basis of distance-based methods or hypothesis test to detect outliers (Abdi & Williams, 2010). Examples of commonly used distance-based and hypothesis testing methods are the Mahalanobis distance (Sohn et al., 2001; Yao & Pakzad, 2012), the Cosh spectral distance (Yao & Pakzad, 2012), the T-statistic, and Q-statistic (Keller, Cohen, Pakzad, & Pessiki, 2017; Mujica et al., 2011). For this application, box and whisker plots and extreme value based methods are favoured given their power and ability to identify multiple outliers in a data set. Commonly used extreme value tests are the Grubbs test (Grubbs, 1969; Stefansky, 1972), Tietjen-Moor test (Tietjen & Moore, 1972), and Generalized Extreme Studentized Deviate test (ESD) (Rosner, 1983). All these tests are parametric, which implies they assume that observations are normally or approximately normally distributed. The Grubbs test is used for the detection of a single outlier in a data set. The Tietjen-Moor test can be used to detect multiple outliers in a data set; however, its application requires that the exact number of outliers is known a priori, which is not the case in practice and introduces an element of subjectivity. The generalized ESD test is essentially the sequential application of the Grubb's test, and is used for the detection of multiple outliers in a data set. The advantage of the Generalized ESD over the Tietjen-Moore test is that the only the upper bound of the number of outliers has to be specified and it ranks the significance of each outlier up to the specified upper bound. Given an upper bound  $k$  for the number of outliers, the following test of hypothesis is formulated,

$H_0$ : *There are no outliers present in the set of scores*

$H_1$ : *There are up to  $k$  outliers present in the set of scores*

The test statistic for the score  $x_i$  at test location  $i$  and a given principal component is calculated as,

$$R_i = \frac{\max_i |x_i - \mu|}{s} \quad (4-15)$$

where  $\mu$  and  $s$  are respectively the mean and the standard deviation of factor scores for a given component and  $x_i$  is the score for test location  $i$  on a plate. The test is performed by removing the observation that maximizes the numerator in Eq. 4-15 and then repeating the operation with the remaining  $(n - 1)$  observations. Sampling with replacement is repeated  $k$  times such that  $k$  test statistics  $R_1, R_2, \dots, R_k$  are obtained, where  $k \leq m$ . Critical values corresponding to  $k$  test statistics for a significance level  $\alpha$  are calculated using Eq. 4-16.

$$\lambda_i = \frac{(n-i)t_{p,n-i-1}}{\sqrt{(n-i-1+t_{p,n-i-1}^2)(n-i+1)}} \quad \text{for } i = 1, 2, \dots, k \quad (4-16)$$

where  $t_{p,v}$  is the 100 $p$  percentage point from the t-distribution with  $v = (n - i - 1)$  degrees of freedom and  $p$  is calculated according to Eq. 4-17, in which  $\alpha$  is the significance level of the test.

$$p = 1 - \frac{\alpha}{2(n-i+1)} \quad (4-17)$$

The number of outliers is determined by finding the largest  $i$  such that  $R_i > \lambda_i$ , that is, the null hypothesis will be rejected if the test statistic value is greater than the critical value for a specific significance level.

The test points identified as extreme outliers in the box and whisker plot for the factor scores for each  $\beta_i$  ( $i = 1, 2, 3, \dots, k$ ) characterize the significant defects ranked in decreasing order of severity. Similarly, the test points shown as outliers using the ESD test on factor scores for  $\beta = 1$  identify the most significant defects in the test element ranked in decreasing order of severity. The process of the proposed algorithm from the impulse-response test measurements to the final defect detection, is outlined in the schematic presented in Figure 4-1.

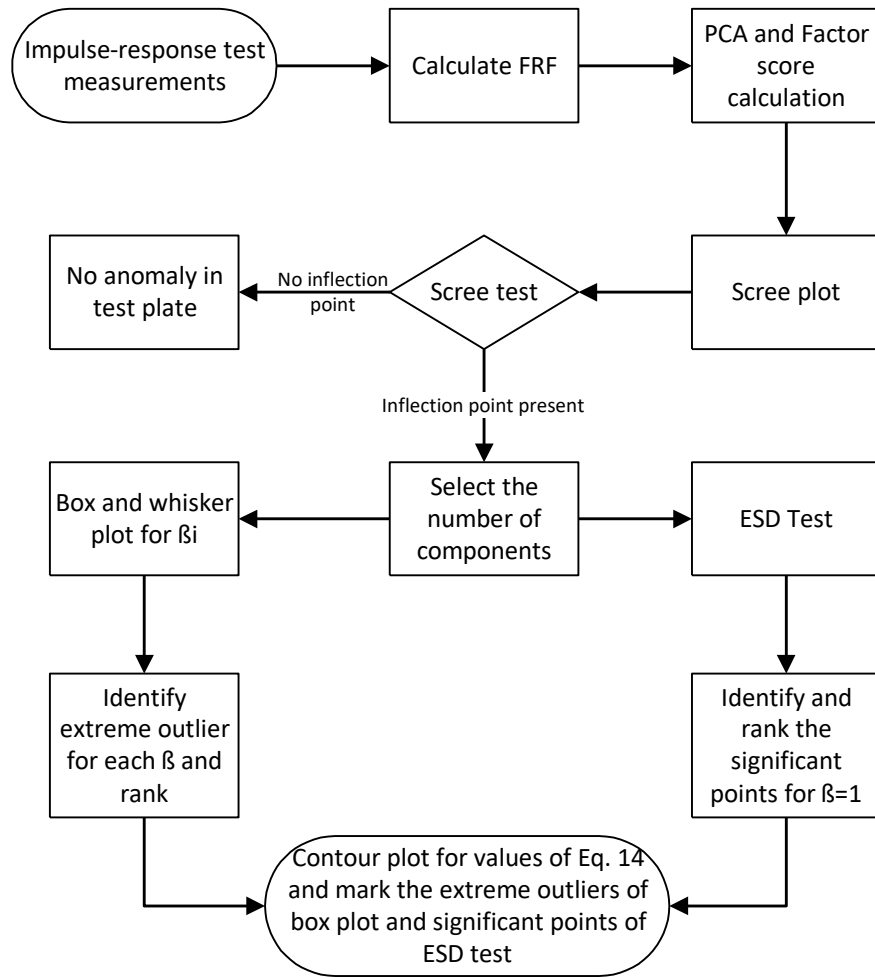


Figure 4-1. Schematic of defect detection with the impulse-response test using the proposed algorithm.

## 4.5 Experiments

Two experimental specimens are used to validate the proposed defect detection algorithm. The first specimen is used to validate the factor score as a damage sensitive feature in the presence of multiple void defects with varying geometrical characteristics. The second specimen is used to evaluate the accuracy of the proposed algorithm for a plate with two types of anomalies, a void and honeycombing, using a survey over a grid of test points.

### 4.5.1 Fully Supported Clamped Plate with Multiple Voids

The first experiment is performed on a 457 mm thick clamped concrete plate with several planar voids of different planar size and depth in zones with and without reinforcement (Figure 4-2 and Table 4-1).

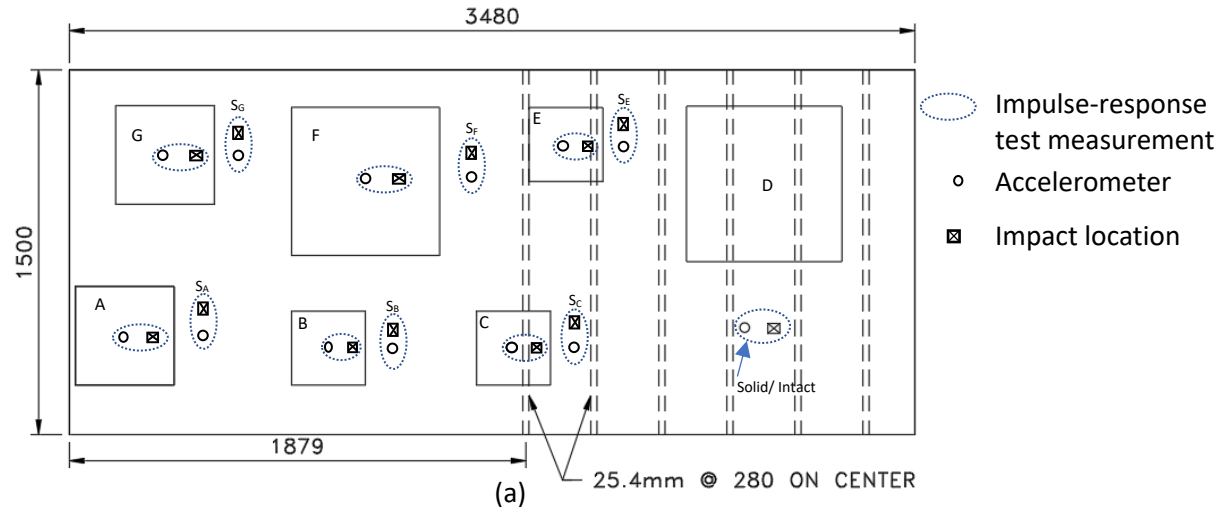


Figure 4-2. (a) Plan view of the first test plate with the impulse-response test measurements identified. All the dimensions are in the units of mm. (b) The specimen under construction. (c)

The specimen during impulse-response test

Table 4-1. Dimensions and depths of planar defects in the test plate.

Defect ID	Size (mm x mm)	Depth (mm)	Size/depth
A	457 x 457	305	1.5
B	305 x 305	152	2.0
C	305 x 305	38	8.0
D	760 x 760	76.2	10.0

Defect ID	Size (mm x mm)	Depth (mm)	Size/depth
E	305 x 305	114	2.7
F	610 x 610	203	3.0
G	406 x 406	76.2	5.3

The impulse-response test is performed using a piezoelectric accelerometer with a 100.616 mV/g, an instrumented hammer with an upper usable frequency range of 2200-4500 Hz, and a data acquisition system (LMS SCADAS Mobile) with a rate of up to 204 kHz per channel. To reduce noise and repeatability of measurements, epoxied steel plates were used for mounting the accelerometer on each test point. A sampling frequency of 20480 samples/sec was selected to obtain high resolution FRFs. The tests were performed on each defect, and an intact location as shown in Figure 4-2a. The locations of the impact and the receiver were within 100 mm of each other for all measurements. For tests performed at defect locations, the receiver was located at the surface above the approximate center of each defect. In-addition to the measurement at the intact location, tests were also performed at intact locations close to each defect. The Accelerance spectrum or acceleration FRF for each measurement is calculated using Eq. 4-18 and a range of 0-2000 Hz is used for the analysis.

$$Accelerance = \frac{A(F)}{f(F)} = \left| \frac{FFT(A(t))}{FFT(f(t))} \right| \quad (4-18)$$

A comparison between the FRFs at the intact location and for each defect is provided in Figure 4-3. A comparison is also provided between the FRF at the intact location and the FRF in the vicinity of each defect ( $S_A$ ,  $S_B$ ,  $S_C$ ,  $S_E$ ,  $S_F$ ,  $S_G$  in Figure 4-2a) for which the location of impactor and accelerometer at each measurement location are detailed in Figure 4-2a. This comparison indicates that distinct FRF patterns are associated with each defect in comparison to the FRF at the intact. Similar patterns are observed in the principal components (PCs) obtained using eigenvectors weighted by the corresponding eigenvalues according to the procedure outlined in section 4-4 (Figure 4-4)

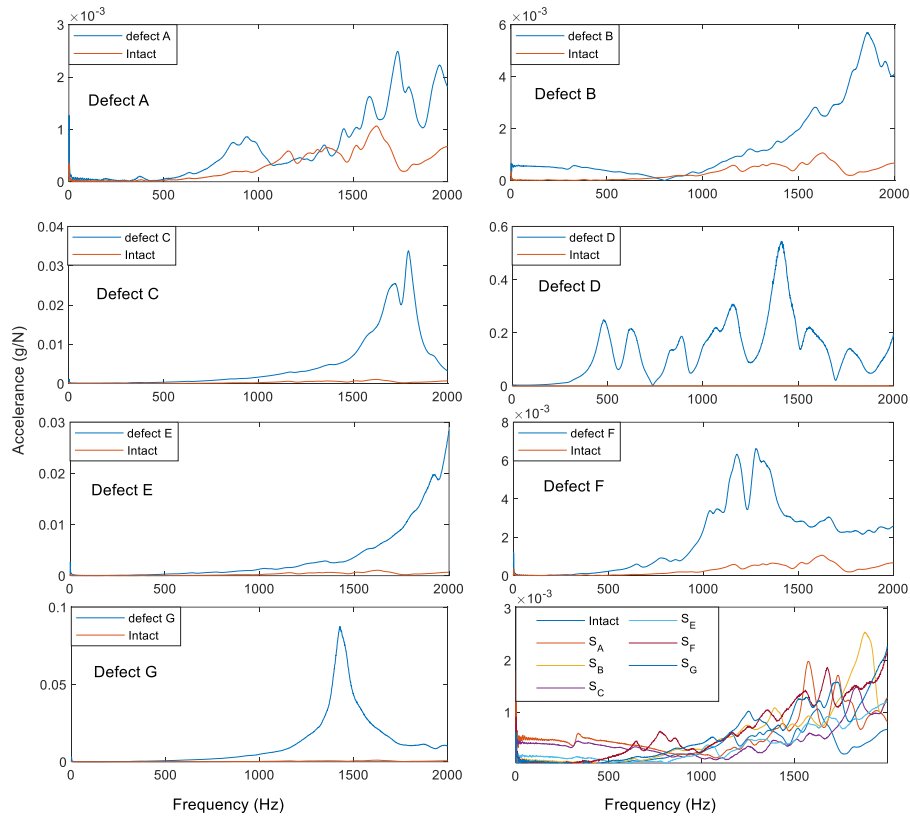


Figure 4-3. Comparison of accelerance spectra with intact and defect locations, and the intact locations near each defect identified in Figure 4.2a with each other.

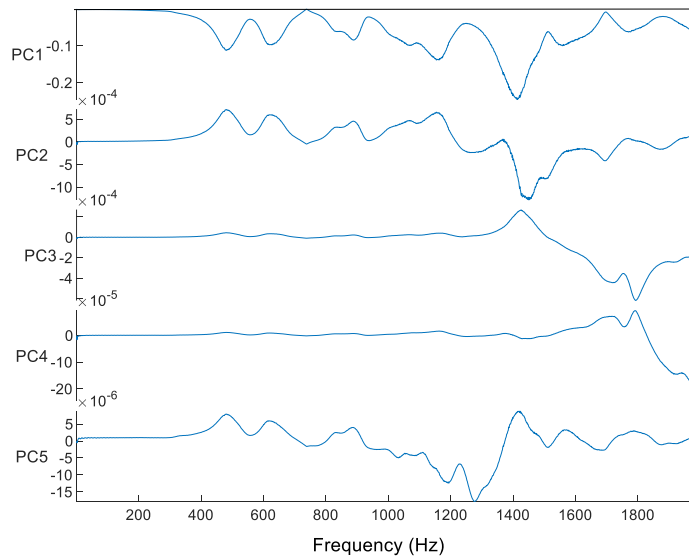


Figure 4-4. Pattern of the first 5 principal components for the FRF dataset of clamped concrete plate.

The number of components needed to fully capture the patterns to delineate defects are obtained using the objective criteria of the scree test. The scree plot and the percentage of variance explained for the first 10 components are shown in Figure 4-5. Almost all the variation in the dataset is explained by the first component, which makes it challenging to determine the exact number of the component on the scree plot beyond which the percent variance explained levels off. For this purpose, a second scree plot is obtained for component 2 to 10 using the data in the table in Figure 4-5. The scree test on both the scree plots shown in Figure 4-5a and Figure 4-5b show that the first five components explain most of the variance in the data set. The factor scores for each test point on the test plate are calculated according to Eq. 4-14 for the first 5 components and are shown in box and whisker plots in Figure 4-6.

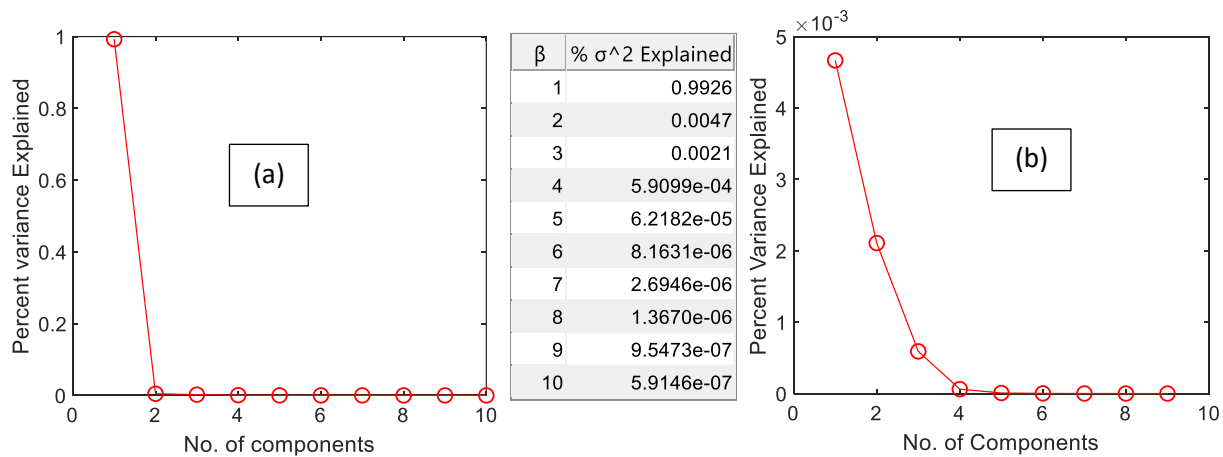


Figure 4-5. Scree plot and the percent variance explained by each component for the FRF dataset of clamped concrete plate.

The scores at locations with defects are significantly larger than for locations with no defect and are identified as either outliers or extreme outliers. It is also noted that the dominant defects are identified as outliers in decreasing order of severity in terms of area and distance from the surface (D, G, C, E, B, and F). Only defect A appears not be significant given its relatively large depth. The scores for component 4 correctly identify locations C, E, and B as defects. Interestingly, the three defects have the same surface area and their scores are inversely proportional to their depth from the surface. The ranking of defects from high to low severity based on the size to depth ratio is not perfect; however, because of the presence of reinforcement in the portion of the plate above defects C, D, and E. Nevertheless, using this procedure of defect severity ranking, D, C and E are

ranked for reinforced class and G and F for the un-reinforced class perfectly well. This confirms that such a ranking of test points with the factor scores as damage sensitive features is feasible. The ESD test is also performed to provide a statistical basis for defect detection and severity ranking. For this purpose, only the factor scores for the first component are used. The test statistic are calculated along with the critical values for various significance levels using the procedure outlined in section 4.4 and Eq. 4-15 to 4-17, as shown in Figure 4-7. In this case, the null hypothesis can be rejected for the presence of no more than 6 outliers at a significance level of 5%. The number of outliers does not change by increasing the significance levels of the test. The points for which the test statistic is higher than the critical values for a given significance level for factor score of  $\beta = 1$  belong to the test points with defects. Furthermore, they are ranked according to their severity in decreasing order based on the severity criterion of the size to depth ratio of the portion of plate above the defect for the reinforced and unreinforced portion of the plate. This ranking is similar to that of the box and whisker plot. Like the box and whisker plots, the ESD test shows all the test points with defects as outliers except for defect A. This is due to the larger depth to size ratio of the defect, which makes the FRF pattern nearly similar to that of a solid test point.

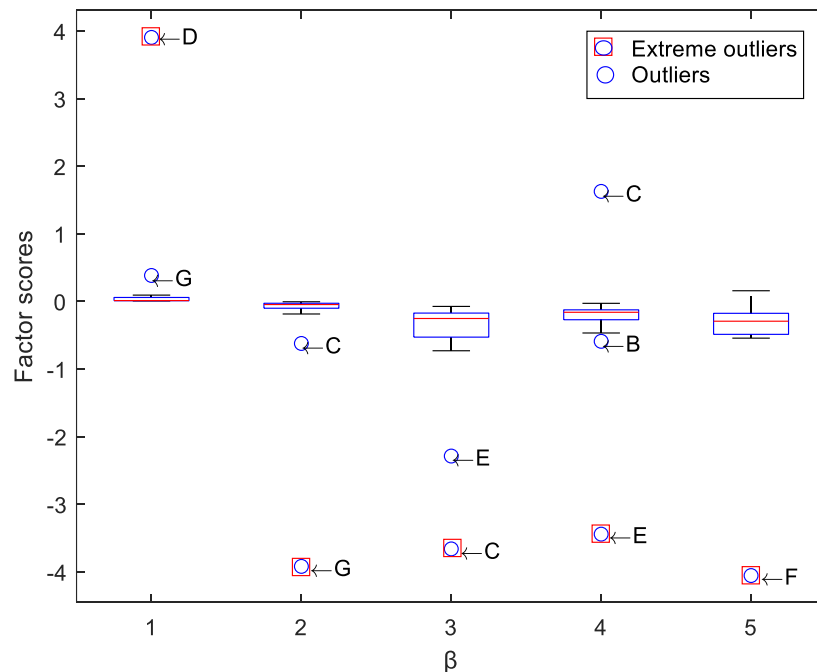


Figure 4-6. Box and Whisker plots of factor scores for the first 5 eigenvectors for the clamped concrete plate dataset.

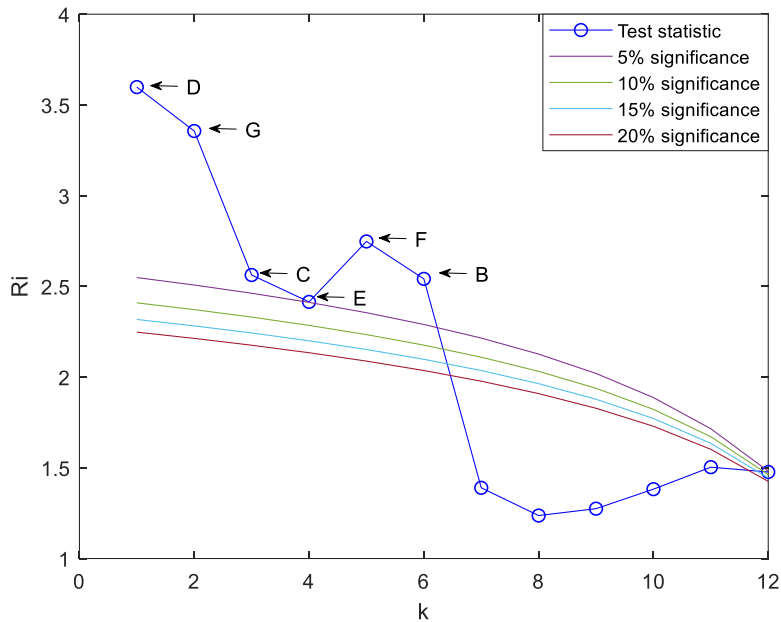


Figure 4-7. Outlier detection with ESD test on Factor scores for  $\beta = 1$ .

Having demonstrated the efficiency and validity of the factor scores as damage sensitive features, the influence of the geometrical characteristics on damage patterns, and the accuracy of the outlier detection in identifying and ranking the defects, the next experiment is performed on a larger specimen with different boundary conditions and two types of defects using a grid of test points to both locate and determine the spatial extent of the defects.

#### 4.5.2 Reinforced Concrete Plate on Elastic Foundation

In the second experiment, the impulse-response test is performed to detect defects in a reinforced concrete plate on elastic foundation. The plate is 400 mm thick and is reinforced with #4 bars in the upper portion of the slab only and in both lateral directions at 127 mm on center. The area of the test plate on which measurements were performed is 2.1 m by 2.7 m. The void and honeycomb defects are respectively at depths of 80 mm and 140 mm. The planar dimensions of the void and honeycomb are respectively 600 mm by 470 mm and 490 mm by 400 mm and their locations in the plate are shown in Figure 4-8.

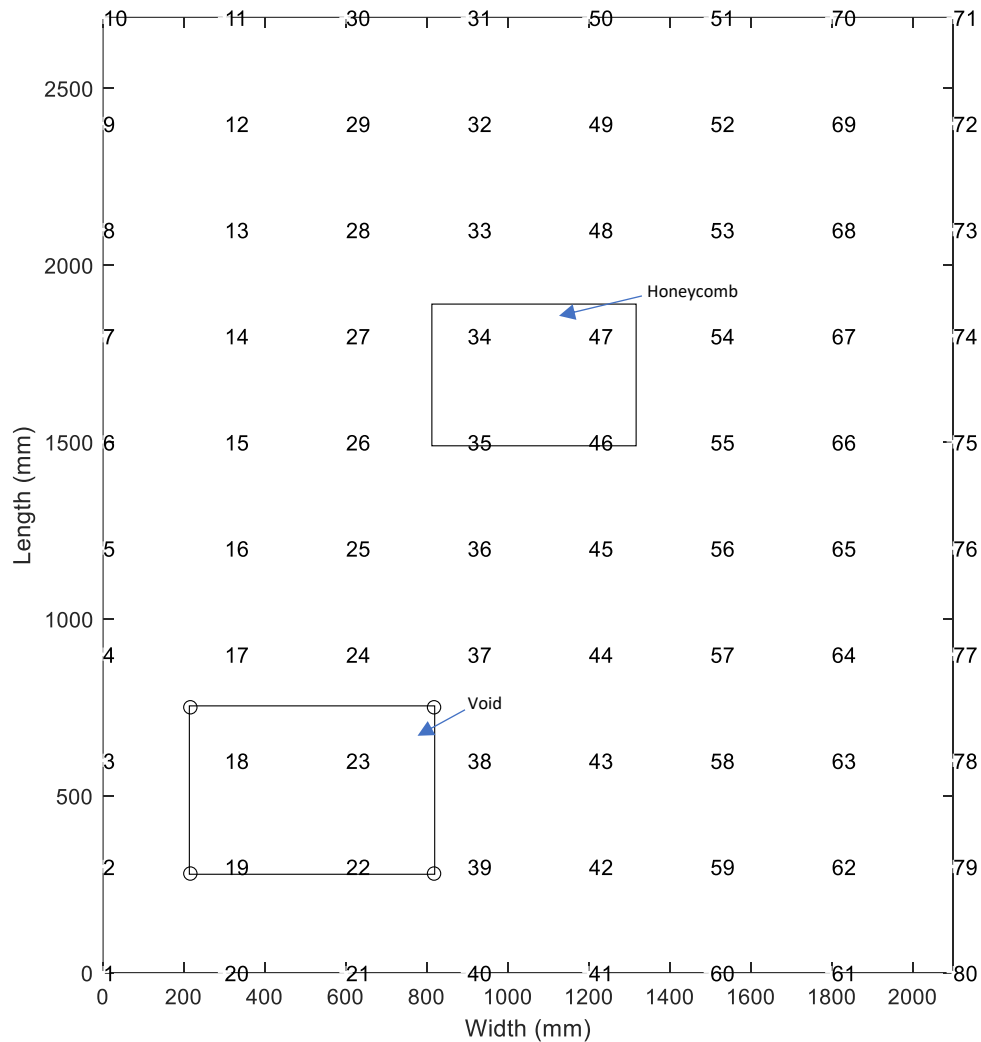


Figure 4-8. The test plate on elastic foundation with measurement grid and locations of void and honeycomb defects

The test is performed over a regular grid of 300 mm by 300 mm to scan the entire surface of the slab and emulate the measurement procedure followed in practice for a total of 80 test points. The designation of the measurements at each test point is shown in Figure 4-8. An instrumented hammer with a sensitivity of 0.23 mV/N, a geophone with a sensitivity of 20 mV/m/s, and a data acquisition system by National Instruments 5132-USB are used for the second experiment. The sampling frequency is 10 kHz. The hammer and geophone records are obtained at each test point on the test grid and the mobility is calculated according to Eq. 4-1. The FRFs from each test points

are compiled in a feature matrix for application of the defect detection algorithm outlined in section 4.4. Because of limitations on the usable frequency range associated with the stiffness and contact area of impactor tip (Sajid, Chouinard, & Carino, 2019), the frequency range from 0 – 700 Hz was used for the analysis.

The PCs and the percent variances explained by the first 10 components are presented respectively in Figure 4-9 and Figure 4-10. The patterns observed in the PCs corresponds to the dominant FRFs in the dataset. The first component explains 76% of the total variance and decreases rapidly for higher components. The percentage of variation explained by components beyond component 4 levels off and based on the scree plot, only the first 4 components are selected as significant. The factor scores for the first 4 components are shown in Figure 4-11.

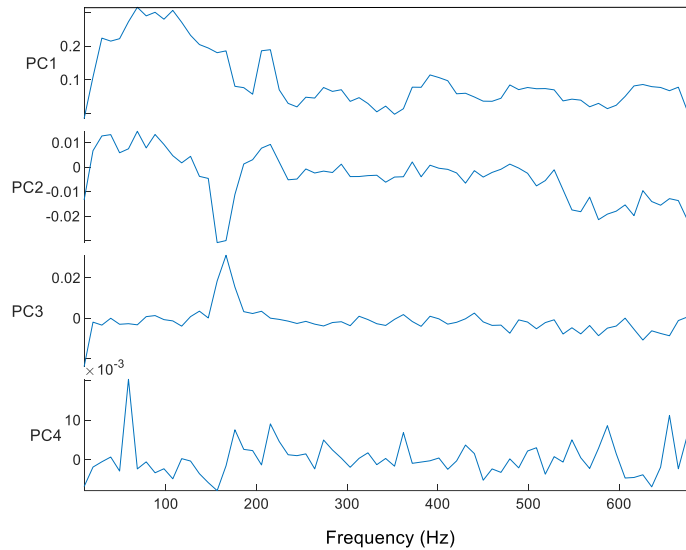


Figure 4-9. Patterns of the first 4 principal components of the dataset for the plate on elastic foundation.

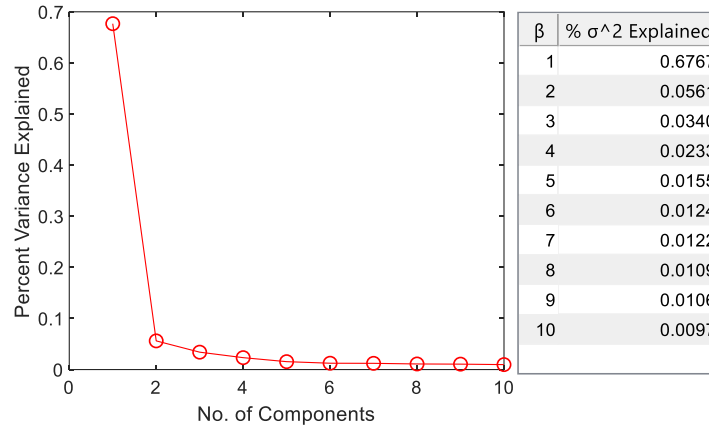


Figure 4-10. Scree plot and the percentage of variance explained by each component for the data set of the plate on elastic foundation.

The box and whisker plot is used to identify test points with defect as outliers for factor scores for the first four components. For the first component, test points 23, 18, 46, 19, and 22 are identified as defects in decreasing order of severity. These points are shown in Figure 4-8 to correspond to the locations of the void and the honeycomb. Similarly, the highest scores observed for the first four components are 23, 18, 34, 46 (Figure 4-11), where the first two are above the void and the last two are above the honeycomb. It is notable that some test points in the box plot for factor score of higher  $\beta$  values are also identified as outliers, though not relatively significant which implies the higher sensitivity of the box plot for slight imperfections in the material integrity and/or boundary condition.

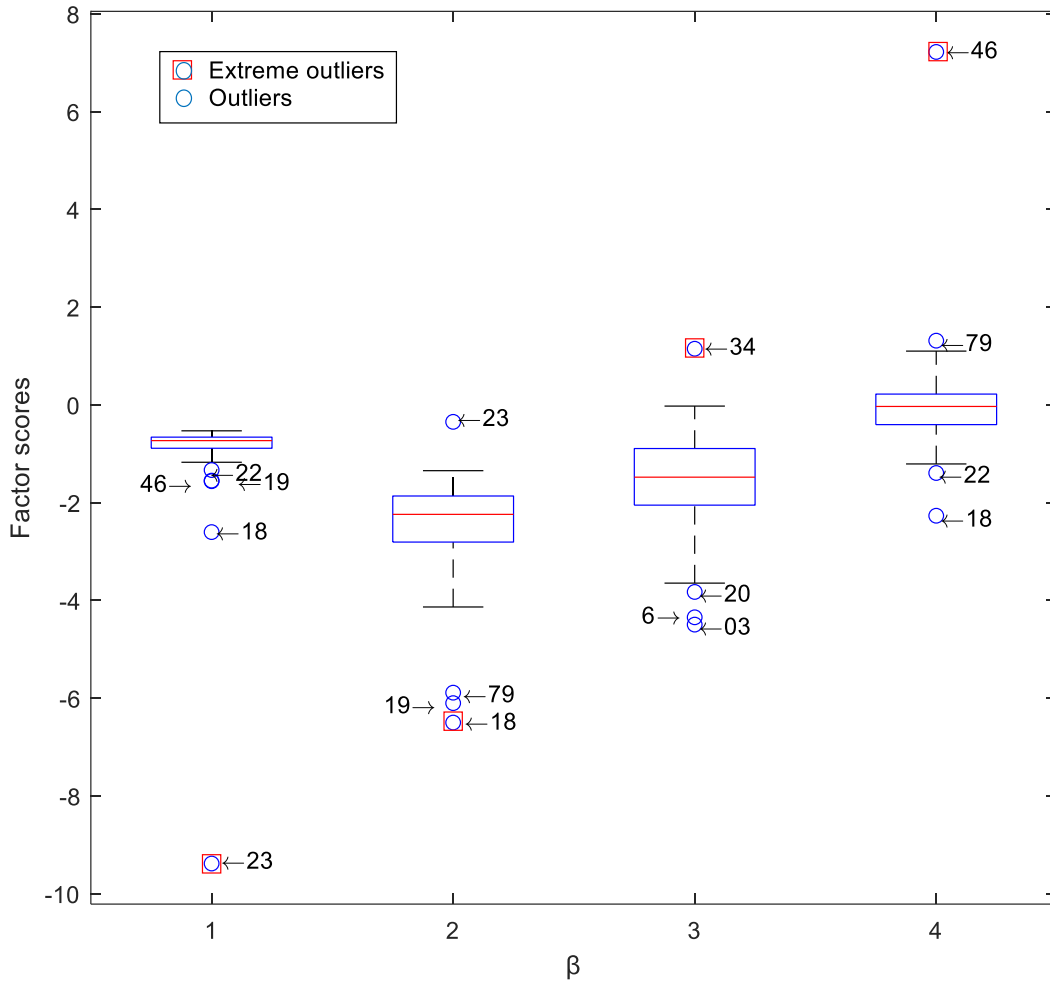


Figure 4-11. Box and whisker plots on factor scores for  $\beta = 1-4$ .

The outlier detection with the ESD test is performed by calculating the test statistic and critical values for various significance levels using Eq. 4-15 to 4-17 on the scores of the first component. The ESD test is relatively less sensitive compared to the box plot and only detect significant outliers in factor scores for high  $\beta$  values leaving the less severe defects as un-detected. The test statistic is greater than critical values for 5 test points at a significance level of 5%. These points are 23, 18, 19, 46, and 22, all of which correspond to the void except for point 46, which is associated with the honeycomb. This detection and ranking is similar to that of the box and whisker plot for factor score of  $\beta = 1$ . Furthermore, the number of test points for which the null hypothesis can be rejected did not change by increase the significance level of the statistical test (Figure 4-12).

The  $k$  value, which is the hypothesized number of outliers present in the factor score for  $\beta = 1$ , was set to 12. A higher value of  $k$  is computationally expensive and the outlier detection is not sensitive to  $k$  higher than the actual number of outliers present in the factor score vector. A contour plot for the factor scores for  $\beta = 1$  shows good agreement with the locations of the void and honeycomb defects (Figure 4-13). The extreme outliers from the box plots and also flagged as statistically significant with the ESD test are shown as red ellipsoids. Both the voids and the honeycomb are located and delineated with reasonable accuracy using the proposed defect detection procedure with the relatively low frequency range of the FRFs.

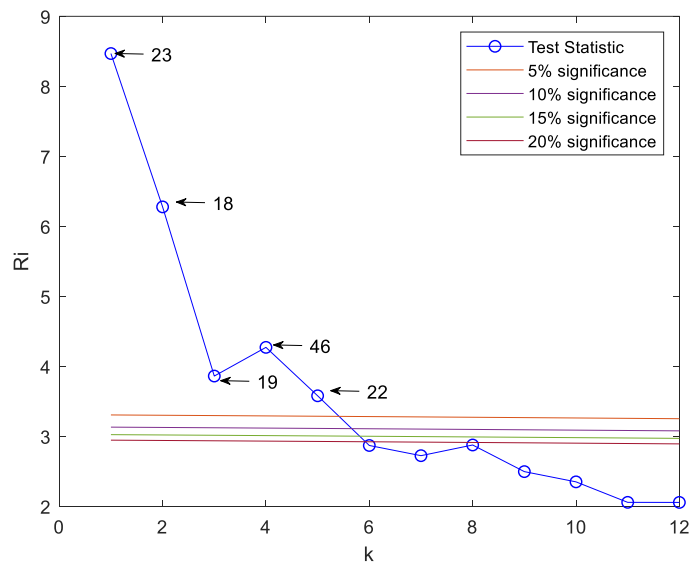


Figure 4-12. Outlier detection with ESD test on the factor scores for the first component for the plate on elastic foundation.

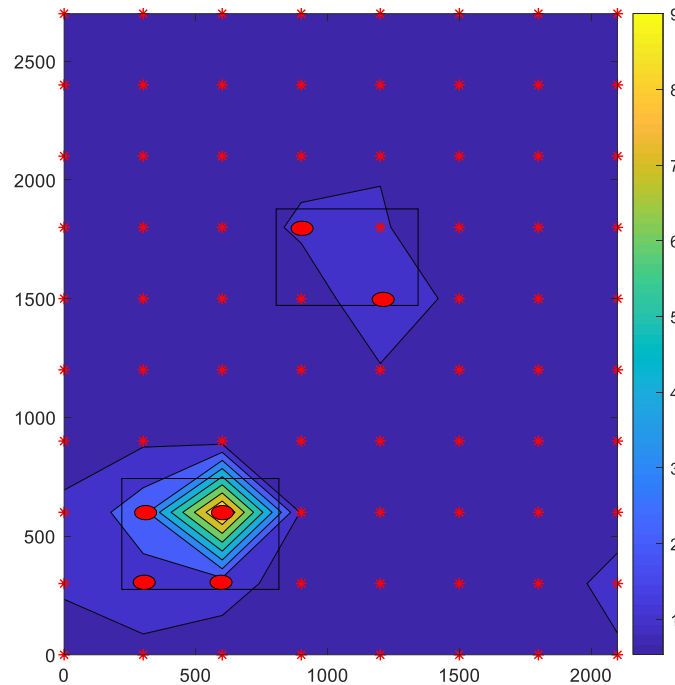


Figure 4-13. Contour plot of the factor score for the first component for the plate on elastic foundation with measurement locations and the outliers respectively by red asterisks and red ellipsoids.

#### 4.5.2.1 Comparison with the Current Detection Procedure

In current practice, empirical indices that describe different characteristics of the mobility FRF and displayed as contour plots across the plate are used for defect detection. Among these, the average mobility is the most common (Dodge & Chapa) (Saldua et al., 2018). The average mobility is defined as;

$$\text{Average mobility} = \frac{1}{n} \left[ \frac{|V(F)|}{|f(F)|} \right] \text{ for } 100 \text{ Hz} \leq F \leq 800 \text{ Hz} \quad (4-22)$$

where  $n$  is the number of ordinates of the mobility FRF in the range of 100 to 800 Hz,  $V(F)$  and  $f(F)$  are respectively the velocity and impact records in frequency domain, and  $F$  is the frequency range on the horizontal axis of the mobility FRF. The contour plot of the average mobility shows the presence of the void, but fails to detect the honeycomb (Figure 4-14). The current procedure only relies on a visual interpretation of the contour plot and does not comprise any statistical test to identify statistically significant defects. Often times, the contour plot is noisy and it is

challenging to subjectively determine the presence of defects thereby increasing the likelihood of false negatives. To explore the accuracy of the average mobility as damage sensitive feature and to assess if the addition of a statistical test for outlier detection would improve detectability of the impulse-response test, ESD test was used to detect outliers in the average mobility vector for all test points. For this purpose, a value of  $k=12$  was selected as the upper range of the possible number of test points with defects. The test statistic was calculated for significance levels ranging from 5 to 20%. It can be seen that only 4 outliers were detected namely 23, 18, 19 and 79 (Figure 4-15). None of these points belongs to the location of the honeycomb as shown in Figure 4-14. This demonstrates that the average mobility is not as optimal damage sensitive feature as the one in the proposed algorithm even when combined with statistical tests for the detection and delineation of defects.

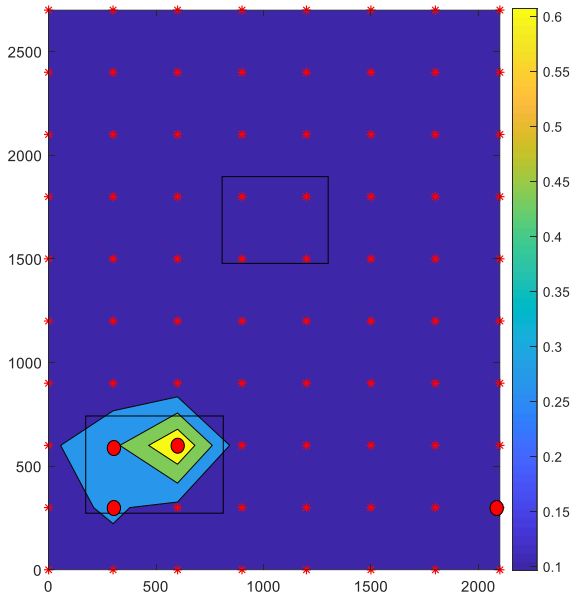


Figure 4-14. Contour plot of average mobility values for the plate on elastic foundation, with planned defects marked and measurement locations presented with red asterisks.

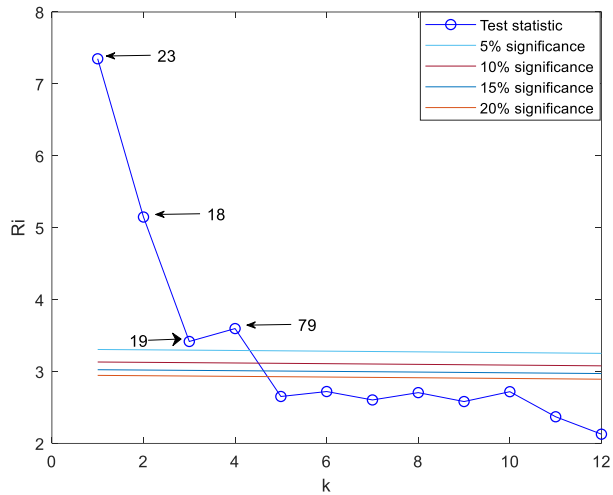


Figure 4-15. ESD test for outlier detection in the average mobility values at each test point for the plate on elastic foundation.

#### 4.5.2.2 Validation of the Proposed Algorithm

The proposed algorithm is designed for unsupervised applications without prior knowledge on the location and extent of defects. The validation of the proposed algorithm is performed by comparing the results of the impulse response test with observations from a high-resolution ultra-sonic shear wave tomography of the second plate (Figure 4-16). The tomography was performed over a grid of 150 mm by 75 mm using MiRA® (Germann-Instruments, 2014). The results show very good agreement between the two surveys. The anomalies identified correspond to the exact position of the void defect and the anomalies identified for the honeycomb correspond to the regions of high response of the C-scan. Lighter shaded areas in the tomography are not considered significant and can be attributed to edge effects and uneven compaction of the plate during casting of the specimen.

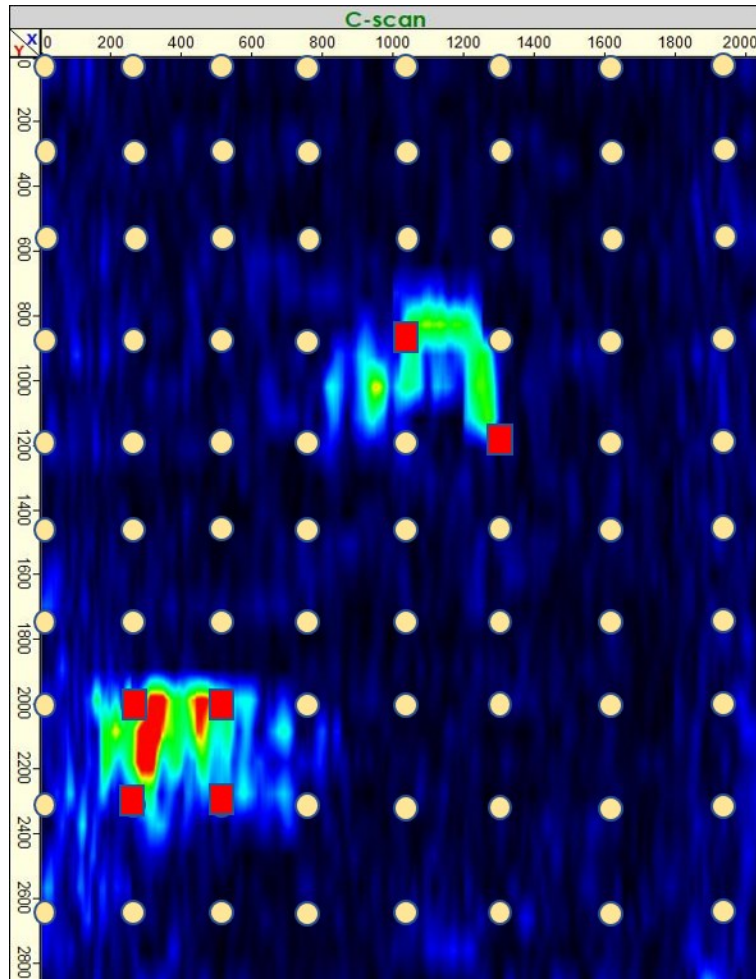


Figure 4-16. Tomogram (C-scan) of the plate obtained using ultrasonic shear wave tomography with MiRA®. The measurements of the impulse-response test are shown as yellow circles and the outliers detected with the box and whisker plots and the ESD are shown as red rectangles.

#### 4.6 Discussion and Future Research Prospects

The impulse-response test is one of the widely used NDT methods for the condition assessment of concrete. Nevertheless, the current data analysis procedures for defect detection may limit the performance of the test. Given the benefits of statistical pattern recognition methods in health monitoring applications, an algorithm based on principal component analysis performed on the FRFs matrix is proposed to improve the diagnostic value of the impulse-response test for defect detection and characterization. The proposed unsupervised algorithm does not require prior baseline surveys or a priori knowledge on the condition of the test element. Two experimental specimens are used for validating the proposed algorithm. The first specimen, which is a clamped

partially reinforced concrete plate having voids of different size and depth, is used to demonstrate the diagnostic value of factor scores for significant components identified from the scree plot and their relation with the severity of the defects. The second specimen, which is a reinforced concrete plate on elastic foundation having a void and honeycomb defect, is used to demonstrate the applicability of the proposed procedure when the impulse-response test measurements are performed in a grid format with two types of defect. The results demonstrate that the proposed algorithm can correctly locate and rank defects in decreasing order of severity and outperforms currently used damage indices such as the average mobility. The findings of this research are also significant from the perspective that the proposed algorithm demonstrates the relatively low frequency impulse-response test can perform at a level equivalent to that of the high frequency ultrasonic shear-wave tomography test but at a much lower cost. The sensitivity of the proposed data analysis procedure as a function of the frequency range of the FRF has to be further investigated, in particular by extending the usable range of the FRF with different types of hammers. The effect of the grid size for test points on the detectability of defects as a function of their type, spatial extent and depth, and plate boundary conditions also need further investigations.

#### **4.7 Conclusion**

The findings of this research significantly improve the detection capabilities of the impulse-response test, which is a low frequency, widely used fast scanning stress-wave NDT method to identify local anomalies in reinforced concrete elements. It has been used for the condition assessment of concrete elements since 1980's but this research is one of the most comprehensive studies using signal processing and pattern recognition to improve the detection and delineation of defects.

The novelty of this research is in the development and application of pattern recognition techniques to the FRF derived from impulse-response records obtained using ASTM C1740 protocols to improve the detection and delineation of defects in concrete plates. The FRF is used to define vector-valued features that have high variance in the presence of defects. Further analysis of the vector-valued features using principal component analysis (PCA) indicates that the dominant patterns are related to specific types of defects and that the scores corresponding to these patterns greatly improve the ability to delineate spatially the extent of the defects in comparison to the indices currently used in practice. In particular, the tests performed on the second plate show that

the proposed algorithm can detect a honeycomb defect, which is undetected with currently used indices. Finally, the Generalized ESD test and box and whisker plot are shown to provide an efficient and objective means to identify and rank statistically significant defects.

### **Acknowledgement**

The authors express profound gratitude to Mr. Steve Valois, Chief Expert, Institut de recherche d'Hydro-Québec, Varennes, Québec, Canada, for access to testing on the first specimen, and Mariana Lara, Vice President, Germann Instruments Inc. Evanston IL, USA, for access to the second experimental specimen and the use of testing equipment for the impulse-response test and ultrasonic shear-wave tomography.

### **Funding**

The authors acknowledge the Mobility Award from the Faculty of Engineering, McGill University for funding the experiments on the 2<sup>nd</sup> specimen, the McGill Engineering Doctoral Award, and NSERC Discovery Grants for providing the funding for the research.

### **Conflict of Interest**

The authors declare no conflict of Interest.

### **References**

- Abdi, H., & Williams, L. J. (2010). Principal component analysis. *Wiley interdisciplinary reviews: computational statistics*, 2(4), 433-459.
- ACI. (American Concrete Institute). 2013. *Report on Nondestructive Test Methods for Evaluation of Concrete in Structure*. ACI 228.2R. Farmington Hills MI: ACI. In.
- Aldo, O., Samokrutov, A. A., & Samokrutov, P. A. (2013). Assessment of concrete structures using the Mira and Eyecon ultrasonic shear wave devices and the SAFT-C image reconstruction technique. *Construction and Building Materials*, 38, 1276-1291.
- Asadi, P., Gindy, M., & Alvarez, M. (2019). A machine learning based approach for automatic rebar detection and quantification of deterioration in concrete bridge deck ground penetrating radar B-scan images. *KSCE Journal of Civil Engineering*, 23(6), 2618-2627.
- ASTM-C1383-15. (2015). *Standard Test Method for Measuring the P-Wave Speed and the Thickness of Concrete Plates Using the Impact-Echo Method*. Retrieved from ASTM International, West Conshohocken, PA, 2015, [www.astm.org](http://www.astm.org):

- ASTM-C1740-16. (2016). *Standard practice for evaluating the condition of concrete plates using the impulse-response method*. Retrieved from ASTM International, West Conshohocken, PA, 2016, [www.astm.org](http://www.astm.org):
- ASTM-D6432-11. (2011). *Standard Guide for Using the Surface Ground Penetrating Radar Method for Subsurface Investigation*. Retrieved from ASTM International, West Conshohocken, PA, 2011, [www.astm.org](http://www.astm.org):
- Cattell, R. B. (1966). The scree test for the number of factors. *Multivariate behavioral research*, 1(2), 245-276.
- Clausen, J. S., & Knudsen, A. (2009). *Nondestructive testing of bridge decks and tunnel linings using Impulse Response*. Paper presented at the Proceedings of 10th ACI International Conference on Recent Advances in Concrete Technology, Seville, SP-261-19.
- Clem, D., Popovics, J., Schumacher, T., Oh, T., Ham, S., & Wu, D. (2013). *Understanding the impulse response method applied to concrete bridge decks*. Paper presented at the AIP Conference Proceedings.
- Davis, A., & Hertlein, B. (1987). *Nondestructive testing of concrete pavement slabs and floors with the transient dynamic response method*. Paper presented at the Proc Int Conf Struct Faults Repair (Lond).
- Davis, A., Hertlein, B., Lim, M., & Michols, K. (1996). *Impact-Echo and Impulse Response stress wave methods: Advantages and limitations for the evaluation of highway pavement concrete overlays*.
- Davis, A. G. (2003). The nondestructive impulse response test in North America: 1985–2001. *NDT & E International*, 36(4), 185-193.
- Davis, A. G., Evans, J. G., & Hertlein, B. H. (1997). Nondestructive evaluation of concrete radioactive waste tanks. *Journal of performance of constructed facilities*, 11(4), 161-167.
- Davis, A. G., & Hertlein, B. H. (1995). *Nondestructive testing of concrete chimneys and other structures*. Paper presented at the Nondestructive Evaluation of Aging Structures and Dams.
- Davis, A. G., Lim, M. K., & Petersen, C. G. (2005). Rapid and economical evaluation of concrete tunnel linings with impulse response and impulse radar non-destructive methods. *NDT & E International*, 38(3), 181-186.

- Dinh, K., Zayed, T., Romero, F., & Tarussov, A. (2015). Method for analyzing time-series GPR data of concrete bridge decks. *Journal of Bridge Engineering*, 20(6), 04014086.
- Dodge, E. C., & Chapa, S. V. *Impulse response testing - analysis of relative test data*. Paper presented at the International Symposium on Non-Destructive Testing in Civil Engineering (NDT-CE) September 15-17, 2015, Berlin , Germany.
- Farrar, C. R., Duffey, T. A., Doebling, S. W., & Nix, D. A. (1999). A statistical pattern recognition paradigm for vibration-based structural health monitoring. *Structural Health Monitoring*, 2000, 764-773.
- Farrar, C. R., & Worden, K. (2010). An introduction to structural health monitoring. *New Trends in Vibration Based Structural Health Monitoring*, 1-17.
- Germann-Instruments. (2014). NDT Systems - Bridging NDT Theory and Practice. In (pp. 96-102).
- Gorzelańczyk, T., Hoła, J., Sadowski, Ł., & Schabowicz, K. (2013). Methodology of nondestructive identification of defective concrete zones in unilaterally accessible massive members. *Journal of Civil Engineering and Management*, 19(6), 775-786.
- Grubbs, F. E. (1969). Procedures for detecting outlying observations in samples. *Technometrics*, 11(1), 1-21.
- Ham, S., & Popovics, J. (2015). Application of micro-electro-mechanical sensors contactless NDT of concrete structures. *Sensors*, 15(4), 9078-9096.
- Haritos, N., & Owen, J. (2004). The use of vibration data for damage detection in bridges: a comparison of system identification and pattern recognition approaches. *Structural Health Monitoring*, 3(2), 141-163.
- Jayawardhana, M., Zhu, X., Liyanapathirana, R., & Gunawardana, U. (2015). Statistical damage sensitive feature for structural damage detection using AR model coefficients. *Advances in Structural Engineering*, 18(10), 1551-1562.
- Jolliffe, I. T., & Cadima, J. (2016). Principal component analysis: a review and recent developments. *Philosophical Transactions of the Royal Society A: Mathematical, Physical and Engineering Sciences*, 374(2065), 20150202.
- Kang, M.-S., Kim, N., Lee, J. J., & An, Y.-K. (2019). Deep learning-based automated underground cavity detection using three-dimensional ground penetrating radar. *Structural Health Monitoring*, 1475921719838081.

- Keller, W., Cohen, R., Pakzad, S., & Pessiki, S. (2017). *Rapid detection of fatigue cracking in steel anchor rods using the impulse response method*. Retrieved from [http://onlinepubs.trb.org/onlinepubs/IDEA/FinalReports/Highway/NCHRP175\\_Final\\_Report.pdf](http://onlinepubs.trb.org/onlinepubs/IDEA/FinalReports/Highway/NCHRP175_Final_Report.pdf)
- Martin, J., Broughton, K., Giannopolous, A., Hardy, M., & Forde, M. (2001). Ultrasonic tomography of grouted duct post-tensioned reinforced concrete bridge beams. *NDT & E International*, 34(2), 107-113.
- Morgantini, M., Betti, R., & Balsamo, L. (2021). Structural damage assessment through features in queffreny domain. *Mechanical Systems and Signal Processing*, 147, 107017.
- Mujica, L., Rodellar, J., Fernandez, A., & Güemes, A. (2011). Q-statistic and T2-statistic PCA-based measures for damage assessment in structures. *Structural Health Monitoring*, 10(5), 539-553.
- Mustapha, S., Hu, Y., Nguyen, K., Alamdari, M. M., Runcie, P., Dackermann, U., . . . Ye, L. (2015). Pattern recognition based on time series analysis using vibration data for structural health monitoring in civil structures. *Electronic Journal of Structural Engineering*.
- Noman, A. S., Deeba, F., & Bagchi, A. (2013). Health monitoring of structures using statistical pattern recognition techniques. *Journal of Performance of Constructed Facilities*, 27(5), 575-584.
- Ottosen, N. S., Ristinmaa, M., & Davis, A. G. (2004). Theoretical interpretation of impulse response tests of embedded concrete structures. *Journal of engineering mechanics*, 130(9), 1062-1071.
- Qiao, L., Esmaeily, A., & Melhem, H. G. (2012). Signal pattern recognition for damage diagnosis in structures. *Computer-Aided Civil and Infrastructure Engineering*, 27(9), 699-710.
- Rosner, B. (1983). Percentage points for a generalized ESD many-outlier procedure. *Technometrics*, 25(2), 165-172.
- Sadowski, L. (2018). Methodology of the assessment of the interlayer bond in concrete composites using NDT methods. *Journal of adhesion science and Technology*, 32(2), 139-157.
- Sajid, S., & Chouinard, L. (2019). Impulse response test for condition assessment of concrete: A review. *Construction and Building Materials*, 211, 317-328.
- Sajid, S., Chouinard, L., & Carino, N. (2019). Robustness of Resonant Frequency Test for Strength Estimation of Concrete. *Advances in Civil Engineering Materials*, 8(1), 451-462.

- Saldua, B. P., Dodge, E. C., Kolf, P. R., & Olson, C. A. (2018). Reinforced concrete antenna pedestal. *Concrete International*, 40(4), 40-42.
- Shahsavari, V., Chouinard, L., & Bastien, J. (2017). Wavelet-based analysis of mode shapes for statistical detection and localization of damage in beams using likelihood ratio test. *Engineering Structures*, 132, 494-507.
- Shlens, J. (2014). A tutorial on principal component analysis. *arXiv preprint arXiv:1404.1100*.
- Sohn, H., & Farrar, C. R. (2001). Damage diagnosis using time series analysis of vibration signals. *Smart materials and structures*, 10(3), 446.
- Sohn, H., Farrar, C. R., Hemez, F. M., & Czarnecki, J. J. (2002). *A Review of Structural Health Monitoring Literature 1996-2001*. Retrieved from
- Sohn, H., Farrar, C. R., Hunter, N. F., & Worden, K. (2001). Structural health monitoring using statistical pattern recognition techniques. *J. Dyn. Sys., Meas., Control*, 123(4), 706-711.
- Stefansky, W. (1972). Rejecting outliers in factorial designs. *Technometrics*, 14(2), 469-479.
- Sun, H., Pashoutani, S., & Zhu, J. (2018). Nondestructive evaluation of concrete bridge decks with automated acoustic scanning system and ground penetrating radar. *Sensors*, 18(6), 1955.
- Sun, Z., & Chang, C. (2004). Statistical wavelet-based method for structural health monitoring. *Journal of structural engineering*, 130(7), 1055-1062.
- Tarussov, A., Vandry, M., & De La Haza, A. (2013). Condition assessment of concrete structures using a new analysis method: Ground-penetrating radar computer-assisted visual interpretation. *Construction and Building Materials*, 38, 1246-1254.
- Tietjen, G. L., & Moore, R. H. (1972). Some Grubbs-type statistics for the detection of several outliers. *Technometrics*, 14(3), 583-597.
- Yao, R., & Pakzad, S. N. (2012). Autoregressive statistical pattern recognition algorithms for damage detection in civil structures. *Mechanical Systems and Signal Processing*, 31, 355-368.
- Ye, J., Iwata, M., Takumi, K., Murakawa, M., Tetsuya, H., Kubota, Y., . . . Mori, K. (2014). *Statistical impact-echo analysis based on grassmann manifold learning: Its preliminary results for concrete condition assessment*. Paper presented at the Proceedings of 7th European Workshop on Structural Health Monitoring, , Nantes, France, 8–11 July; pp. 1349–1356.

Zang, C., Friswell, M. I., & Imregun, M. (2004). Structural damage detection using independent component analysis. *Structural Health Monitoring*, 3(1), 69-83.

Zhu, J., & Popovics, J. S. (2007). Imaging concrete structures using air-coupled impact-echo. *Journal of engineering mechanics*, 133(6), 628-640.

## **5. Detection and Ranking of Damage in Concrete Plates Using Impulse-response Test with Affinity Propagation and Homoscedasticity**

### **Abstract**

This article presents a procedure based on the impulse-response test and the affinity propagation algorithm to detect delamination, honeycomb, and debonding in concrete slabs. Frequency response functions (FRFs) generated with the impulse-response test according to the protocols of ASTM C1740 on a grid pattern are combined to define a feature space matrix. The affinity propagation (AP) algorithm is used to cluster the FRFs in the feature space. Clusters are shown to correspond to either intact locations or defects and cluster membership can be used to locate defects in the plate. The effectiveness of the algorithm for damage delineation is dependant on the optimal number of exemplars and some objective-criteria to categorize each cluster according to the severity of defects. To achieve this objective, an upper bound for the number of exemplars is proposed for optimal defect detection and the variance of the FRF is proposed and validated as a criterion for ranking the severity of defects and for merging exemplars that exhibit similar levels of variability to address potential underfitting issues associated with the AP algorithm. The latter is achieved by checking the homoscedasticity of each pair of exemplars using Levene's test for the equality of variance. Two fully supported slabs with free edges and having different characteristics, and a slab on elastic foundation with restrained edges are used to validate the proposed procedure. The proposed procedure is shown to efficiently detect shallow delamination and debonding. The deep delamination and honeycomb in the experimental slabs are also delineated but to a lesser extent compared to the shallow delamination.

### **Keywords**

Debonding, impulse-response test, delamination, honeycombing, homoscedasticity, affinity propagation.

### **5.1 Introduction**

Construction defects and ageing-related deteriorations adversely affect the durability of materials and the projected service life of reinforced concrete structures, which account for the largest

proportion of the infrastructure. The ingress of invasive substances (mainly chlorides and carbon compounds) inside the concrete alters its electrochemical environment and react with the protective passivation film at the surface of the reinforcing steel thereby exposing it to corrosion. The expansion of corrosion products can induce in-plane cracking, or delamination, which is difficult to detect visually in its early stages. Initial construction and/or design flaws may also induce delamination, as for example, improper post-tensioning in curved concrete elements (Choi, Woods, Hrynyk, & Bayrak, 2020). Similarly, honeycombing due to improper placement and/or compaction can increase the permeability of concrete and promote the ingress of water and contaminants. The timely detection and assessment of these defects with simple, accurate and low-cost non-destructive tests (NDT) is desirable given that early interventions followed by remedial measures increases the service life and lowers overall maintenance and repair costs of the structures.

## **5.2 Condition Assessment Methods**

Condition assessment surveys are generally performed prior to rehabilitation, repair or replacement decisions on a structure. A list of the various methods used in condition assessment is outlined in the consensus committee report of the American Concrete Institute (ACI-Committee-228, 2013). The most versatile methods among these are the impact-echo (ASTM-C1383-15, 2015), the impulse-response (ASTM-C1740-16, 2016), the ground penetrating radar (ASTM-D6432-11, 2011), and the ultrasonic shear-wave tomography. The impact-echo method is based on the analysis of the propagation of P-waves across the thickness of an element and of the reflected waves due to changes in material impedance when waves travel across different types of materials or through defects. The test performs well; however, the time required to complete the test limits its application to small sections of structural elements that have been identified as potentially deficient by other methods. More recently, the air-coupled sensing technology has been introduced to replace contact sensors to reduce the amount of work required to perform the test (Ham & Popovics, 2015; Zhu & Popovics, 2007). However, the task of tuning the impact to generate responses within the desired frequency range is time-consuming and remains a challenge. Similarly, the ground penetrating radar is based on the propagation and reflection of electromagnetic waves in the presence of defects and reinforcing steel due to changes in dielectric properties. However, the interpretation of measurements is complex and is still the subject of

ongoing research using innovative data analysis procedures (Sun, Pashoutani, & Zhu, 2018; Tarussov, Vandry, & De La Haza, 2013) and machine learning algorithms (Asadi, Gindy, & Alvarez, 2019; Kang, Kim, Lee, & An, 2019). Because it is based on the electrical properties of materials, signals are dominated by interactions with the steel reinforcement and other embedded metallic objects, which impairs the assessment of defects located below the steel reinforcement. The ultrasonic shear-wave tomography is used to generate 3D tomograms of objects using a synthetic aperture focusing technique (SAFT) (Aldo, Samokrutov, & Samokrutov, 2013). The method is highly accurate and is routinely used to assess the integrity of pre-stress tendon grouts (Martin, Broughton, Giannopolous, Hardy, & Forde, 2001). The main limitation of this test is the relatively long time required to perform the test.

### 5.3 Impulse-response Test

The impulse-response test (ASTM-C1740-16, 2016), on the other hand, is a low strain and low frequency stress wave propagation-based NDT method, which is widely used in practice across large surfaces as a fast scanning method (A. G. Davis, 2003). This method was first used for pile integrity testing; however, since the late 1980's it has also been used for the condition assessment of bridge decks, floor slabs (AG Davis & Hertlein, 1987), concrete chimneys (A. G. Davis & Hertlein, 1995), highway pavements (Allen Davis, Hertlein, Lim, & Michols, 1996), concrete tunnel linings (A. G. Davis, Lim, & Petersen, 2005), radioactive waste tanks (A. G. Davis, Evans, & Hertlein, 1997), and nuclear containment buildings (Miller, 2010). Sajid and Chouinard provide a detailed literature review and current state-of-the-art report on the test (Sajid & Chouinard, 2019). The standard procedure for the test is described in ASTM C1740. Measurements are typically performed across grid points at the surface of a test element to obtain the velocity frequency response function (FRF) or mobility spectrum at each test point. Several indices are derived from the mobility spectrum that characterize the shape of the mobility spectrum in the frequency range of 10-800 Hz. The indices for average mobility ( $N_{av}$ ), dynamic stiffness ( $K_d$ ), voids index ( $v$ ), and mobility slope  $\left(\frac{M_p}{N_{av}}\right)$  are defined and illustrated in Figure 5-1. These indices are a function, to varying degrees, of the modulus of elasticity  $E$ , the mass density of the material  $\rho$ , the thickness of the test element  $t$ , the stiffness of the element at its boundary  $K_{boundary}$ , and the presence of internal defects ( $ID$ ) such as debonding of overlay ( $D$ ), and delamination ( $DL$ ).

$$N_{av} = f(E, t, \rho) \quad (5-1)$$

$$K_d = f(E, t, K_{boundary}, ID) \quad (5-2)$$

$$\frac{M_p}{N_{av}} = f(\rho) \quad (5-3)$$

$$v = f(K_{boundary}, D, DL) \quad (5-4)$$

The dynamic stiffness ( $K_d$ ) is the inverse of the slope of the mobility spectrum in the 20-100 Hz range (Eq. 5-2) and the mobility slope ( $\frac{M_p}{N_{av}}$ ) is defined for the range from 100 to 800 Hz (Eq. 5-3). A relative comparison of the spatial variation of these indices is used to identify potentially deficient regions on the test element, which can be investigated in more detail by using more refined methods such as impact-echo or ultrasonic shear-wave tomography (ASTM C1740-16).

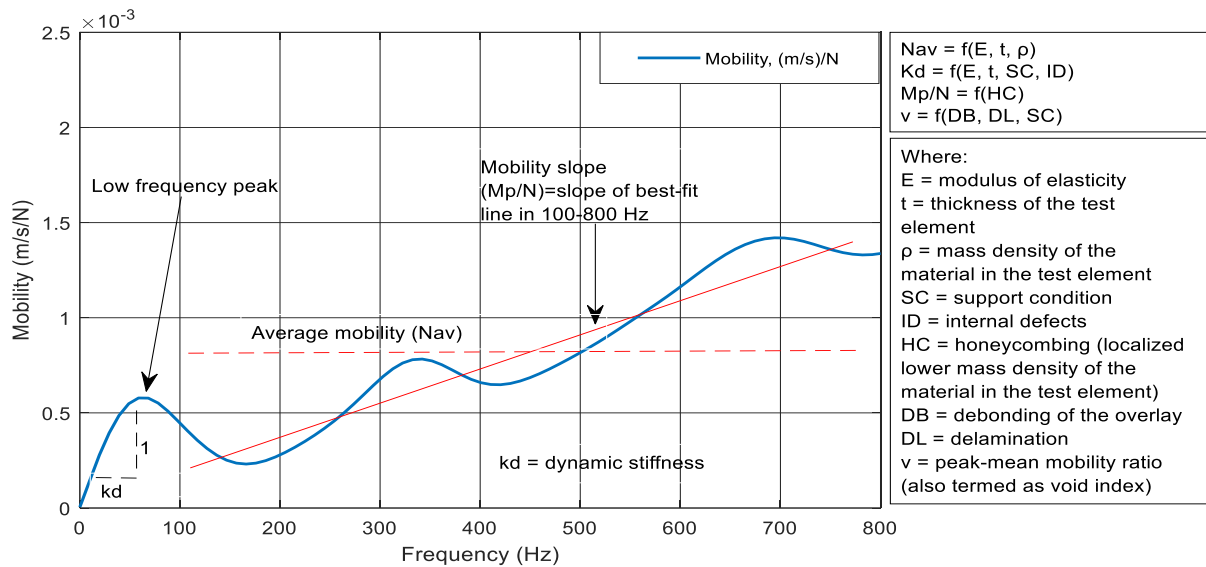


Figure 5-1. A typical mobility spectrum for concrete plate element with a description of the defect indices according to ASTM C1740-16.

Although the test has been used for the condition assessment of concrete elements since the late 1980's, there has been very limited research on the use of modern data analysis tools to improve diagnostics and provide physical insight linking features of the mobility spectrum and defects (Sajid & Chouinard, 2019). For example, Ottossen et al. (Ottossen, Ristinmaa, & Davis, 2004) use a theoretical model of a beam on elastic foundation to demonstrate that a defect either in the beam or the foundation will reduce damping and increase mobility. Nevertheless, the indices currently used in ASTM C1740-16 and their interpretation remain mostly empirically based. This research

is part of an effort to improve the diagnostics with the impulse-response test using novel data analysis procedures.

#### **5.4 Literature Review**

Clustering algorithms have been widely used for the detection of defects in concrete elements. Dinh et al. (Dinh et al., 2015) used k-means clustering for partitioning ground penetrating radar data for the assessment of the degree of corrosion in reinforced concrete bridge decks. Clustering has also been used to partition infrared thermography images for the assessment of defects in reinforced concrete bridge decks (Omar & Nehdi, 2017a, 2017b). Principal component analysis and self-organizing neural networks clustering have been used to analyse acoustic emission signals and assess the severity of damage in concrete elements (Calabrese, Campanella, & Proverbio, 2010). Clustering has also been used to combine information from different non-destructive procedures to detect and assess the severity of honey-combing in concrete elements (Völker & Shokouhi, 2015). Kabir et al. used edge detection algorithms and statistical pattern recognition with k-means clustering to classify defects in concrete dams (Kabir, Rivard, He, & Thivierge, 2009).

Clustering analysis has also been applied with the frequency response function and transmissibility data for defect detection. Yu et al. (Yu, Zhu, & Yu, 2013) use Fuzzy c-mean clustering to classify damaged and healthy states by clustering the medians of the principal components of the FRF obtained at different locations of a truss. Park et al. (Park, Lee, Yun, & Inman, 2008) assess the condition of bolted joints using electro-mechanical impedance monitoring. The data from wireless sensors is analyzed first by the principal component analysis followed by clustering using the k-means algorithm (Park et al., 2008). Lattanzi and Miller use image processing and clustering combined with a machine learning classifier for the detection of surface cracks on a bridge (Lattanzi & Miller, 2014). However, their methodology is based on supervised learning, which requires prior knowledge on a portion of the test element for training the model. Multiple other studies provide examples of clustering-based health monitoring for structural systems (Alamdari, Rakotoarivelo, & Khoa, 2017; Diez et al., 2016; Fang, Liu, & Teng, 2018; Hu et al., 2012; Yeung & Smith, 2005) (Alamdari, Rakotoarivelo, & Khoa, 2017; Diez et al., 2016; Fang, Liu, & Teng, 2018; Hu et al., 2012; Yeung & Smith, 2005). Zhou et al. (Zhou, Maia, Sampaio, & Wahab, 2017) use hierarchical clustering of the transmissibility measurements combined with a distance-based

similarity measure to detect damage in structures using laboratory scale models. Perera et al. (Perera, Torres, Ruiz, Barris, & Baena, 2019) demonstrate the detection of defects in surface layers of epoxy-bonded sheets to beam elements with two complementary clustering techniques. For this purpose, they use hierarchical clustering over the entire frequency range of the electromechanical impedance, and k-means clustering of moments of the measured impedance responses (Perera et al., 2019).

In the case of stress-wave testing methods, such as impact-echo and impulse-response, there are very few applications where clustering methods have been used to improve condition assessments of test elements. Zhang, Yan and Cui (Zhang, Yan, & Cui, 2016) apply a feed-forward neural network technique to data from the impact-echo Test. Igual et al. use a semi-supervised Bayesian classifier to analyse impact-echo data on aluminum alloy specimens to identify defects (Igual, Salazar, Safont, & Vergara, 2015). Hierarchical clustering has also been used with impact-echo data for similar purposes in laboratory investigations by Igual et la. (Igual, 2020). Sajid et al (Sajid, Taras, & Chouinard, 2021) use the factor score of principal components of the FRF from impulse-response tests as a damage indicator, which is shown to be a better damage sensitive feature for condition assessment compared to the currently used indices.

In this article, the AP algorithm is used to cluster and delineate defects in a plate using the FRFs at all the test points as a feature space matrix. This algorithm is favoured as it does not require to preselect the number of clusters initially. Nevertheless, the inputs to the algorithm can be adjusted to control the number of clusters. Some guidance is provided on the specification of the maximum number of cluster centers and the condition of homoscedasticity through the application of Levene's test is introduced to address underfitting by the AP algorithm. Finally, the variance of the resulting exemplars is shown to be very correlated with the severity of defects.

## **5.5 Frequency Response Function and Defects**

The frequency response function (FRF) obtained from the impulse response test and its interpretation are briefly reviewed for a plate. The shape of the FRF is characterized through a vector of values for a set of frequencies and forms the basis for defect detection and quantification of defect severity.

Consider a system with  $n$  degrees of freedom subjected to an input excitation  $f(t)$ , the governing equation of motion is:

$$M\ddot{x}(t) + C\dot{x}(t) + Kx(t) = f(t) \quad (5-5)$$

where  $M$ ,  $C$  and  $K$  are respectively ( $n \times n$ ) mass, stiffness, and damping matrices while  $\ddot{x}(t)$ ,  $\dot{x}(t)$ ,  $x(t)$ , and  $f(t)$  are respectively the column vectors of acceleration, velocity, displacement, and force in the system. Assuming that  $f(t)$  is a harmonic excitation, the Fourier transforms of the excitation and response are:

$$f(t) = F(\omega)e^{i\omega t} \text{ and } x(t) = X(\omega)e^{i\omega t} \quad (5-6)$$

Therefore, the solution of Eq. 5-5 in the frequency domain is,

$$(-\omega^2 M + i\omega C + K)X(\omega) = F(\omega) \quad (5-7)$$

The output response and input excitation are related through:

$$X(\omega) = H(\omega) \cdot F(\omega) \quad (5-8)$$

where  $H(\omega)$  is the FRF

$$H(\omega) = \frac{X(\omega)}{F(\omega)} = (-\omega^2 M + i\omega C + K)^{-1} \quad (5-9)$$

In the presence of a defect, the dynamic properties of the system are altered, which modifies the response of the system as:

$$X_d(\omega) = X(\omega) + \delta X(\omega) = H_d(\omega) \cdot F(\omega) \quad (5-10)$$

where  $\delta X(\omega)$  is the change in the system response due to presence of the defect, and  $H_d(\omega)$  is the FRF of the system with the defect. The effect of damage on the mass, damping and stiffness matrices are similarly defined as  $\delta M$ ,  $\delta C$ , and  $\delta K$ , such that:

$$H_d(\omega) = \frac{X_d(\omega)}{F(\omega)} = (-\omega^2(M - \delta M) + i\omega(C + \delta C) + (K + \delta K))^{-1} \quad (5-11)$$

Next, the input excitation is idealized as a cubic half sine wave function:

$$F(t) = F_{max} \sin^3\left(\frac{\pi t}{t_c}\right) \text{ for } 0 < t < t_c$$

$$F = 0, \quad \text{for } t > t_c \quad (5-12)$$

where  $t_c$  is the contact time of the impactor. This function satisfies the Dirichlet conditions (Ewins, 2009), and hence the Fourier transform for the impact is:

$$F(\omega) = \left(\frac{1}{2\pi}\right) \int_{-\infty}^{\infty} f(t)e^{-i\omega t} dt \quad (5-13)$$

The system response in the frequency domain due to the impact is:

$$X(\omega) = \underline{H}(\omega) \cdot F(\omega) \quad (5-14)$$

where  $\underline{H}(\omega)$  represents the FRF for the transient input and output functions and is similar to Eq. 5-8, which implies that the presence of a defect will modify the FRF in the same way as for a harmonic input-output system. Furthermore, the output in the input-output function can be in the form of displacement, velocity, and acceleration. A defect in the dynamic system is characterized with a local reduction in stiffness, mass, and damping. The reduction in the stiffness results in reducing the frequencies at which resonances occur in the system while reduction in damping increase the overall amplitude of the system responses. Both these contribute to relatively more fluctuations and higher amplitudes in the FRFs as compared with flatter FRFs for the same system without any defects. These changes in FRFs for the two systems results in higher variances in the FRFs at locations with defect in comparison with locations without defects. It follows that local variations in the dynamic characteristics of the element forms the basis for the detection and ranking of defects with the impulse-response test.

A finite element model is used to explain the influence of severity of delamination on the variance in the FRF. A concrete plate with 2m by 2m in plan and 500 mm thickness, fully restrained at the base is modeled in Abaqus®. The base material has a mass density of 2400 kg/m<sup>3</sup>, elastic modulus of 33 GPa, and Poisson's ratio of 0.2. The plate is modeled with delamination on its center in plan at different thicknesses and planar dimensions as shown in Figure 5-2. The delamination is modeled as open space inside the model of the plate given negligible elastic modulus of the polystyrene foam compared to concrete, which is generally used to simulate the delamination in the lab specimen (Zhu & Popovics, 2007). Impact was modeled using a half sine wave function with a useful frequency range of upto 3 Hz and the acceleration response recorded at 20 kHz sampling frequency on the center of the plate above delamination. The impact and response time

histories were used to generate FRFs in acceleration domain. The variance in each FRF vector in the frequency range of 0-2000 Hz is calculated and shown in Figure 5-2. It is evident that the severity of delamination characterized by smaller depth from the surface of the plate is directly influencing the variance in the respective FRFs.

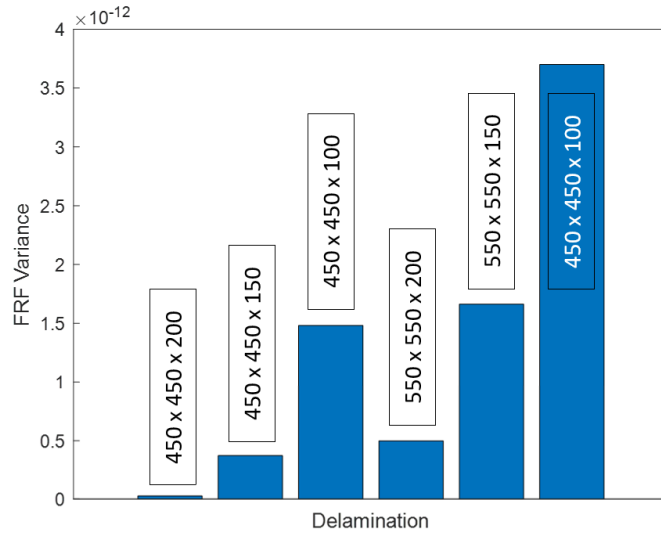


Figure 5-2. Influence of the defect severity on the variance of the FRF in the frequency range of 0-2000 Hz. All dimensions are in units of mm.

## 5.6 Proposed Procedure

### 5.6.1 Vectorization of the FRFs

The FRF is used to define a vector-valued feature for frequencies within a selected frequency range. The feature matrix  $[A]$  is formed of elements  $\{a_{ij}\}$  corresponding to the  $j^{th}$  FRF value at the specified frequency of the FRF for the  $i^{th}$  test location. The feature space matrix is then analyzed with a cluster identification algorithm to group FRFs with similar characteristics, which can be related either to intact locations of the element or specific types of defects.

### 5.6.2 Affinity Propagation (AP)

AP is a clustering algorithm based on the concept of “the message passing between feature vectors”, to find the “exemplars” (or cluster centers) (Frey & Dueck, 2007). For each FRF  $i$  and each candidate exemplar  $k$ , AP computes the "responsibility"  $\bar{r}(i, k)$ , which indicates how well suited  $k$  is an exemplar for  $i$ , and the "availability"  $\bar{a}(i, k)$  reflecting the evidence that  $i$  should choose  $k$  as an exemplar.

$$\bar{r}(i, k) \leftarrow s(i, k) - \max\{a(i, k') + s(i, k')\} \quad (5-15)$$

$$\bar{a}(i, k) \leftarrow \min\{0, \bar{r}(k, k) + \sum_{i': i' \notin \{i, k\}} \max\{0, \bar{r}(i', k)\}\} \quad (5-16)$$

where  $s(i, k)$  denotes the similarity between two nodes or mobility spectra, which is defined as the negative of the squared Euclidean distance between the FRF vector  $\sigma^{(i)}$  and  $\sigma^{(k)}$  (Eq. 5-17) (Frey & Dueck, 2007).

$$s(i, k) = -\left\|\sigma^{(i)} - \sigma^{(k)}\right\|^2 \quad (5-17)$$

The equations 5-19 to 5-21 are iterated until the cluster membership remains unchanged. Each test point  $i$  is then assigned to the exemplar  $k$ , which maximizes the sum  $\bar{a}(i, k) + \bar{r}(i, k)$ , and if  $i = k$ , then,  $\sigma^{(i)}$  is an exemplar (Vlasblom & Wodak, 2009).

The AP algorithm does not require that the number of clusters is specified a priori. The algorithm is initiated by scaling the diagonal of the similarity matrix or setting the  $s(i, i)$ , which Frey and Dueck (Frey & Dueck, 2007) refer to as “input preferences”. A high value on the diagonal of the similarity matrix will result in a high number of exemplars and vice versa. Frey and Dueck suggested to use the median of the off-diagonal terms of the similarity matrix as the input preference value to obtain an optimal number of exemplars. In this research, an alternative approach is proposed by setting the input preference value such that a high number of exemplars are obtained. An upper limit of 5 or 6 exemplars is suggested based on substantial experimentation. This recommended number of exemplars can be obtained by adjusting the input preferences value to the AP algorithm using a trial and adjustment procedure. To confirm if this number of exemplars results in underfitting by the AP algorithm, an additional constraint in the form of homogeneity of variances of each pair of exemplars is proposed. This homogeneity of variances or homoscedasticity is implemented using the Levene’s test as explained in the following section. The underfitting scenario can arise with the proposed upper number of exemplars for slabs with no defects or that have multiple defects of similar size and severity. The analyst can also select input preferences value to obtain higher numbers of exemplars and use the proposed homoscedasticity test to check for underfitting for the purpose of diagnostics, but it may be computationally expensive.

### 5.6.3 Homoscedasticity or Equality of Variance Test

As explained in section 5.5, the presence of a defect in a test element affects the local dynamic characteristics at a test point, which increases the variance of the corresponding FRF. Therefore, the variance of the FRF can be used as a criterion to distinguish between clusters corresponding to sections of the plate with or without defects as well as for ranking the degree of severity of the defects. The test is used primarily to eliminate clusters in intact regions that exhibit different FRF shapes but that are not statistically significant in terms of variability.

Various statistical tests can be used to test the equality of variance between two or several populations. The most common are the F-test, Bartlett's test (Snedecor & William, 1989), and Levene's test (Levene, 1960). In this research, Levene's test is used because it is the most robust to departures from normality.

The Levene's test for the equality of the variance of k clusters is defined as:

$$H_0: \sigma_1^2 = \sigma_2^2 = \dots = \sigma_k^2$$

$$H_a: \sigma_g^2 \neq \sigma_h^2 \text{ for at least one pair of } (g, h), \quad 2 \leq (g, h) \leq k$$

Given a sample of N observations distributed into k exemplars, where  $N_g$  is the sample size of the  $g^{th}$  exemplar (in this application,  $N_g$  is the same for all exemplars such that  $N = N_g$ ), the Levene's test statistic is defined as:

$$W = \frac{(N-k) \sum_{g=1}^k N_g (\bar{Z}_{g..} - \bar{Z}_{..})^2}{(k-1) \sum_{g=1}^k \sum_{h=1}^{N_g} (Z_{gh.} - \bar{Z}_{g.})^2} \quad (5-18)$$

$$Z_{gh} = |Y_{gh} - \bar{Y}_g| \quad (5-19)$$

where  $Y_{gh}$  is the value of the  $h^{th}$  accelerance component of the  $g^{th}$  exemplar,  $\bar{Y}_g$  is the average accelerance of the  $g^{th}$  exemplar,  $\bar{Z}_{g.}$  is the average of the absolute deviations of the accelerance components from the average accelerance for exemplar g and  $\bar{Z}_{..}$  is the overall mean of  $Z_{gh..}$ . The Levene's test rejects the null hypothesis (variances are equal) if,  $W > F_{\alpha, k-1, N-k}$ , where  $F_{\alpha, k-1, N-k}$  is the F-distribution with  $k - 1$  and  $N - k$  degrees of freedom at a significance level of  $\alpha$  (Sematech, 2006). In this article, the Levene's test is used to test all pairs of exemplars

obtained by the AP algorithm. If the test fails to reject the null hypothesis, the respective pair of exemplars are combined and their members are represented by either one of the two exemplars.

## **5.7 Experimental Study**

Three experimental specimens with different characteristics are used to validate the proposed procedure. The first two specimens, are reinforced concrete plates fully supported with unrestrained edges; one with defects and a reference slab. The slabs are respectively referred to as Slab 1 and Slab 2. The third specimen is a reinforced concrete plate on elastic foundation with restrained edges referred to as Slab 3. The following subsections describe each experimental specimen, the respective instrumentation, the measurements and the data analysis.

### *5.7.1 Fully Supported Slabs with Free Edges*

#### Description

Both Slab 1 and Slab 2 are 300 mm thick having planar dimensions of 2400 mm by 1200 mm. They are reinforced with 15M Grade 60 steel rebars in both directions at 150 mm spacings near the top and bottom surfaces of the slab. Defects simulating delamination (at two different depths), honeycomb, debonding, and pipes partially filled with grout are built in Slab 1 (Figure 5-3a). The delamination is simulated by using a 25 mm thick circular polystyrene foam sheet having a diameter of 300 mm. The shallow and deep delaminations are located at depths of 80 mm and 220 mm, respectively (Figure 5-3a). Debonding is simulated by placing a thin glass fiber sheet at a depth of 40 mm from the top surface. The honeycomb is simulated using a precast concrete block constructed using a small quantity of fine aggregates. The pipes simulate prestressing tendon ducts, one which is filled with a grout and the other is empty. Slab 2 is solid and is used as a reference (Figure 5-3b). The slabs are constructed with the MTQ type 5 concrete with a compressive strength of 35 MPa, which is typically used in pavements and bridge decks in Quebec, Canada.

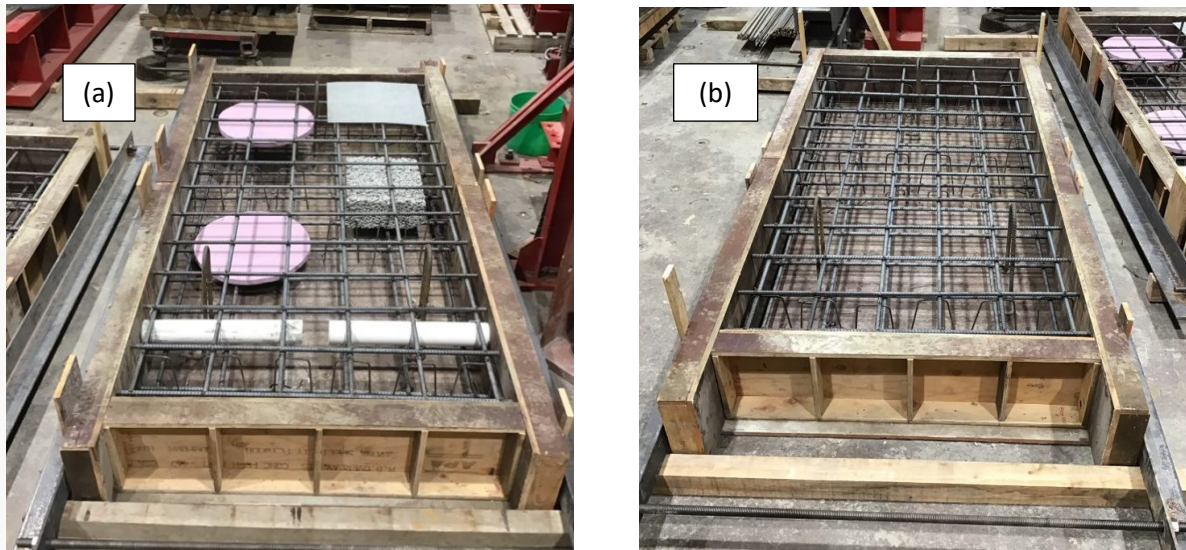


Figure 5-3. Slab specimen during construction (a) slab with defects (Slab 1), (b) reference slab (Slab 2).

Instrumentation

Impulse-response measurements are performed on both Slab 1 and Slab 2 using the instruments provided in Table 5-1. The measurements are performed on a square grid of 300 mm. The distance between the hammer impact and the position of the sensor is kept at 75 mm for all test points.

Table 5-1. Specifications of the instruments used for the impulse-response test measurements.

Instrument	Notes
Accelerometer	PCB 352C33 piezoelectric accelerometer, with 100.5 mV/g sensitivity and 0.5-10000 Hz range.
Hammer	PCB 086D05 hammer with force sensor and plastic tip with minimum upper usable frequency range of 1800 Hz.
Data Acquisition system	National Instruments 6123-USB DAQ Device

The impulse-response measurements are performed at a sampling frequency of 10 kHz (for every 0.4096 seconds) and the Accelerance spectrum generated of each test point is obtained using Eq. 5-20.

$$Accelerance = \left| \frac{FFT(A(t))}{FFT(f(t))} \right| \quad (5-20)$$

Where  $A(t)$  and  $f(t)$  are respectively the response and force time histories obtained for each measurement. A graphical user interface-based software is developed in MATLAB for recording the impulse-response test measurements and controlling the quality of measurements.

In the current practice, the upper frequency range of the FRF is limited at 800 Hz. However, the slabs are unrestrained at the edges and low frequencies are expected to be dominated by global responses, which are not affected significantly by the presence of the deep delamination and the honeycomb in Slab 1. For this reason, the upper frequency range of the FRFs was progressively increased from 800 Hz to 1400 Hz. Based on the findings from previous studies (Sajid, Chouinard, & Taras, 2022) the useful frequency range for unrestrained specimens is selected as 10 to 1200 Hz. Increasing the frequency range beyond 1200 Hz does not result in significant changes in diagnostic value.

#### Clustering with AP and condition assessment

The feature space matrix obtained from the impulse-response test measurements is clustered using the AP algorithm. For Slab 1, the input preferences ( $s(i, i)$ ) are selected as the first quartile of the input similarities ( $s(i, k)$ ) to target a total of 6 exemplars. Underfitting (too many exemplars) can be corrected by testing for homoscedasticity and merging pairs of exemplars. However, overfitting (too few exemplars) may overlook defects and decrease the detection capabilities of the proposed procedure. A flow chart of the procedure adopted for the condition assessment of slabs is provided in Figure 5-4.



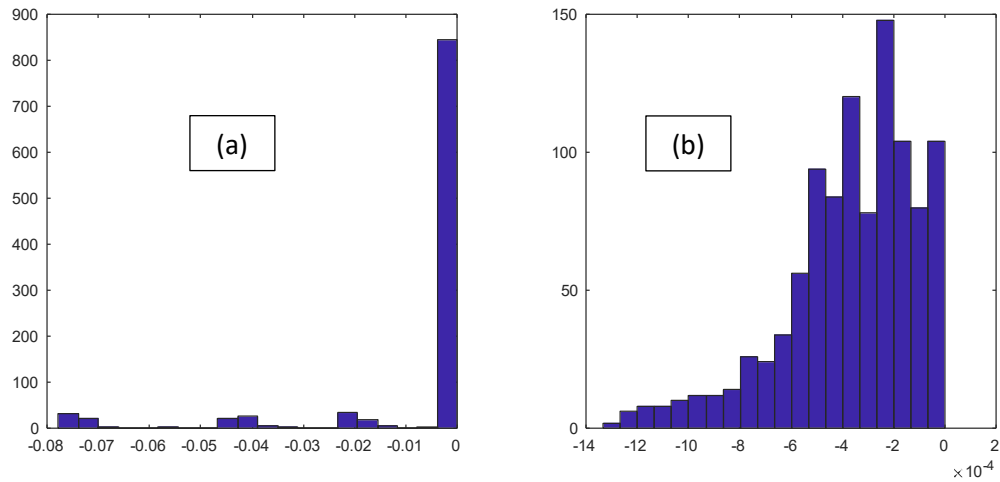


Figure 5-6. The distribution of the input similarities, which includes all the entries of the similarities matrix for (a) Slab 1, and (b) Slab 2.

The Levene’s test is used to assess the homoscedasticity of each pair of the exemplars obtained in Figure 5-5 at a significance level of 5%. The p-values for each pair of exemplars are provided in Table 5-2, which shows that the null hypothesis is rejected for all exemplar pairs. Furthermore, it can be also concluded that the input preferences of 0.25 used to perform AP does not result in underfitting.

Table 5-2. P-values of Levene's test for each pair of exemplars for Slab 1.

Variance	Exemplars	22	29	20	8	7	4	Rank
3.58E-07	22	...	0	0	0	0	0	1
1.14E-06	29		...	0	0.002	0	0	2
1.39E-06	20			...	0	0	0	3
1.64E-05	8				...	0	0	4
3.00E-05	7					...	0	5
4.50E-05	4						...	6

In Table 5-2, the exemplars are ranked in order of increasing variance. The exemplars and the associated FRFs for Slab 1 are shown in Figure 5-7, which shows a close agreement between the FRFs of cluster members and of the corresponding exemplars. The exemplars are ranked based on their variance, which is correlated to the severity of the defects. The variances of the exemplars

are assigned to each test point given their cluster membership and displayed in Figure 5-8. The honeycomb defect and the deep delamination are detected but not completely delineated and may be due to the proximity of the defects to the boundary of the plate. This result is consistent with findings from a previous study that indicates that the limit of detectability of deep delamination with the impulse-response test is in the order of 300mm (Sajid et al., 2022).

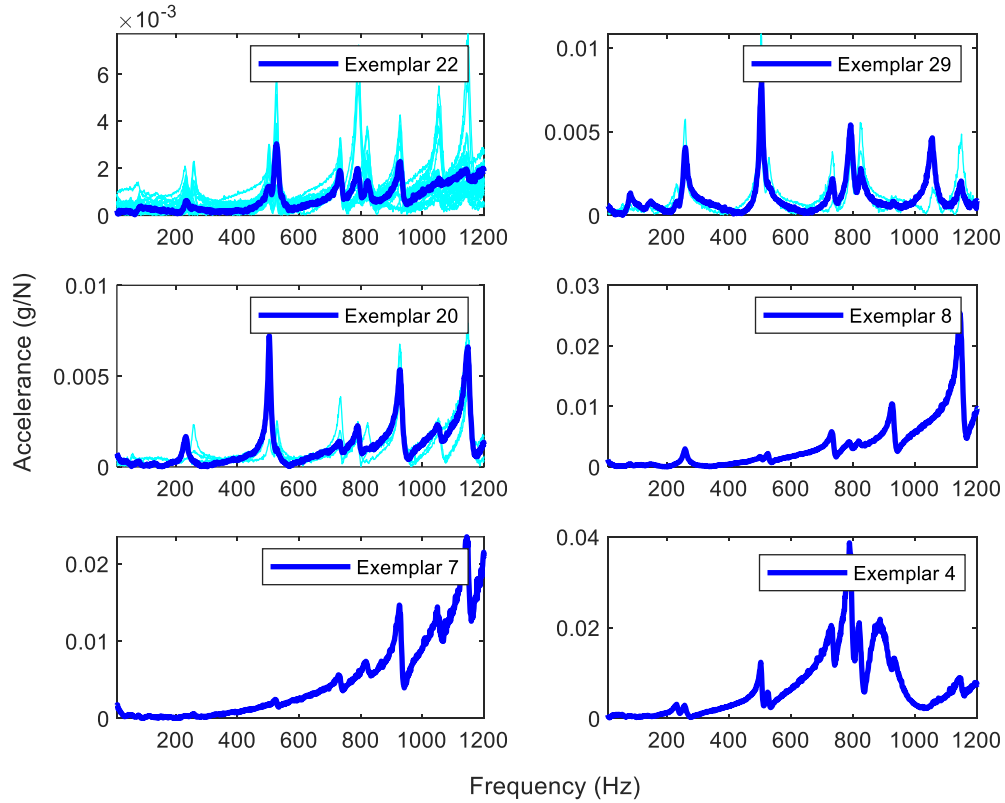


Figure 5-7. Exemplars and the associated FRFs in the respective clusters for Slab 1

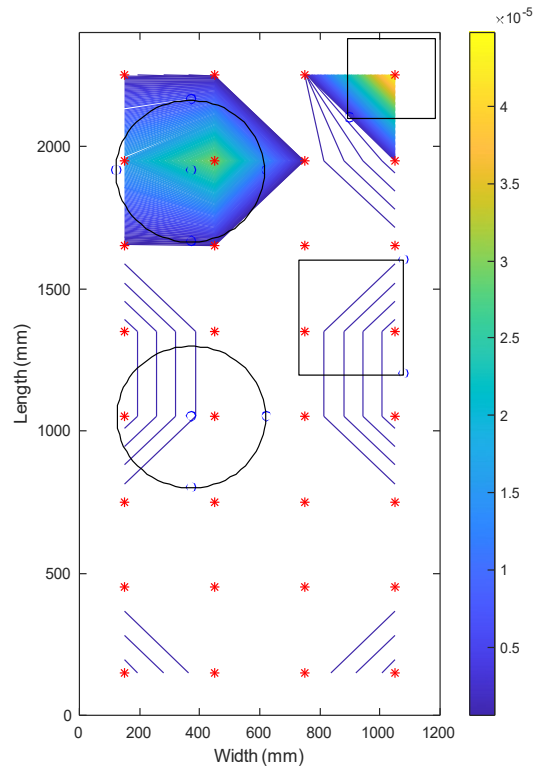


Figure 5-8. Contour plot of ranks of each test point.

The proposed defect detection procedure is also applied on the feature space matrix obtained from the impulse-response test measurements on the fully supported reference slab with free edges and no defects. The same input preference value of 0.25 and the frequency range of 10-1200 Hz of the FRFs are used to perform the analysis. The exemplars obtained along with the respectively member FRFs are shown in Figure 5-9c.

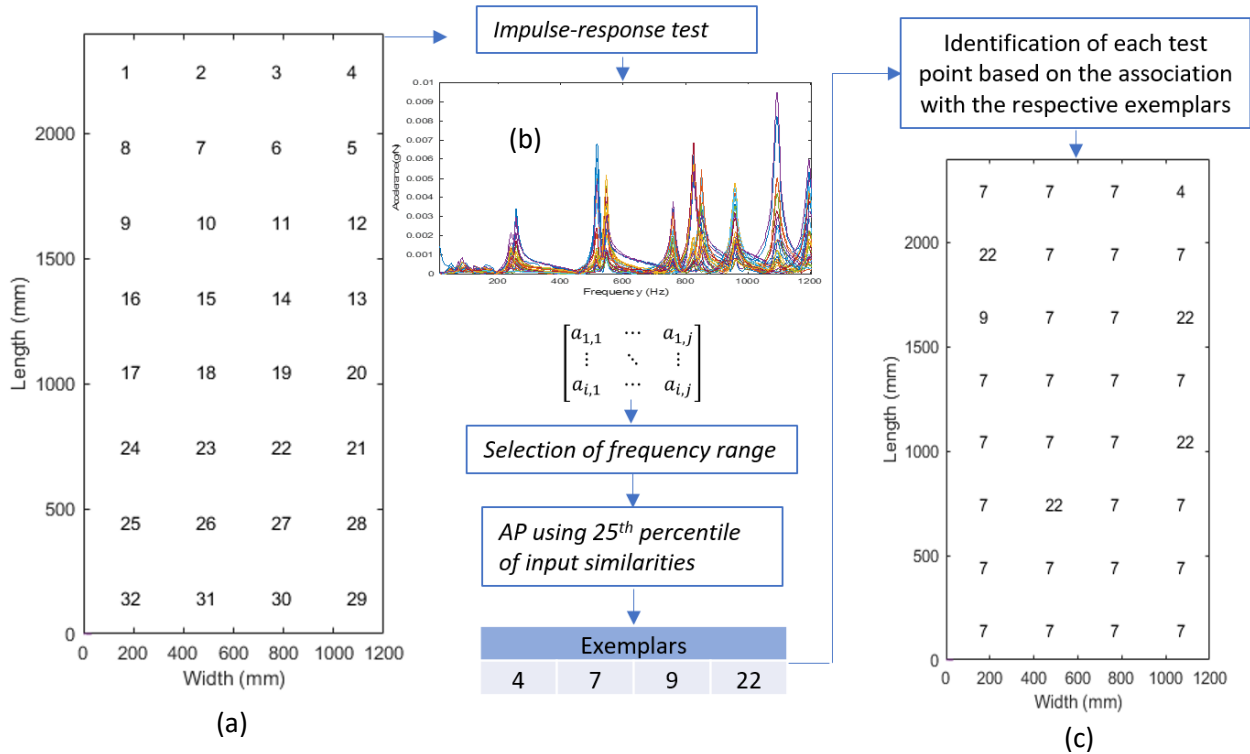


Figure 5-9. AP algorithm for to obtain exemplars and their associated FRFs for Slab 2.

Clustering with the AP for fully supported reference slab with free edges.

Four exemplars are identified by the AP algorithm for Slab 2 and are mostly located in proximity to the edge of the plate, indicating the FRFs may be influenced by local support conditions. However, the variances of the four exemplars are of the same order of magnitude indicating that there is no significant defect in the plate. This is confirmed by the results of the Levene's test (Table 5-3). The p-values are above or equal to 0.05 except of the pair of exemplars 4 and 7, where exemplar 4 may be influenced a local corner support condition. Nevertheless, all other pairs of exemplars fail to reject the null hypothesis of equal variances. Therefore, based on high p-values, the Levene's test fails to reject the null hypothesis of equal variances, and all test points can be represented by a single exemplar for the reference slab as shown in Figure 5-10. The histogram of the input similarities for Slab 2 given in Figure 5-6b also does not show any distinct groups, which implies closely spaced FRFs in feature space matrix.

Table 5-3. Levene’s test for exemplars obtained using AP for the reference slab with free-free edges.

Exemplars	4	7	9	22
4	...	0.0065	0.7374	0.0889
7		...	0.05	0.0630
9			...	0.1497
22				...

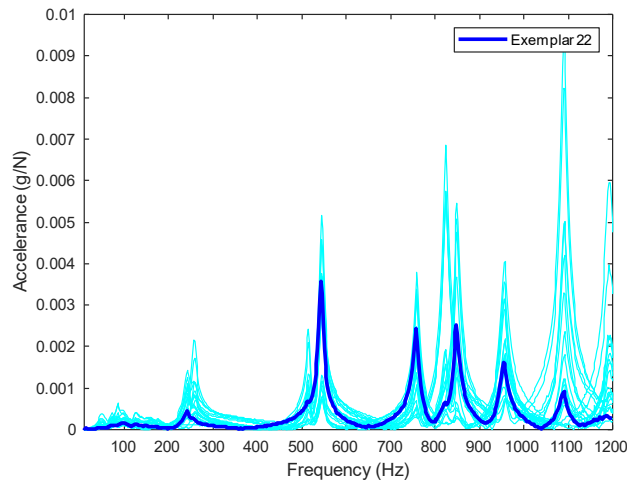


Figure 5-10. Exemplar and the corresponding FRFs for Slab 2.

### 5.7.2 Concrete slab on Elastic Foundation with Restrained Edges

#### Description

This slab is 380 mm thick with planar dimensions of 2300 mm by 3500 mm cast on a polystyrene insulation board, and reinforced with 12.7 mm diameter bars in both directions with a 127 mm center-to-center spacing, and 38.1 mm cover. An artificial delamination with a planar size of 600 mm by 470 mm was created using polystyrene foam and a simulated honeycomb defect of 490 mm by 400 mm was created using a precast concrete block made without fine aggregates. The delamination and honeycomb were placed at 56 mm and 116 mm, respectively, from the top surface of Slab 3.

The impulse-response measurements on the second slab specimen were performed using a 300 mm grid following the protocols of ASTM C1740-16. The measurements were performed with a

commercial test system that included a geophone and instrumented hammer, having 20 mV/m/s and 0.25 mV/N sensitivity, respectively. Data were recorded at a sampling frequency of 10 kHz with a National Instruments 5132 USB card.

The position of the measurement points relative to the defects on the test element are shown in Figure 10a. The velocity transducer was placed on each grid point to perform measurements and the hammer impact was always within  $100\pm 25$  mm from the corresponding grid point in conformity to ASTM C1740-16 (ASTM-C1740-16, 2016). The sampling frequency was 10 kHz and the signals were recorded for a duration of 0.1024 sec for a total of 1024 data points. The hammer tip used in the measurements had a contact time of 0.001s and produced a corresponding meaningful frequency range up to 800 Hz (Sajid, Chouinard, & Carino, 2019). The frequency resolution for the velocity FRFs is around 9.25 Hz. For the feature space matrix, a frequency range of 10-700 Hz was selected since this range covers the flat frequency response of the instrumented hammer.

#### Clustering of Mobility Spectra

The feature space matrix is first clustered using the AP algorithm. The input preference value was adjusted to reduce the number of exemplars to 5 or 6 based on the recommendation made in section 5.6.2. This is achieved with the 8<sup>th</sup> percentile of the input similarities after a trial and adjustment procedure. The input preferences value used for this feature space matrix is significantly smaller compared to that for the previous two experiments in this research. One reason may be due to the change of instrumentation from a glued accelerometer to a dry contact geophone. The smoothness of the FRFs for experiment with Slab 3 is relatively less compared to that of the other slabs because of lower frequency resolution. The exemplars and the associated cluster identifications for each test points are provided in Figure 5-11c. It can also be noted that the histogram of the input similarities shows groups at reasonably spaced from the majority of the values which implies the presence of distinct FRF shapes and hence the defects (Figure 5-12).

Next, the Levene's test is performed for each pair of exemplars (Table 5-4). The exemplar pairs 42 and 15, and 19 and 46 have significantly high p-values and the test fail to reject the null hypothesis at the 5% significance level. The FRFs of 42 and 15, and 19 and 46 are combined and relabelled 15 and 19 respectively given both these pairs have homogenous variances. Table 5-5 shows the final exemplars ranked based on their variances. The exemplars and their corresponding

FRFs are closely spaced as can be seen in Figure 5-13. The variances of the exemplars in Table 5-5 and their corresponding cluster members are shown on a contour plot in Figure 5-14 which accurately delineate the delamination but to a lesser extent the honeycomb.

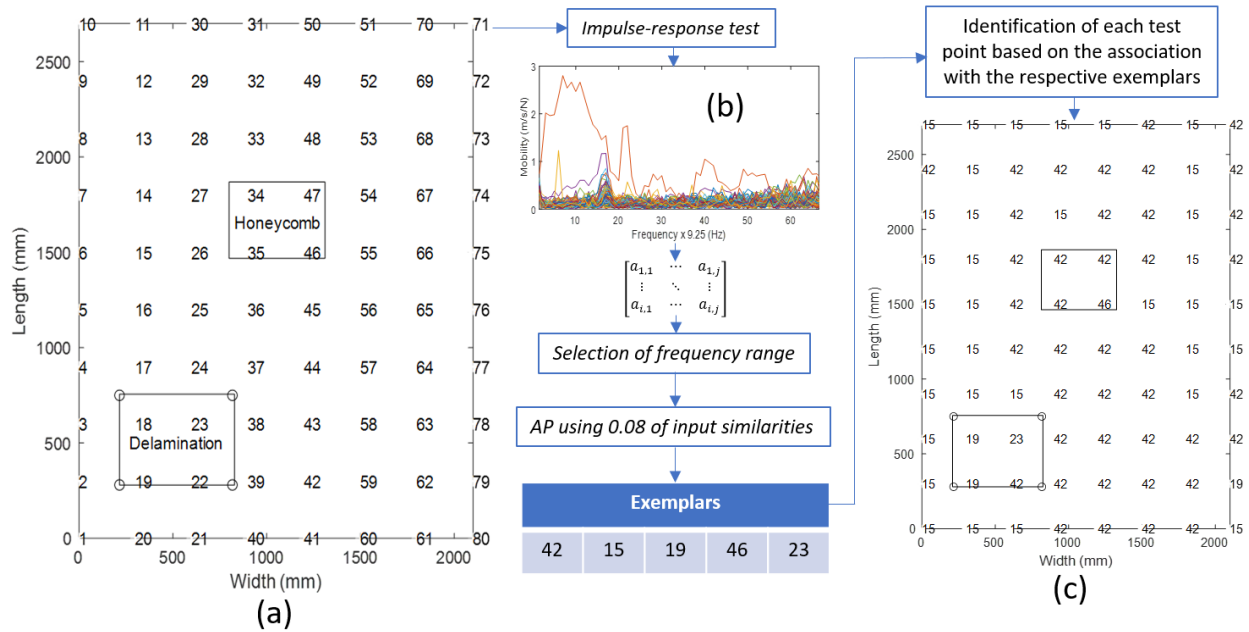


Figure 5-11. Defect delineation with the proposed algorithm for the impulse-response test data for Slab 3.

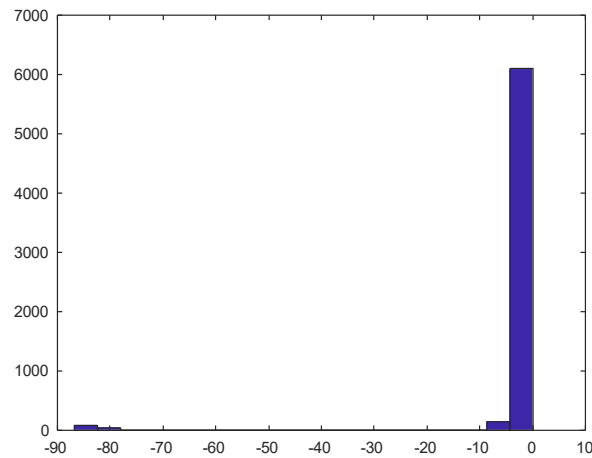


Figure 5-12. Histogram of the input similarities for Slab 3.

Table 5-4. P-values of Levene's test for each pair of the exemplars for Slab 3 obtained in Figure 5-11.

Exemplar	42	15	19	46	23
42	...	0.45	0	0	0
15		...	0	0	0
19			...	0.58	0
46				...	0
23					...

Table 5-5. Ascending order of exemplars based on individual variances for Slab 3.

Exemplar	Variance
15	0.0078
19	0.0324
23	0.5380

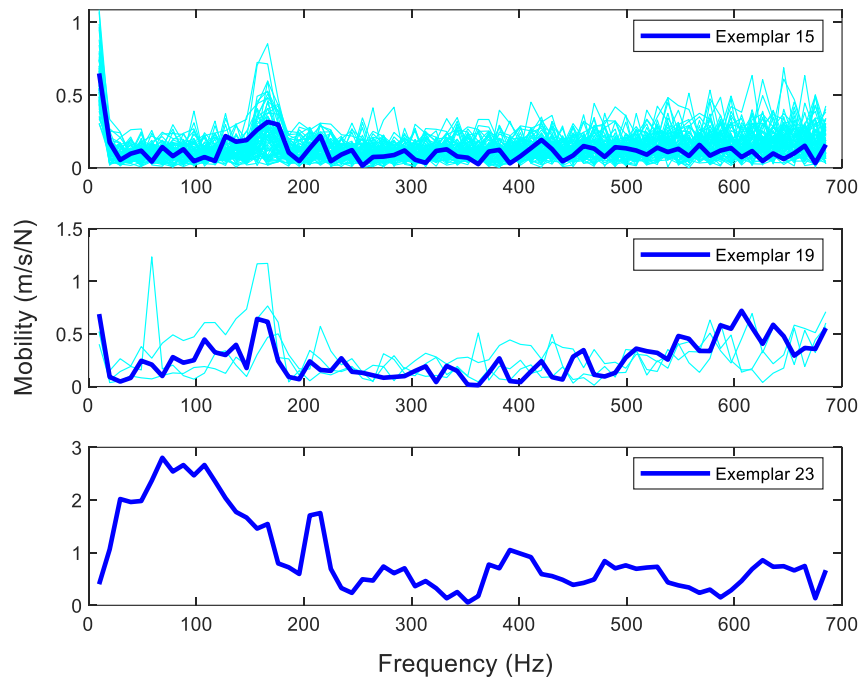


Figure 5-13. Exemplars and cluster members resulting from the AP and Levene's test for Slab 3.

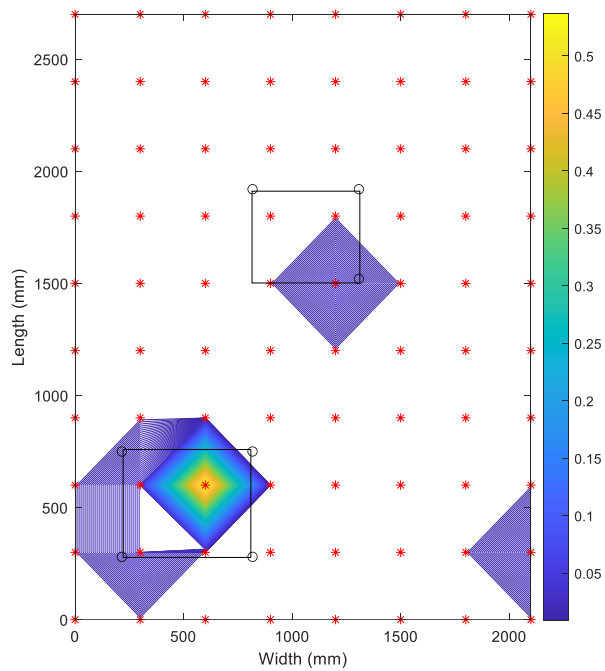


Figure 5-14. Contour plot of variances of FRFs associated with exemplar for Slab 3.

### 5.7.3 Ultrasonic Shear Wave Tomography Test for Slab 3

Shear-wave tomography is a very precise NDT technique that provides 3D imagery of the test element in the form of different scans (ACI-Committee-228, 2013; Aldo et al., 2013; Germann-Instruments, 2014). In this research, it is used on Slab 3 to confirm the detection of defects with the proposed procedure. The test was performed with MiRA® on a grid of 75 mm by 150 mm. All 3 scans (A-scan, B-scan and C-scan) were obtained using the SAFT algorithm; however, only C-scan is shown in Figure 5-15 for comparison with the impulse-response test, which provides the planar view of the plate at a particular depth. In this application, the depth was selected to be around 130 mm from the top surface of the plate such that both the delamination and honey-comb defects are visible. It also compares well with the detection of delamination and to a lesser degree of honeycomb by the proposed procedure.

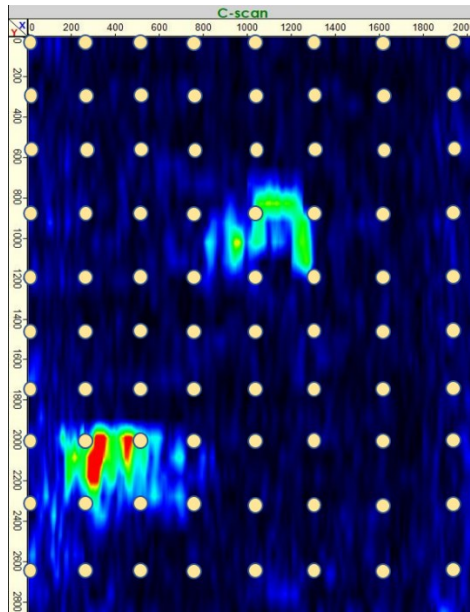


Figure 5-15. C-scan of the plate obtained with MiRA® after performing ultrasonic shear wave tomography (at a depth of around 130 mm from the top surface).

## 5.8 Concluding Remarks

The main contribution of this research is to propose a new procedure to improve the detection of defects with the impulse-response test, and an objective criterion based on variance for non-binary ranking relative to intact locations. The AP algorithm is shown to provide an efficient means for the analysis of feature space to identify distinct patterns without the need to pre-specify the number

of clusters. Instead, the number of clusters is controlled by selecting a given fractile from input similarities. The AP algorithm can result in overfitting or underfitting, which results in inaccurate delineation of defects. Using the experimental data from several plates, a trial and adjustment procedure is proposed to select the fractile input similarities to obtain 5 to 6 exemplars using the AP algorithm. To address underfitting, the Levene's test is introduced to assess the homoscedasticity for each pair of exemplars and merge those that meet the criteria of equal variances. The variances of exemplars for the corresponding FRFs are shown on contour map to objectively categorize defects on a non-binary basis. The proposed defect detection procedure is effective in detecting debonding, and shallow delaminations in the fully supported concrete plate with unrestrained edges (Slab 1) using a frequency range of 10-1200 Hz for the FRFs in the feature space matrix. The deeper delamination and the honeycomb in the same plate are also detected but to a lower extent. The proposed procedure is also applied to a concrete plate without any defects (Slab 2) and a single exemplar was obtained implying homogeneity of the FRFs for all the test points and hence no defects. A separate experimental plate (Slab 3) with different sensing instrumentation and different boundary conditions and base materials compared to the first two experimental plates is used for application of the proposed procedure. It is demonstrated that the delamination and honeycomb in this plate are delineated in a frequency range of 10-700 Hz. The results for this experimental slab are compared with the detection performed with the ultrasonic shear-wave tomography to generate baseline information, which shows accurate detection of delamination and to a lesser degree of the honeycomb with the proposed procedure.

### **Acknowledgement**

The authors would like to express gratitude to Mariana Lara and Andrea Godoy of Germann Instruments Inc. for the access and facilitation in measurements to the 3<sup>rd</sup> experimental slab (slab on elastic foundation with restrained edges) and facilitation of the testing. The Mobility Award by McGill University, Faculty of Engineering is acknowledged with thanks for funding the boarding, lodging and travel for the experiment at Germann Instruments Inc. The funding by Natural Science and Engineering Research Council of Canada and the MEDA awards are acknowledged for funding the doctoral thesis of the first author.

### **Conflict of Interest**

The authors declare no conflict of interest.

## References

- ACI. (American Concrete Institute). 2013. *Report on Nondestructive Test Methods for Evaluation of Concrete in Structure*. ACI 228.2R. Farmington Hills MI: ACI. In.
- Alamdari, M. M., Rakotoarivelo, T., & Khoa, N. L. D. (2017). A spectral-based clustering for structural health monitoring of the Sydney Harbour Bridge. *Mechanical Systems and Signal Processing*, 87, 384-400.
- Aldo, O., Samokrutov, A. A., & Samokrutov, P. A. (2013). Assessment of concrete structures using the Mira and Eyecon ultrasonic shear wave devices and the SAFT-C image reconstruction technique. *Construction and Building Materials*, 38, 1276-1291.
- Amick, H., Xiong, B., Tang, N., & Gendreau, M. (2009). Voids Beneath Slabs-on-Ground. *Concrete International*, 31(7), 29-33.
- Asadi, P., Gindy, M., & Alvarez, M. (2019). A machine learning based approach for automatic rebar detection and quantification of deterioration in concrete bridge deck ground penetrating radar B-scan images. *KSCE Journal of Civil Engineering*, 23(6), 2618-2627.
- ASTM-C1383-15. (2015). *Standard Test Method for Measuring the P-Wave Speed and the Thickness of Concrete Plates Using the Impact-Echo Method*. Retrieved from ASTM International, West Conshohocken, PA, 2015, [www.astm.org](http://www.astm.org):
- ASTM-C1740-16. (2016). *Standard practice for evaluating the condition of concrete plates using the impulse-response method*. Retrieved from ASTM International, West Conshohocken, PA, 2016, [www.astm.org](http://www.astm.org):
- ASTM-D6432-11. (2011). *Standard Guide for Using the Surface Ground Penetrating Radar Method for Subsurface Investigation*. Retrieved from ASTM International, West Conshohocken, PA, 2011, [www.astm.org](http://www.astm.org):
- Bodenhofer, U., Kothmeier, A., & Hochreiter, S. (2011). APCluster: an R package for affinity propagation clustering. *Bioinformatics*, 27(17), 2463-2464.
- Calabrese, L., Campanella, G., & Proverbio, E. (2010). Use of cluster analysis of acoustic emission signals in evaluating damage severity in concrete structures. *Journal of Acoustic Emission*, 28.
- Choi, J., Woods, C. R., Hrynyk, T. D., & Bayrak, O. (2020). Delamination Cracking Behavior of Curved Post-Tensioned Concrete Structures. *ACI Structural Journal*, 117(3), 169-183.

- Clem, D., & Schumacher, T. (2012). *A Fresh Look at Impulse Response as a Form of NDT for Concrete Bridge Decks*. Paper presented at the ACI Spring Convention March 18-22, Texas, USA, .
- Davis, A., & Hertlein, B. (1987). *Nondestructive testing of concrete pavement slabs and floors with the transient dynamic response method*. Paper presented at the Proc Int Conf Struct Faults Repair (Lond).
- Davis, A., Hertlein, B., Lim, M., & Michols, K. (1996). *Impact-Echo and Impulse Response stress wave methods: Advantages and limitations for the evaluation of highway pavement concrete overlays*.
- Davis, A. G. (2003). The nondestructive impulse response test in North America: 1985–2001. *NDT & E International*, 36(4), 185-193.
- Davis, A. G., Evans, J. G., & Hertlein, B. H. (1997). Nondestructive evaluation of concrete radioactive waste tanks. *Journal of performance of constructed facilities*, 11(4), 161-167.
- Davis, A. G., & Hertlein, B. H. (1995). *Nondestructive testing of concrete chimneys and other structures*. Paper presented at the Nondestructive Evaluation of Aging Structures and Dams.
- Davis, A. G., Lim, M. K., & Petersen, C. G. (2005). Rapid and economical evaluation of concrete tunnel linings with impulse response and impulse radar non-destructive methods. *NDT & E International*, 38(3), 181-186.
- Diez, A., Khoa, N. L. D., Alamdari, M. M., Wang, Y., Chen, F., & Runcie, P. (2016). A clustering approach for structural health monitoring on bridges. *Journal of Civil Structural Health Monitoring*, 6(3), 429-445.
- Dinh, K., Zayed, T., Moufti, S., Shami, A., Jabri, A., Abouhamad, M., & Dawood, T. (2015). Clustering-based threshold model for condition assessment of concrete bridge decks with ground-penetrating radar. *Transportation Research Record*, 2522(1), 81-89.
- Dodge, E. C., & Chapa, S. V. *Impulse response testing - analysis of relative test data*. Paper presented at the International Symposium on Non-Destructive Testing in Civil Engineering (NDT-CE) September 15-17, 2015, Berlin , Germany.
- Ewins, D. J. (2009). *Modal testing: theory, practice and application*: John Wiley & Sons.
- Fang, K., Liu, C., & Teng, J. (2018). Cluster-based optimal wireless sensor deployment for structural health monitoring. *Structural Health Monitoring*, 17(2), 266-278.

- Frey, B. J., & Dueck, D. (2007). Clustering by passing messages between data points. *science*, 315(5814), 972-976.
- Germann-Instruments. (2014). NDT Systems - Bridging NDT Theory and Practice. In (pp. 96-102).
- Ham, S., & Popovics, J. (2015). Application of micro-electro-mechanical sensors contactless NDT of concrete structures. *Sensors*, 15(4), 9078-9096.
- Hu, Q., Liu, X., Wu, Q., Cao, J., Liu, Y., & Tan, Y. (2012). *Cluster-based energy-efficient structural health monitoring using wireless sensor networks*. Paper presented at the 2012 International Conference on Computer Science and Service System.
- Igual, J. (2020). Hierarchical clustering of materials with defects using impact-echo testing. *IEEE Transactions on Instrumentation and Measurement*.
- Igual, J., Salazar, A., Safont, G., & Vergara, L. (2015). Semi-supervised Bayesian classification of materials with impact-echo signals. *Sensors*, 15(5), 11528-11550.
- Kabir, S., Rivard, P., He, D.-C., & Thivierge, P. (2009). Damage assessment for concrete structure using image processing techniques on acoustic borehole imagery. *Construction and Building Materials*, 23(10), 3166-3174.
- Kang, M.-S., Kim, N., Lee, J. J., & An, Y.-K. (2019). Deep learning-based automated underground cavity detection using three-dimensional ground penetrating radar. *Structural Health Monitoring*, 1475921719838081.
- Lattanzi, D., & Miller, G. R. (2014). Robust automated concrete damage detection algorithms for field applications. *Journal of Computing in Civil Engineering*, 28(2), 253-262.
- Levene, H. (1960). Contributions to probability and statistics. *Essays in honor of Harold Hotelling*, 278-292.
- Liao, T. W. (2005). Clustering of time series data—a survey. *Pattern recognition*, 38(11), 1857-1874.
- Lim, M. K., & Cao, H. (2013). Combining multiple NDT methods to improve testing effectiveness. *Construction and Building Materials*, 38, 1310-1315.
- Lloyd, S. (1982). Least squares quantization in PCM. *IEEE transactions on information theory*, 28(2), 129-137.

- Martin, J., Broughton, K., Giannopolous, A., Hardy, M., & Forde, M. (2001). Ultrasonic tomography of grouted duct post-tensioned reinforced concrete bridge beams. *NDT & E International*, 34(2), 107-113.
- Mei, J., Liu, M., Wang, Y.-F., & Gao, H. (2015). Learning a mahalanobis distance-based dynamic time warping measure for multivariate time series classification. *IEEE transactions on Cybernetics*, 46(6), 1363-1374.
- Miller, G. (2010). Crystal River Unit# 3 Containment Delamination Investigation and Repair. *Progress Energy*, Mar.
- Omar, T., & Nehdi, M. L. (2017a). *Clustering-based threshold model for condition assessment of concrete bridge decks using infrared thermography*. Paper presented at the International Congress and Exhibition" Sustainable Civil Infrastructures: Innovative Infrastructure Geotechnology".
- Omar, T., & Nehdi, M. L. (2017b). Remote sensing of concrete bridge decks using unmanned aerial vehicle infrared thermography. *Automation in Construction*, 83, 360-371.
- Ottosen, N. S., Ristinmaa, M., & Davis, A. G. (2004). Theoretical interpretation of impulse response tests of embedded concrete structures. *Journal of engineering mechanics*, 130(9), 1062-1071.
- Park, S., Lee, J.-J., Yun, C.-B., & Inman, D. J. (2008). Electro-mechanical impedance-based wireless structural health monitoring using PCA-data compression and k-means clustering algorithms. *Journal of intelligent material systems and structures*, 19(4), 509-520.
- Perera, R., Torres, L., Ruiz, A., Barris, C., & Baena, M. (2019). An EMI-Based Clustering for Structural Health Monitoring of NSM FRP Strengthening Systems. *Sensors*, 19(17), 3775.
- Rousseeuw, P. J. (1987). Silhouettes: a graphical aid to the interpretation and validation of cluster analysis. *Journal of computational and applied mathematics*, 20, 53-65.
- Sajid, S., & Chouinard, L. (2019). Impulse response test for condition assessment of concrete: A review. *Construction and Building Materials*, 211, 317-328.
- Sajid, S., Chouinard, L., & Carino, N. (2019). Robustness of Resonant Frequency Test for Strength Estimation of Concrete. *Advances in Civil Engineering Materials*, 8(1), 451-462.
- Saldua, B. P., Dodge, E. C., Kolf, P. R., & Olson, C. A. (2018). Reinforced concrete antenna pedestal. *Concrete International*, 40(4), 40-42.
- Sematech, N. (2006). Engineering statistics handbook. *NIST SEMATECH*.

- Shirkhorshidi, A. S., Aghabozorgi, S., & Wah, T. Y. (2015). A comparison study on similarity and dissimilarity measures in clustering continuous data. *PloS one*, *10*(12), e0144059.
- Snedecor, G., & William, G. (1989). Statistical methods/george w. *Snedecor and william g. Cochran*.
- Sun, H., Pashoutani, S., & Zhu, J. (2018). Nondestructive evaluation of concrete bridge decks with automated acoustic scanning system and ground penetrating radar. *Sensors*, *18*(6), 1955.
- Tarussov, A., Vandry, M., & De La Haza, A. (2013). Condition assessment of concrete structures using a new analysis method: Ground-penetrating radar computer-assisted visual interpretation. *Construction and Building Materials*, *38*, 1246-1254.
- Vlasblom, J., & Wodak, S. J. (2009). Markov clustering versus affinity propagation for the partitioning of protein interaction graphs. *BMC bioinformatics*, *10*(1), 1-14.
- Völker, C., & Shokouhi, P. (2015). Clustering based multi sensor data fusion for honeycomb detection in concrete. *Journal of Nondestructive Evaluation*, *34*(4), 32.
- Yeung, W., & Smith, J. (2005). Damage detection in bridges using neural networks for pattern recognition of vibration signatures. *Engineering Structures*, *27*(5), 685-698.
- Yu, L., Zhu, J.-h., & Yu, L.-l. (2013). Structural damage detection in a truss bridge model using fuzzy clustering and measured FRF data reduced by principal component projection. *Advances in Structural Engineering*, *16*(1), 207-217.
- Zhang, J.-K., Yan, W., & Cui, D.-M. (2016). Concrete condition assessment using impact-echo method and extreme learning machines. *Sensors*, *16*(4), 447.
- Zhou, Y.-L., Maia, N. M., Sampaio, R. P., & Wahab, M. A. (2017). Structural damage detection using transmissibility together with hierarchical clustering analysis and similarity measure. *Structural Health Monitoring*, *16*(6), 711-731.
- Zhu, J., & Popovics, J. S. (2007). Imaging concrete structures using air-coupled impact-echo. *Journal of engineering mechanics*, *133*(6), 628-640.
- Zoidis, N., Tatsis, E., Vlachopoulos, C., Gotzamanis, A., Clausen, J. S., Aggelis, D. G., & Matikas, T. E. (2013). Inspection, evaluation and repair monitoring of cracked concrete floor using NDT methods. *Construction and Building Materials*, *48*, 1302-1308.

## 6. Chapter 6. Original Research Contributions and Recommendations

### 6.1 Original Research Contributions

- a. The impulse-response test for concrete elements is shown to perform diagnostics using the standing waves and the relative variations in the local dynamic characteristics of the test element forms the basis of detection with it. Therefore, it can potentially overcome the downside of limited detectability of defects below reinforcing steel by the reflective based NDT methods such as impact-echo and ground penetrating radar.
- b. The test may have limited sensitivity to delamination at depths greater than 250 mm from the top surface in a reinforced concrete plate. The existing tolerance of the distance between the hammer and the sensor for taking measurement with the test by ASTM C1740 of  $100\pm 25$  mm is found to potentially introduce uncertainties in the test results primarily owing to the experimental setup. A more stringent tolerance of  $100\pm 10$  mm is proposed especially for characterizing the depth of delamination with the measurements.
- c. The current practice of the impulse-response test stipulates the frequency range of the frequency response function obtained with the test as 10-800 Hz. The experiments and the analyses performed in this research indicates that with minor modification in instrumentation, the frequency range of the test can be increased from its current upper limit to around 2000 Hz. With this extended frequency range, the new damage indicator, the frequency peak associated with the first bending mode of the portion of the plate above delamination is shown to have the potential to be used for the depth estimates of the delamination. The reliability of the depth estimates is quantified by Gaussian process which shows that these estimates can be significantly improved when the newly proposed damage indicator is combined with the average accelerance, which is the damage indicator used in the current practice. According to the author's best knowledge, the defect characterization has not been explored using the measurements from the impulse-response test.
- d. The factor score based on the principal component analysis of the full range of frequency response functions obtained with the impulse-response test is found as an effective damage indicator for detecting and ranking of defects based on the severity of damage. This together with outlier detection performed using the extreme valued Studentized test, and

box and whisker plots are shown to provide a practical and easily implementable damage detection procedure with the test. Defining the impulse-response test measurements in such a statistical pattern recognition paradigm enables identification of the test points with significant damages. Furthermore, using experiments, the proposed procedure is shown to detect artificial delamination and honeycomb in a reinforced concrete plate on elastic foundation, as opposed to the detection of delamination only with the existing data analysis procedures for the test. The results with the proposed defect detection procedure are shown to delineate defects with closely comparable accuracy as that of the highly refined yet time consuming ultrasonic shear-wave tomography test.

- e. The affinity propagation (AP) algorithm is shown to provide an efficient means for the analysis of feature space to identify distinct patterns without the need to pre-specify the number of clusters. Instead, the number of clusters is controlled by selecting a given fractile from input similarities. The AP algorithm can result in overfitting or underfitting, which results in inaccurate delineation of defects. Using the experimental data from several plates, a trail and adjustment procedure is proposed to select the fractile input similarities to obtain 5 to 6 exemplars using the AP algorithm. To address underfitting, the Levene's test is introduced to assess the homoscedasticity for each pair of exemplars and merge those that meet the criteria of equal variances. The variances of exemplars for the corresponding FRFs are shown on contour map to objectively categorize defects on a non-binary basis. The proposed defect detection procedure is effective in detecting debonding, and shallow delaminations in the fully supported concrete plate with unrestrained edges (Slab 1) using a frequency range of 10-1200 Hz for the FRFs in the feature space matrix.

## **6.2 Recommendations for Future Research**

- a. The impulse-response test operates on a relatively low frequency range and there may be a possibility of extracting component level response in-addition to the local level response. It is recommended to explore the possibility of generating eigen functions and the eigen values from the current measurement procedure as this will significantly increase the value of information obtained with the test. Furthermore, it will also give the information on influence of local defects, if any, on the global level performance of the test element.

- b. The use of modern non-contact sensing methods, such air-coupled sensors, instead of the traditional geophone in the experimental setup should be explored. The current research shows potentially improved detection with the test for a higher upper limit of the frequency range. The contact type sensor, which also will need coupling agent for each measurement significantly increase the time for the completion of the test. Therefore, using an air-couple sensor, such as a microphone, a micro-elctromechanical sensor (MEMS), high speed camera-based measurements, and the laser vibrometer are recommended for exploration in this regard in comparison with the traditionally used geophone and the piezo-electric accelerometer.
- c. The prospects for using the test in non-linear vibration analysis setup should be explored. The author believes the low frequency non-linearities in the form of slight shift and reduced damping of a given vibration mode in low frequencies may be representative of damages in the support condition. While in the high frequency range, such non-linearities may be representative of the micro-mechanical damages, for instance, due to alkali silica reaction.
- d. Given the stationary waves dominate the response during the impulse-response test, it is expected to have influence of the stiffness and the orientation of the support condition. Such influences are obtained were observed on the corners of the unrestrained portion of the plates studied during this research. It is suggested to perform study on the detectability of the defects above different support stiffnesses. Further study is also recommended to understand the influence of global support stiffness on the diagnostics with the impulse-response test given the relatively low frequency range use by the latter.